
Doctoral Dissertations

Student Theses and Dissertations

Fall 2019

Remanufacturing of precision metal components using additive manufacturing technology

Xinchang Zhang

Follow this and additional works at: https://scholarsmine.mst.edu/doctoral_dissertations



Part of the [Manufacturing Commons](#), and the [Materials Science and Engineering Commons](#)

Department: **Mechanical and Aerospace Engineering**

Recommended Citation

Zhang, Xinchang, "Remanufacturing of precision metal components using additive manufacturing technology" (2019). *Doctoral Dissertations*. 2853.

https://scholarsmine.mst.edu/doctoral_dissertations/2853

This thesis is brought to you by Scholars' Mine, a service of the Missouri S&T Library and Learning Resources. This work is protected by U. S. Copyright Law. Unauthorized use including reproduction for redistribution requires the permission of the copyright holder. For more information, please contact scholarsmine@mst.edu.

REMANUFACTURING OF PRECISION METAL COMPONENTS USING
ADDITIVE MANUFACTURING TECHNOLOGY

by

XINCHANG ZHANG

A DISSERTATION

Presented to the Faculty of the Graduate School of the
MISSOURI UNIVERSITY OF SCIENCE AND TECHNOLOGY

In Partial Fulfillment of the Requirements for the Degree

DOCTOR OF PHILOSOPHY

in

MECHANICAL ENGINEERING

2019

Approved by:

Dr. Frank Liou, Advisor
Dr. Ashok Midha
Dr. K. Chandrashekhara
Dr. Heng Pan
Dr. Xiaoming He

© 2019

Xinchang Zhang

All Rights Reserved

PUBLICATION DISSERTATION OPTION

This dissertation consists of the following five articles that have been published as follows:

Paper I, pages 8-32 have been published in JOM.

Paper II, pages 33-65 have been published in 2018 Annual International Solid Freeform Fabrication Symposium.

Paper III, pages 66-93 have been published in International Journal of Advanced Manufacturing Technology.

Paper IV, pages 94-122 have been published in International Journal of Advanced Manufacturing Technology.

Paper V, pages 123-154 have been published in International Journal of Advanced Manufacturing Technology.

All the above papers have been prepared in the Missouri University of Science and Technology dissertation format.

ABSTRACT

Critical metallic components such as jet engine turbine blades and casting die/mold may be damaged after servicing for a period at harsh working environments such as elevated temperature and pressure, impact with foreign objects, wear, corrosion, and fatigue. Additive manufacturing has a promising application for the refurbishment of such high-costly parts by depositing materials at the damaged zone to restore the nominal geometry. However, several issues such as pre-processing of worn parts to assure the repairability, reconstructing the repair volume to generate a repair tool path for material deposition, and inspection of repaired parts are challenging. The current research aims to address crucial issues associated with component repair based on three research topics. The first topic is focusing on the development of pre-repair processing strategies which includes pre-repair machining to guarantee the damaged parts are ready for material deposition and pre-repair heat-treatment to restore the nominal mechanical properties. For this purpose, some damaged parts with varied defects were processed based on the proposed strategies. The second topic presents algorithms for obtaining the repair volume on damaged parts by comparing the damaged 3D models with the nominal models. Titanium compressor blades and die/mold were used as case studies to illustrate the damage detection and reconstructing algorithms. The third topic is the evaluation of repaired components through material inspection and mechanical testing to make sure the repair is successful. The current research contributes to metallic component remanufacturing by providing knowledge to solve key issues coupled with repair. Moreover, the research results could benefit a wide range of industries, such as aerospace, automotive, biomedical, and die casting.

ACKNOWLEDGMENTS

First of all, I would like to express my earnest thankfulness for my advisor, Dr. Frank Liou, for guiding, inspiring, encouraging, and motivating me during my Ph.D. study at the Department of Mechanical and Aerospace Engineering at Missouri University of Science and Technology. I would like to show my profound gratitude for the experience and professional knowledge I've learned from him. I'm grateful to him for giving me the opportunity to work in the team and I have enjoyed my time working under his supervision.

I would also like to extend my appreciation to all my advisory committee members, Dr. Ashok Midha, Dr. K. Chandrashekhara, Dr. Heng Pan, and Dr. Xiaoming He. The advisory committee members contributed invaluable guidance and advice on my research projects. Thank you once again for your time and efforts.

The research and dissertation were also supported by Laser-Aided Manufacturing Processes (LAMP) Laboratory and Intelligent Systems Center (ISC) at the Missouri University of Science and Technology. Their support is greatly appreciated.

In addition, I would like to show my special thanks to my colleagues in LAMP laboratory, Mr. Todd Sparks, Dr. Wei Li, Dr. Lei Yan, Dr. Sreekar Karnati, Mr. Yunlu Zhang, Dr. Xueyang Chen, Ms. Wenyuan Cui, Ms. Tan Pan, Mr. Max Mulholland, Mr. Connor L. Coward, Mr. Leon Hills, Dr. Sriram Isanaka, and Mr. Aaron Flood, for helping and advising me for my professional and personal life.

Last but not least, I wish to sincerely appreciate my wife, Peipei Hou, my parents, and all my family members for their endless love and generous support towards me. Thank you!

TABLE OF CONTENTS

	Page
PUBLICATION DISSERTATION OPTION.....	iii
ABSTRACT.....	iv
ACKNOWLEDGMENTS	v
LIST OF ILLUSTRATIONS.....	xi
LIST OF TABLES.....	xvi
 SECTION	
1. INTRODUCTION.....	1
1.1. BACKGROUND	1
1.2. RESEARCH OBJECTIVES.....	3
1.3. ORGANIZATION OF DISSERTATION	5
 PAPER	
I. EXPERIMENTAL CHARACTERIZATION OF A DIRECT METAL DEPOSITED COBALT-BASED ALLOY ON TOOL STEEL FOR COMPONENT REPAIR.....	8
ABSTRACT.....	8
1. INTRODUCTION.....	9
2. EXPERIMENTAL PREPARATION	11
2.1. MATERIALS	11
2.2. EXPERIMENTAL SETUP.....	13
2.3. SPECIMEN PREPARATION AND MATERIAL CHARACTERIZATION.....	16
3. RESULTS AND DISCUSSION.....	17

3.1. MACROSTRUCTURE EXAMINATION.....	17
3.2. MICROSTRUCTURE AND EDS ANALYSIS	19
3.3. TENSILE TESTING OF THE REPAIRED SAMPLES.....	22
3.4. MICROHARDNESS MEASUREMENTS	26
4. CONCLUSION.....	28
ACKNOWLEDGMENTS	29
REFERENCES	29
II. DEVELOPMENT OF PRE-REPAIR PROCESSING STRATEGIES FOR LASER-AIDED METALLIC COMPONENT REMANUFACTURING	33
ABSTRACT.....	33
1. INTRODUCTION	34
2. PRE-REPAIR MACHINING STRATEGIES FOR SURFACE DENTS.....	37
2.1. DAMAGED PART CLEANING AND PRE-REPAIR INSPECTION	38
2.2. MODEL RECONSTRUCTION OF A BLOCK	39
2.3. CUT-OFF VOLUME DEFINITION.....	40
2.3.1. U-Shaped Boundary Definition.	42
2.3.2. Convex-Hull Boundary Definition.	45
2.4. MACHINING VOLUME ACQUISITION.....	47
2.5. PRE-REPAIR MACHINING PROGRAM GENERATION	49
3. PRE-REPAIR MACHINING STRATEGY FOR SURFACE EROSION, WEAR, CORROSION, AND HEAT CHECKS	50
3.1. MODEL RECONSTRUCTION OF A DIE	51
3.2. MACHINING VOLUME DETERMINATION AND MACHINING	52
4. PRE-REPAIR MACHINING STRATEGY FOR CRACKING.....	53

4.1. MACHINING STRATEGY FOR CRACKING ON BLADES.....	55
5. PRE-REPAIR HETA-TREATMENT OF DAMAGED DIE	57
6. CONCLUSION.....	60
ACKNOWLEDGMENTS	61
REFERENCES	61
III. DAMAGE DETECTION AND RECONSTRUCTION ALGORITHM IN REPAIRING COMPRESSOR BLADE BY DIRECT METAL DEPOSITION....	66
ABSTRACT.....	66
1. INTRODUCTION	67
2. GENERAL STRUCTURE OF DAMAGE DETECTION AND RECONSTRUCTION ALGORITHM	70
2.1. MODEL ACQUISITION	72
2.2. MODEL BEST FIT	74
2.3. DAMAGE DETECTION	83
2.4. DAMAGE EXTRACTION.....	84
3. BLADE REPAIR EXPERIMENT.....	86
3.1. EXPERIMENTAL SETUP.....	86
3.2. REPAIR RESULT AND MICROSTRUCTURE EVALUATION.....	87
4. CONCLUSION.....	90
ACKNOWLEDGMENTS	90
REFERENCES	91
IV. DAMAGE RECONSTRUCTION FROM TRI-DEXEL DATA FOR LASER- AIDED REPAIRING OF METALLIC COMPONENTS	94
ABSTRACT.....	94
1. INTRODUCTION	95

2. DAMAGE RECONSTRUCTION METHODOLOGY.....	98
2.1. TRI-DEXEL MODEL AND DATA STRUCTURE.....	98
2.2. ROBOT-ASSISTED 3D SCANNING.....	101
2.3. MODEL RECONSTRUCTION AND MODEL ALIGNMENT	103
2.4. DAMAGE RECONSTRUCTION FROM TRI-DEXEL DATA	105
3. REPAIR EXPERIMENTS AND RESULTS.....	109
3.1. EXPERIMENTAL SETUP AND MATERIAL PREPARATION	109
3.2. REPAIR RESULTS	111
4. ACCURACY OF DAMAGE RECONSTRUCTION.....	112
5. ILLUSTRATING EXAMPLES OF DAMAGE RECONSTRUCTION FROM TRI-DEXEL DATA.....	114
6. CONCLUSION.....	117
ACKNOWLEDGMENTS	119
REFERENCES	119
V. EVALUATION OF COMPONENT REPAIR USING DIRECT METAL DEPOSITION FROM SCANNED DATA	123
ABSTRACT.....	123
1. INTRODUCTION	124
2. 3D SCANNING AND TOOL PATH GENERATION	127
3. EXPERIMENT PROCEDURE	131
3.1. MATERIALS AND PREPARATION	131
3.2. EXPERIMENTAL SETUP.....	133
3.3. SAMPLE PREPARATION AND MATERIAL CHARACTERIZATIONS	135
4. RESULTS AND DISCUSSION.....	136

4.1. MACRO EXAMINATION OF REPAIRED SAMPLES	136
4.2. MICROSTRUCTURE CHARACTERIZATION	138
4.3. MECHANICAL PROPERTIES.....	140
4.3.1. Tensile Behavior.....	140
4.3.2. Tensile Fracture Surface Morphology.....	143
4.3.3. Vickers Hardness Analysis.....	146
4.4. EDS ANALYSIS.....	148
4.4.1. Interface EDS Analysis.....	148
4.4.2. Deposits EDS Analysis.....	150
5. CONCLUSION.....	151
ACKNOWLEDGMENTS	152
REFERENCES	152
SECTION	
2. CONCLUSION	155
BIBLIOGRAPHY.....	159
VITA.....	160

LIST OF ILLUSTRATIONS

SECTION	Page
Figure 1.1. The framework of this dissertation.....	6
PAPER I	
Figure 1. (a) Dimensions of the prepared substrates with V-shaped grooves of 45°, 75°, and 90° sidewall inclination angle; SEM micrograph (b) and particle size distribution (c) of Wallex 50 alloy powder.....	12
Figure 2. Model reconstruction for tool path generation.	14
Figure 3. (a) Overview of the repaired samples; (b) Optical micrographs of cross-sections of the repaired samples.....	18
Figure 4. SEM micrographs of the boundary area of samples with 45° (a) and 75° (b) sidewall damage; (c) micrograph of top layers of the sample with 45° sidewall damage.....	20
Figure 5. EDS line scan result for samples with 45° (a) and 75° (b) sidewall damage	22
Figure 6. Tensile stress-strain curves for samples with 45° (a) and 75° (b) damage.....	24
Figure 7. Tensile fracture morphology.	25
Figure 8. Vickers hardness distribution.	27
PAPER II	
Figure 1. Pre-repair machining procedure for surface impact damage.....	37
Figure 2. An H13 tool steel substrate with ball-indented damage on the top surface	39
Figure 3. Structured-light 3D scanner for model reconstruction	40
Figure 4. Point cloud (a) and reconstructed STL model (b) of the substrate.....	40
Figure 5. Model slicing and enveloping boundary determination.	41
Figure 6. Sidewall inclination angle optimization for the U-shaped boundary.	44
Figure 7. Convex-hull boundary definition.	46

Figure 8. Unprocessed and processed models.	48
Figure 9. (a) Machining toolpath; (b) Machining setup; (c) Machined substrate	50
Figure 10. (a) A casting die with surface erosion, wear, and corrosion; (b) STL model of the damaged region of the casting die	52
Figure 11. (a) Machining tool path generation; (b) Machined model.....	52
Figure 12. (a) Titanium blade with cracks; (b) Reconstructed model of the blade; (c) Selection of points located at the damaged area	56
Figure 13. (a) Damaged point set extraction and its convex-hull; (b) Optimized contour; (c) Blade after pre-machining.....	56
Figure 14. (a) The hardness of H13 tool steel before and after thermal fatigue cycles [41]; (b) Microstructure of H13 tool steel after thermal fatigue cycles [41] ..	58
Figure 15. Schematic diagram of the re-hardening process for H13 tool steel.....	59
Figure 16. Tensile testing data of worn H13 tool steel (BH), re-hardened H13 tool steel (AH) and brand-new H13 tool steel in quenched and tempered condition	59
Figure 17. The hardness of worn H13 tool steel (BH), re-hardened H13 tool steel (AH) and brand-new H13 tool steel in quenched and tempered condition.....	60

PAPER III

Figure 1. Cross-section comparison showing the curved profile of a blade.	70
Figure 2. General structure of damage detection and reconstruction algorithms	71
Figure 3. Blade preparation.....	73
Figure 4. Model acquisition process.	74
Figure 5. Surface best-fitting process.	76
Figure 6. A cross-section of the nominal model (a) and damaged model (b).....	77
Figure 7. Aligned position after convex-hull centroid best fit.....	78
Figure 8. An irregular closed polygon illustrating the area calculation.....	79
Figure 9. Schematic diagram showing the relationship between A and A'	80

Figure 10. Cross-section best-fit process	81
Figure 11. Nominal and damaged profiles before (a) and after (b) cross-section best-fit	81
Figure 12. Best-fitted position of the damaged model with nominal model	82
Figure 13. Slices of the nominal model and damaged model	83
Figure 14. Defect detection process	83
Figure 15. Damaged layers detection.....	84
Figure 16. Cross-sections of blade models and intersections with casting rays	85
Figure 17. (a) Damage detection process; (b) Damage extraction processes	85
Figure 18. (a) DMD system; (b) DMD experimental setup; (c) Tool path generation for material deposition; (d) SEM images of Ti-6Al-4V particles.....	87
Figure 19. Compressor blade after the DMD process (a) and after machining (b)	88
Figure 20. Microstructure of substrate (a) and as-deposited titanium alloy (b).....	89
PAPER IV	
Figure 1. (a) Single dexel representation; (b) Data structure of a tri-dexel model	99
Figure 2. Comparison of a cross-section of a polyhedral model (a), voxel model (b), single-dexel model (c) and tri-dexel model (dexel along z-axis not shown) (d)	100
Figure 3. The Nachi robot and 3D scanner setup.....	101
Figure 4. Evaluation of the robot-assisted part scanning process.....	102
Figure 5. Model alignment.....	104
Figure 6. Flowchart of the damage reconstruction process from tri-dexel data	107
Figure 7. Damage extraction.....	108
Figure 8. Damage reconstruction for a fractured die.	109
Figure 9. (a) SEM micrograph (a) and particle size distribution (b) of Wallex 40 powder	110

Figure 10. Tool path generation and repair result.....	111
Figure 11. (a) A bracket nominal model; (b) Damaged model; (c) Defects	112
Figure 12. Accuracy analysis with different casting ray spacing.	113
Figure 13. Damage reconstruction for a damaged turbine rotor.	115
Figure 14. Damage reconstruction for a damaged die.	116
 PAPER V	
Figure 1. Schematic diagram of the laser-aided direct metal deposition process	125
Figure 2. H13 tool steel substrates with hemispherical-shaped defects.....	127
Figure 3. Flowchart of scanning to tool path generation	128
Figure 4. (a) 3D scanning setup; (b) Scanned point cloud; (c) Damage extraction.....	129
Figure 5. (a) Uncontinuous deposition pattern; (b) Continuous deposition pattern; (c) Repair tool path; Circular (d) and rectangular (e) finishing path.....	131
Figure 6. SEM micrograph (a) and particle size distribution (b) of Wallex 40 powder .	132
Figure 7. DMD equipment to perform repair experiment.....	134
Figure 8. Tensile test specimen preparation.	136
Figure 9. Repaired substrates from (a) repair 1, (b) repair 2, and (c) repair 3.....	137
Figure 10. Optical images of cross-sections of repaired substrates from (a) repair 1, (b) repair 2, and (c) repair 3.....	137
Figure 11. (a) Optical micrographs of materials on the bonding area; SEM micrograph of as-deposited Wallex 40 in the middle layers (b) and on the top (c)	139
Figure 12. Tensile stress-strain curves obtained from the tensile test for (a) Wallex 40 + H13 tool steel samples, and (b) H13 tool steel samples.....	141
Figure 13. Fracture morphologies in longitudinal section of a Wallex 40 + H13 tool steel sample.....	144
Figure 14. Fracture morphologies in cross-section of a Wallex 40 + H13 tool steel sample.....	146

Figure 15. Vickers hardness distribution	147
Figure 16. EDS mapping at the interface.....	148
Figure 17. EDS line scan analysis from the substrate to deposits	149
Figure 18. EDS mapping at the deposits.....	150

LIST OF TABLES

PAPER I	Page
Table 1. The chemical composition of the target materials (wt.%)	13
Table 2. Material deposition processing parameters.....	16
Table 3. UTS obtained from tensile testing	23
PAPER II	
Table 1. The volume of the model with varied pre-machining strategies	49
Table 2. Pre-repair machining parameters for surface impact damage	49
Table 3. Candidate machining approaches for cracking.....	54
PAPER III	
Table 1. The DMD processing parameters	86
PAPER IV	
Table 1. Chemical composition of the target materials (wt.%)	110
Table 2. Laser-aided DED processing parameters.....	111
Table 3. DED processing parameters for the samples in Figure 14.....	117
Table 4. CPU runtime for damage reconstruction	117
PAPER V	
Table 1. Chemical composition of the target materials (wt.%)	132
Table 2. Processing parameters for repair experiment.....	134
Table 3. UTS and elongation obtained from tensile testing.....	142

SECTION

1. INTRODUCTION

1.1. BACKGROUND

Crucial metallic components and structures such as aircraft jet engine turbine and compressor blades, landing gears, casting dies and molds, engine shafts and rods are designed to work at harsh conditions such as cyclic loading, impact loading, elevated temperature and pressure, rapid heating and cooling cycles, corrosion, and fatigue [1, 2]. In order to survive in such working environments, these components are usually made of high-performance materials such as titanium, nickel- and cobalt-based alloys, and tool steels. Fabrication of such parts are very costly since these materials require special tools for machining and in addition, most of these components are very complex in geometry which requires a significant amount of time and effort in the machining process [3]. After service for a period of time, defects such as surface indentations, heat checks, cracking, corrosion, wear, and deformation would appear on the parts. Because these key components are high-priced, remanufacturing of these parts is crucial for reinserting them into service to maximize their service lifespan to reduce costs in routine maintenance [4].

Additive Manufacturing (AM) process, especially powder-fed Directed Energy Deposition (DED), has a promising application for metallic component refurbishment [5-8]. A typical DED system consists of a laser that used for creating melt pool on damaged substrates, powder feeding nozzle for delivering metal powder from powder feeder to the melt pool, multi-axis stage for moving substrates according to designed tool path and

shielding gas for preventing the deposition from oxidation. In the repair process using a DED system, damaged regions on worn parts are defined, and metal powders are injected into the defective zone and then experience melting and solidification to recover the missing geometry. The critical surfaces with high surface finish requirements may undergo final machining before putting the repaired parts into service. In advantages, DED process can deposit a wide variety of metals including titanium, nickel- and cobalt-based alloys, tool steels, all of which are commercially available, and customized materials by mixing elemental powders with specific mixing ratio [9]. Besides, with optimized parameters, the process can precisely deposit materials in target areas with a small heat-affected zone, which enables the repair of delicate thin-wall structures [10]. Moreover, the process can form excellent metallurgical bonding between deposited materials and damaged components [11]. All these benefits make the DED process a great candidate for part remanufacturing.

Issues associated in component remanufacturing using DED process are still needed to be addressed urgently in order to widely apply this technique in industries. For example, most damaged parts cannot be directly deposited without pre-repair machining as defects may block the laser beam. Besides, reconstructing the repair volume is essential for remanufacturing since it provides the geometry that needs to be precisely recreated on the damaged region. In addition, a comprehensive inspection of the repaired components should be conducted to guarantee a successful repair. Currently, research focusing on solving these issues is lacking, which limits the further application of the repair technology. In order to address these problems, this dissertation will conduct research focusing on the

following key tasks. The outcomes will benefit many industries and areas for part refurbishment, such as aerospace, automotive, biomedical, and die casting.

1.2. RESEARCH OBJECTIVES

The main objective of the current research is to address key issues in the remanufacturing process using AM technology to broaden the application of this technology in a wide area. For this purpose, five research tasks are carefully conducted.

In detail, the research tasks 1 and 2 are carried out towards an overall objective of developing pre-repair processing strategies that should be conducted on the damaged parts to guarantee these parts are ready for repair. The research task 1 is trying to solve a problem that what damaged geometries could be successfully repaired. This task provides information that will be utilized for developing pre-repair processing strategies in research task 2. In task 1, V-shaped defects with varied sidewall inclination angles of 45° , 75° , and 90° were prepared on H13 tool steel material which is widely used in manufacturing casting dies and molds. The damage was repaired by depositing a Co-Ni-Cr-W alloy to assure a longer wear and corrosion life. In order to evaluate the repaired parts to clear whether the damaged substrates have been successfully repaired, macrostructure examination, microstructure characterization, EDS analysis, tensile testing, and microhardness measurement were performed on the repaired samples. The information obtained in research task 1 provides fundamental knowledge for task 2.

Research task 2 further extends the pre-repair processing technique by developing strategies for addressing typical defects such as surface indentations, corrosion, erosion, wear, fatigue, and cracking. Specifically, pre-repair processing includes two sections: pre-

repair machining and pre-repair heat-treatment. Pre-repair machining aims to machine off materials surrounding defects that make the damaged region inaccessible to laser beams and powder feed nozzle, while is trying to machine off as less material as possible because the machined volume unavoidably needs to be redeposited in the additive process. The pre-repair machining also aims to remove contaminated layers such as layers with corrosion, wear and heat checks on worn parts. Pre-repair heat-treatment was evaluated to restore the nominal mechanical properties of worn parts undergoing a large number of heating and cooling cycles during service. The outcomes of task 2 guarantee the worn parts are ready for material deposition.

Research task 3 addresses key issue in restoring jet engine turbine and compressor blades by reconstructing the missing cross-section profiles on the blade edges and tips. Recreating repair volume on damaged blades is crucial to guarantee a successful repair as the repair tool path is determined by the repair volume. In this study, a damaged blade was scanned using a structured-light 3D scanner to obtain the damaged model. Subsequently, the damaged model was precisely aligned with the nominal model based on proposed model alignment algorithms. After that, a damage reconstructing algorithm based on a one-dimensional ray casting method was implemented to regain the missing geometry. Tool path was then generated based on the missing geometry and material deposition experiment was conducted afterward. This approach realizes automatic model alignment, damage reconstruction, tool path generation, and enhances the automation and accuracy in repairing engine blades.

Research task 4 further extends the methodologies in task 3 through developing damage reconstruction method based on tri-dexel modeling that uses three-dimensional ray

casting method. Based on this approach, accurate three-dimensional repair volumes could be obtained. This methodology could also be applied to a variety of components including blades, dies, molds, shafts, brackets, engine blocks, etc. Several illustrating examples with different damaged geometries were implemented to show the feasibility of the proposed damage reconstruction approach.

Finally, research task 5 aims to evaluate the repaired metallic components through a series of tests to guarantee the repair is successful. For this purpose, surface indentations were prepared on substrates and subsequently repaired by DED process using cobalt-based alloys powders as the filler material. Geometries of the repaired samples were inspected. A systematic analysis method including microstructure characterization, elemental distribution analysis, tensile testing, hardness testing, and fracture surface analysis was performed on the repaired samples. This study verifies that repaired parts may yield superior properties than their nominal counterparts, showing the promising value of component remanufacturing.

The outcomes of the aforementioned research tasks are expected to contribute to component remanufacturing using AM technology for high-value metallic parts refurbishment. The algorithms, methodologies, and approaches developed in this study may benefit not only the area of component repair but also other areas such as hybrid manufacturing, automation engineering, and advanced manufacturing.

1.3. ORGANIZATION OF DISSERTATION

This dissertation has five correlative tasks with the core goal of metallic component remanufacturing using additive manufacturing technology, while each task addresses a

specific issue for realizing the overall objective. The organization of this dissertation is illustrated in Figure 1.1.

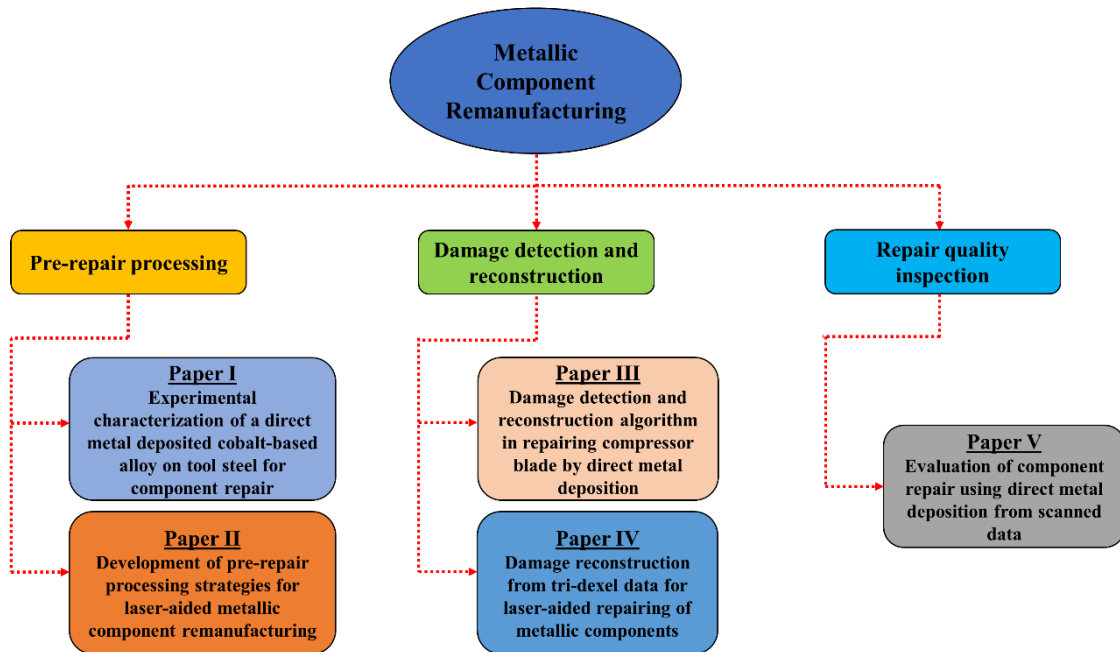


Figure 1.1. The framework of this dissertation

Paper I investigated the effects of angles of the machined surfaces on the quality of repaired parts. Damaged parts with different sidewall inclination angles were repaired and analyzed. The results obtained in this task would provide necessary information for guiding the development of pre-repair machining strategies. Paper II concentrated on the development of pre-repair processing methodologies which include pre-repair machining and pre-repair heat-treatment. Approaches for machining typical defects such as surface indentations, corrosion, wear, heat checks, and cracking were developed and implemented by case studies using Computer Numerical Control (CNC) machine and Electrical

Discharge Machining (EDM). Pre-repair heat-treatment procedure for H13 tool steel that is widely used for manufacturing casting dies, molds and tools was presented to restore the nominal properties of damaged parts due to fatigue failure after a large number of thermal cycles. Mechanical properties of re-hardened samples were compared with the corresponding properties of damaged specimens to show the benefits and necessity of pre-repair heat-treatment. Paper III introduced a method for refurbishing damaged jet engine turbine and compressor blades, which has an immense value of remanufacturing. Algorithms for accurately aligning damaged blade models with their nominal models were investigated. Besides, repair volume reconstruction approach based on one-directional ray casting method was proposed. Paper IV further extended the damage reconstruction method by casting rays in three directions (Tri-dexel modeling). This approach is capable of generating three-dimensional repair volumes for a variety of metal parts. The accuracy of the reconstructed damage based on the proposed algorithm was further studied. This paper also introduced an automatic 3D scanning process by integrating a structured-light 3D scanner with a Nachi industrial robot. The integration intends to realize the scanning automation to benefit the automated part repair process. Paper V analyzed the repaired part quality by microstructure characterization and mechanical testing. The purpose of this paper is to validate the successful repair of damaged components by the AM process, confirming the feasibility of the repair framework illustrated in Figure 1.1.

Five research papers in combination could solve potential crucial problems associated with metallic component remanufacturing, therefore, contributing to the industries and areas dealing with part repair. Each paper was presented in detail in the following of this dissertation.

PAPER**I. EXPERIMENTAL CHARACTERIZATION OF A DIRECT METAL DEPOSITED COBALT-BASED ALLOY ON TOOL STEEL FOR COMPONENT REPAIR****Xinchang Zhang¹, Tan Pan¹, Wei Li¹, and Frank Liou¹**¹Department of Mechanical and Aerospace Engineering,

Missouri University of Science and Technology, Rolla, MO 65409, USA

ABSTRACT

Casting dies made of tool steel are subject to impact, abrasion, and cyclic thermo-mechanical loading that can result in damage such as wear, corrosion, and cracking. To repair these defects, materials enveloping the defects need to be machined off and then refilled. In this study, V-shaped defects with varied sidewall inclination angles were prepared on H13 tool steel substrates and refilled with a cobalt-based alloy using direct metal deposition process (DMD) for superior hardness and wear resistance. The microstructure of rebuilt samples was characterized using an optical microscope (OM) and scanning electron microscope (SEM). Elemental distribution from the substrate to deposits was analyzed using energy-dispersive spectrometry (EDS). The mechanical properties of repaired samples were evaluated by tensile testing and microhardness measurement. A fracture mechanism in tensile testing was analyzed by observing the fracture surface. The experimental result reveals that V-shaped defects with sidewall beyond certain angles can be successfully remanufactured. The deposits were fully dense and free of defects. The

microstructure and tensile testing confirm the solid bonding along the interface. The tensile testing shows the average ultimate tensile strength (UTS) of the repaired samples is approximately 620 MPa, where samples fractured at the deposits region. The hardness measurement reveals the hardness of deposits is around 800 HV, which is much higher than the hardness of the substrate.

Keywords: Direct metal deposition; Component repair; Cobalt-based alloy; Tool steel

1. INTRODUCTION

Direct metal deposition (DMD) is an AM process that was developed recently but applied widely in the fields of fabricating prototypes and end-use parts [1-4], coating on easy-to-wear surfaces for enhanced abrasive resistance [5-9], joining varied materials and functionally graded materials [6], [10-12], depositing high-entropy alloys [13, 14], and repairing valuable components [15-21]. For repair purpose, the damaged region can be coated with hard surfacing alloys through the DMD process to modify the properties to improve hardness, wear, and corrosion resistance. In this way, the damaged components can be restored and reinserted into service to prolong the service life of high-cost components such as titanium parts and dies/molds.

Research on cladding hard surfacing alloys such as nickel- and cobalt-based alloys and WC composite on steels have been conducted. Paul et al. reported in [22] that they successfully deposited fully dense and crack-free W-C-Co coatings on low carbon steel using pulsed Nd: YAG laser with excellent interfacial bonding and significantly improved the hardness. Chen and Xue cladded CPM tool steel on H13 tool steel for enhancing

abrasive wear resistance [23]. Zhong et al. investigated the microstructure evolution during laser cladding of mixture of Stellite 6 and WC powder. In the coating of W-C-Co alloys on medium carbon steel, defects including porosities and cracks were observed in the clad layers mainly owing to gas entrapped in clad layers and stress concentration [24]. By depositing spherotene tungsten carbides on low carbon steel in [25], the researchers found a uniform distribution of hard particles in coatings with a hardness around 1000-1500 HV. Investigators in [26] clad 1.0- to 3.3-mm-thick cobalt-based alloy coatings on cast iron by optimizing processing parameters. The as-deposited material disclosed a crack-free structure and a good mechanical performance.

Cracking is a common failure in metal parts that can be caused by overload and fatigue. However, repairing cracking is not straightforward because the defects cannot be simply removed by refilling materials on the gap region. To repair these defects, a slot or groove needs to be machined to remove materials around cracking to reveal a regular and accessible geometry [27, 28]. It should be noticed that during machining, the slot and the sidewall inclination angle of the slot should be carefully determined. This is because the sidewall tilt angle can affect the bonding condition between the filler material and substrate. A small tilt angle gives a better opening area that assures better accessibility of the defective area but may result in much more material removal. Considering the machined-off material needs to be deposited back through the DMD process, a large volume of removed materials wastes time and effort. A large sidewall inclination angle makes the sidewall steeper. In the DMD process, if the sidewall is too steep, the laser has difficulty melting materials on the sidewall, where this situation can be observed in [29]. As a consequence, the as-deposited material cannot be fused well with the substrate and

the metallurgical bonding between these two materials at such areas cannot be guaranteed. Therefore, the slot sidewall inclination angle should be investigated to assure a minimum machined material to remove cracking and assure the solid interfacial bonding.

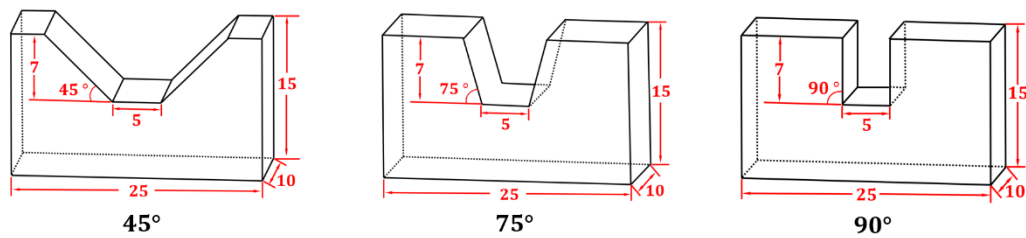
This article has two objectives. At first, it aims to investigate the feasibility of direct metal deposition of a Co-Ni-Cr-W alloy Wallex 50 on H13 tool steel for repair dies/molds to assure longer wear and corrosive life. On the other hand, this article tries to clarify the influence of sidewall inclination angle on the properties of repaired parts. To perform the repair, V-shaped defects with a sidewall inclination angle of 45°, 75°, and 90° were prepared on H13 tool steel substrates. The repair volume on each substrate was reconstructed by scanning the damaged part using a structured-light 3D scanner. After that, the missing geometry was sliced into layers to generate a raster deposition tool path. Wallex 50 alloy was refilled into the defective area to restore the missing geometry. To evaluate the quality of the repaired specimens, macrostructure examination, microstructure characterization, EDS analysis, tensile testing, and microhardness measurement were performed on the repaired samples. A detailed discussion of the properties based on these tests was illustrated.

2. EXPERIMENTAL PREPARATION

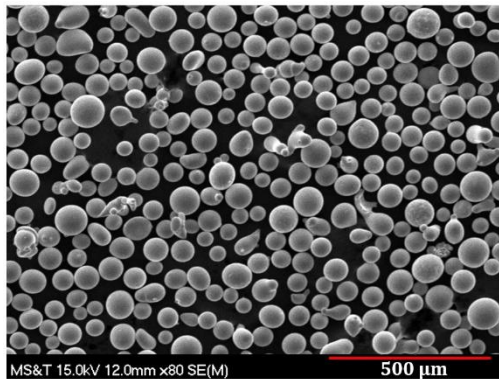
2.1. MATERIALS

H13 hot work tool steel is a common material used for fabricating aluminum casting dies/molds owing to its great thermal fatigue cracking resistance. In this study, H13 tool steel blocks with dimensions of 25 mm × 10 mm × 15 mm were prepared as the substrate.

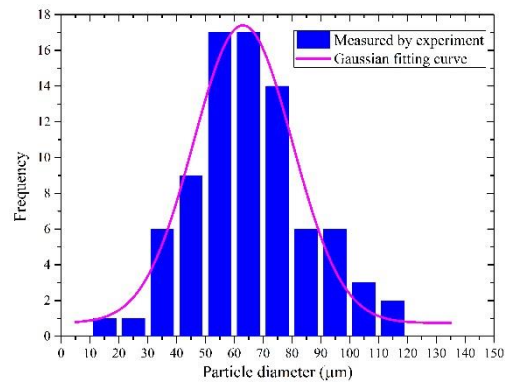
To perform repair experiments, several V-shaped grooves with varied sidewall inclination angles were machined on each substrate. Three sidewall inclination angles of 45° , 75° , and 90° were chosen, which are depicted in Figure 1a. The depth of each groove is 7 mm, and the width of defects at the bottom is 5 mm.



(a)



(b)



(c)

Figure 1. (a) Dimensions of the prepared substrates with V-shaped grooves of 45° , 75° , and 90° sidewall inclination angle; SEM micrograph (b) and particle size distribution (c) of Wallex 50 alloy powder

Co-Ni-Cr-W alloy Wallex 50 is selected as the filler material owing to its excellent corrosion resistance and low coefficient-of-friction, providing good metal-to-metal wear

protection. Wallex 50 alloy has high contents of Co, Ni, Cr, and W to guarantee a high hardness as well as good corrosive resistance. Wallex 50 alloy can be coated on the easy-to-wear surface on H13 tool steel dies to improve resistance to wear. The chemical composition of Wallex 50 and H13 tool steel is collected in Table 1. Wallex 50 alloy powder was characterized to analyze particle shape and size distribution. An SEM micrograph of Wallex 50 alloy powder was obtained in Figure 1b. The image shows that most particles are spherical although a few irregular shaped powders are detected. Particle size distribution in Figure 1c analyzed using ImageJ shows the average particle diameter is 65 μm .

Table 1. The chemical composition of the target materials (wt.%)

Materials	C	Mn	Si	Cr	Ni	Mo	V	W	B	Fe	Co
H13 tool steel	0.4	0.4	1.0	5.25	-	1.35	1.0	-	-	Bal.	-
Wallex 50	0.8	-	2.75	19	18	-	-	10	3.4	1.0	Bal.

2.2. EXPERIMENTAL SETUP

The geometry of the missing region on each substrate should be determined to obtain the deposition tool path. This deposition tool path directly determines the geometry of the restored parts and has great influences on the mechanical properties of deposits. It is needed to acquire the missing volume accurately so that the parts can be repaired. To obtain the refill volume, a structured-light 3D scanner (OptimScan 5M, Shining 3D Tech.) in

Figure 2a was adopted to perform the model reconstruction. The principle of the structured-light 3D scanner is shown in Figure 2a where a pattern with stripes was projected on an object by the projector and two CCD cameras capture distortions of the pattern. The distortion data outputs the 3D geometry of the scanned object.

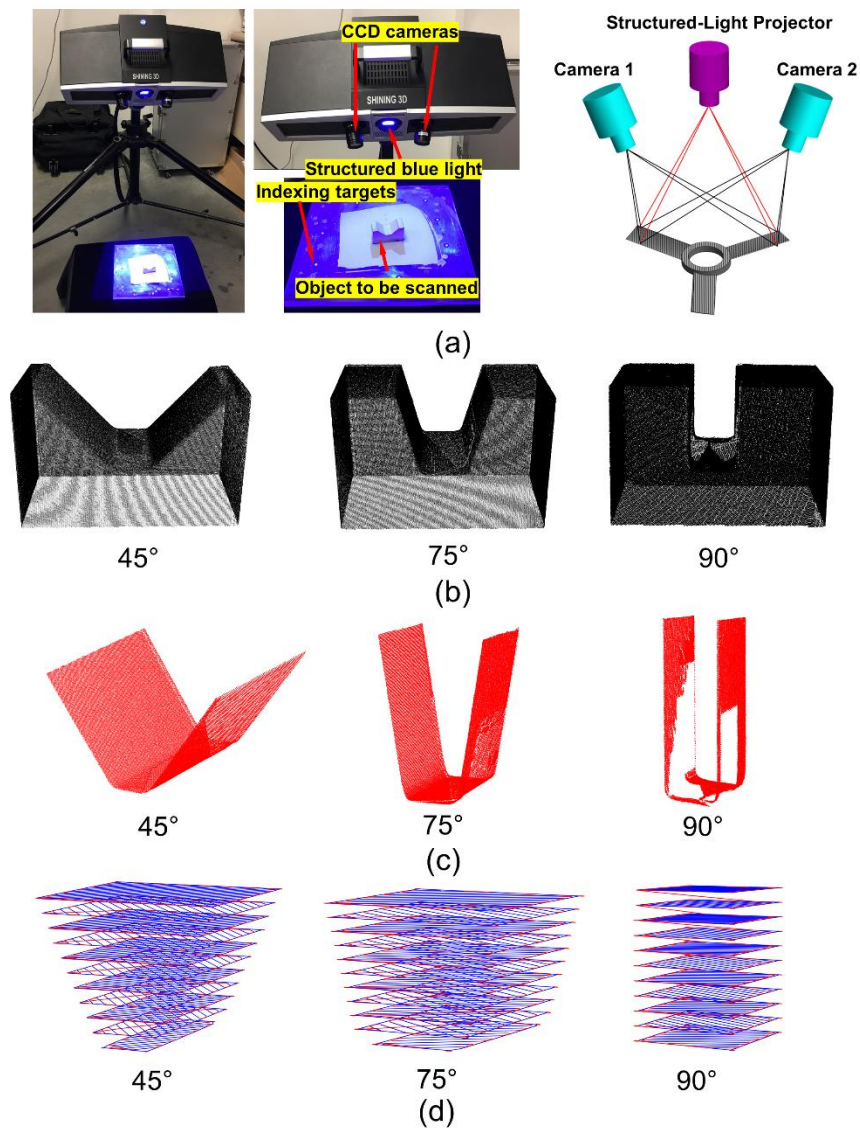


Figure 2. Model reconstruction for tool path generation. (a) 3D scanning setup; (b) Reconstructed point cloud; (c) Extracted damaged points; (d) Repair tool path

The scanning process was conducted on each substrate, and the scanned point cloud was illustrated in Figure 2b. Defining the points in the damaged region is simply conducted by calculating the distance between each scanned point to the top nominal surface of each substrate. After searching for damaged points, the repair geometry was acquired and is depicted in Figure 2c. One can see in Figure 2c that the damage for the sample with 90° sidewall defects was not completely scanned because the vertical sidewall combined with narrow slot blocks the two cameras from capturing projected pattern simultaneously. However, these uncomplete scanned points have no effect on the additive tool path generation because the tool path generation algorithm relies on the convex-hull of the data set, which is described below.

After the missing geometry was obtained, adaptive deposition tool path was generated based on damaged point cloud using the algorithm introduced in [30]. Each geometry was sliced into 11 layers with a layer thickness of 0.6 mm. The deposition tool path is shown in Figure 2d. For each layer, the deposition tool path was planned with an outline contour and raster infill pattern, indicating laser moves along the enveloping boundary and then along the zigzag pattern to acquire fully dense deposits.

Once the additive tool path was acquired, each damaged substrate was loaded to the DMD system for material deposition. The DMD system includes a 1-KW continuous wave (CW) fiber laser, blown powder feeder (Model 1200, Bay State Surface Tech., Inc.), 3-axis work table, and argon gas feeding components. The beam diameter of the CW laser is 1.8 mm. The laser beam is tilted with an angle of 20° to the vertical axis, while the powder feed nozzle is vertical with a stand-off distance of 10 mm above the substrate. The material fusing process was performed in a closed chamber filled with argon gas to keep

deposited beads from oxidization. The processing parameters were summarized in Table 2.

Table 2. Material deposition processing parameters

Laser Power (W)	Powder Flow Rate (g/min)	Layer Thickness (mm)	Scan Speed (mm/min)	Overlap
350	3.2	0.6	220	0.5

2.3. SPECIMEN PREPARATION AND MATERIAL CHARACTERIZATION

As-deposited samples were sectioned using a Hansvedt electrical discharge machine (EDM) and mounted on Bakelite using Simplimet 1000 mounting equipment. Specimens were ground using abrasive papers from 120 Silicon Carbide Grid to 1200 Grid and then polished using 0.05 μm silica suspension and finally ultrasonically cleaned for 30 min. The prepared samples were macroscopic analyzed using a HIROX KH-8700 optical microscope to study the interfacial boundary between refilled material and substrates. The microstructure of deposits near the interface was revealed using a Hitachi S4700 Scanning Electron Microscope (SEM). An EDS line scan was performed from deposits to substrates to analyzed elemental composition and distribution.

Tensile testing and hardness measurement of the repaired specimens were also conducted to test the mechanical properties. For preparing tensile specimens, several thin layers were cut from each repaired substrate. Then the tensile specimens were sectioned from each thin slice. Each tensile specimen consists of deposits and substrate, with

interface locating at the middle of the specimen. The tensile test was conducted using an Instron tester with a crosshead speed of 0.015 mm/min. Ultimate tensile strength was obtained, and then the tensile fracture surface was analyzed. Vickers hardness was measured using a Struers Duramin hardness tester with a press load of 9.81 N and dwell time of 10s.

3. RESULTS AND DISCUSSION

3.1. MACROSTRUCTURE EXAMINATION

The overview of the repaired samples is shown in Figure 3a. Before inspecting the inner material, it seems that the missing volume on all substrates was refilled by filler material successfully. The height of the as-deposited material is higher than the substrate. This can be attributed to the entrapped powder in the defective V-groove. Powders delivered into the melt pool cannot be melted completely. A portion of the delivered metal powders was melted and solidified on the substrate while the unmelted powders were accumulated in the area. Because of the concave shape, powders were entrapped in the geometry, melted and solidified in the next layers of deposition, causing the mountain-shaped geometry. To investigate the inner material, the repaired samples were sectioned and further inspected.

The optical micrographs of cross sections of the repaired samples are depicted in Figure 3b. Micrographs were taken at the boundary of deposits and substrates. The bonding line is very clear and free of defects for 45° and 75° samples, while a large number of porosities and lack of fusion were observed in the sample with 90° damage. Those defects

were almost entirely located along the vertical sidewall boundaries. In the bottom region of the 90° sample, the deposits are still bonded well with the substrate. This phenomenon is expected because, for a vertical sidewall, the laser cannot continuously melt the materials at the vertical side of the defects but can still effectively melt materials on the bottom region. Thus, the melt pool cannot be successfully formed at vertical regions and filler materials were not able to be melt and deposited. This situation might become worse when the defect is deep and the open neck is narrow.

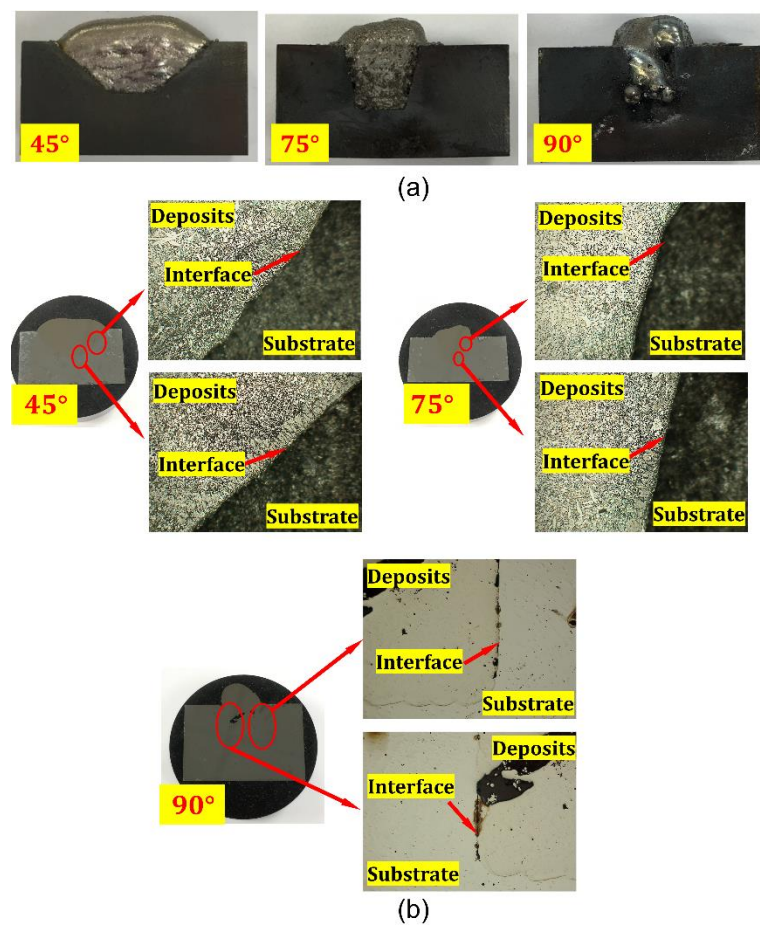


Figure 3. (a) Overview of the repaired samples; (b) Optical micrographs of cross-sections of the repaired samples

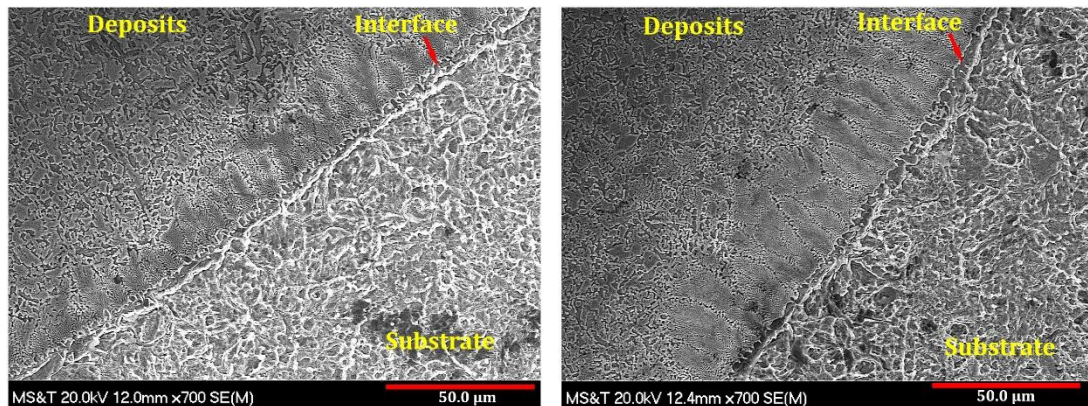
Through macrostructure examination, one can see that it is necessary to tilt the sidewall so that laser can melt the materials on the nearly vertical surfaces. Sidewall with 75° tilt angle is sufficient to guarantee the solid bi-material interfacial bonding. Further tilting the sidewall may increase the volume of the machined-off material. Because the cut-off volume needs to be re-deposited, removing more materials is not suggested.

3.2. MICROSTRUCTURE AND EDS ANALYSIS

Considering the damaged substrate with 90° sidewall tilt angle was not repaired successfully, only restored samples with 45° and 75° sidewall damage were further analyzed in terms of microstructure, elemental distribution, and mechanical properties. Figure 4a and 4b reveal the microstructure of materials near the bi-material bonding area for samples with 45° and 75° sidewall damage, respectively. One can see that the bonding line between as-deposited material and the substrate is very clear. The materials on the opposite side of the bonding line show different microstructures. There is no smooth transitional zone passing the interface of the two materials. Through observation, it is revealed that the bonding is solid and there are no defects like cracks and gas pores around the interfacial area. The SEM micrographs show that the filler material was metallurgically fused with the substrate. This solid bonding can also be validated in the tensile test in the following of this article.

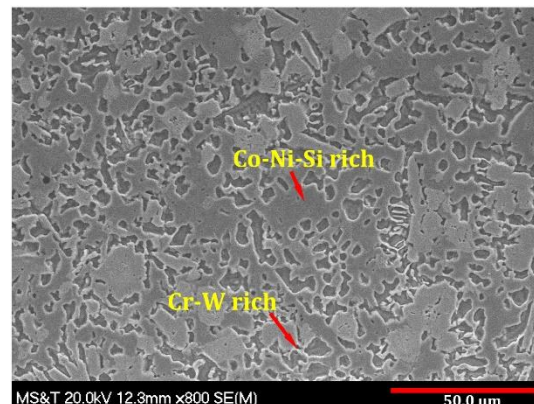
The SEM micrographs in Figure 4 depict that the microstructure of the as-deposited Wallex 50 near the interface show mostly a columnar structure stretched toward the center of deposits perpendicular to the bonding line. These grains were growing parallel to the heat flow direction during solidification. At the deposition starting stage for the first few

layers, the substrate was at a relatively low temperature. When the laser scanned on the substrate to create a melt pool, the solidification rate is extremely high. This high cooling rate causes the grains at such few layers growing in a columnar structure. The cooling rate is so high that leaves not sufficient time for grains to form secondary dendrites. As materials deposited layer by layer, the solidification rate dropped and the microstructure of deposits gradually changed to dendrite with interdendritic eutectics.



(a)

(b)



(c)

Figure 4. SEM micrographs of the boundary area of samples with 45° (a) and 75° (b) sidewall damage; (c) micrograph of top layers of the sample with 45° sidewall damage

The microstructure of the top layers of as-deposited Wallex 50 alloy is presented in Figure 4c, which consists of mostly interdendritic eutectics. It was observed that the gray region was enveloped by bright phases. The EDS spectrum shows the bright region was rich in Cr and W and the gray area is dominated by Co, Ni, and Si.

An EDS line scan was performed on the repaired specimens to investigate elemental composition and distribution. The line scan was initiated from the as-deposited Wallex 50 and terminated in the area of the H13 tool steel, passing the bi-material interface. Major elements including Co and Fe were quantified along this route. Dwell time for each point was 200 ms. The acquired data are plotted in Figure 5.

The EDS line scan exhibits that the major elements like Co and Fe were quickly changed from the deposit region to the substrate. A diluted zone can be seen at the interface. In this region, the quantity of Co is gradually increasing while the amount of Fe is decreasing. This can be attributed to that when a melt pool was formed on the substrate, cobalt-based alloy Wallex 50 was injected in the melt pool and mixed with the melted H13 tool steel material. After solidification, mixture of Wallex 50 and H13 tool steel was formed at the interfacial area. This material mixture results in the transition of the elemental composition near the interface. A large amount of Fe exists in the first few layers of deposits, showing the dilution of Fe into Wallex 50 and contributes to the phase transformation over the interface. There is almost no influence of sidewall tilt angle on the transition of elements at the boundary. Therefore, once materials are fused together, similar elemental composition trend can be obtained. The EDS line scan also confirms that excellent metallurgical bonding was created along the interface. Both materials were metallurgically instead of mechanical joined, showing the mixing compatibility.

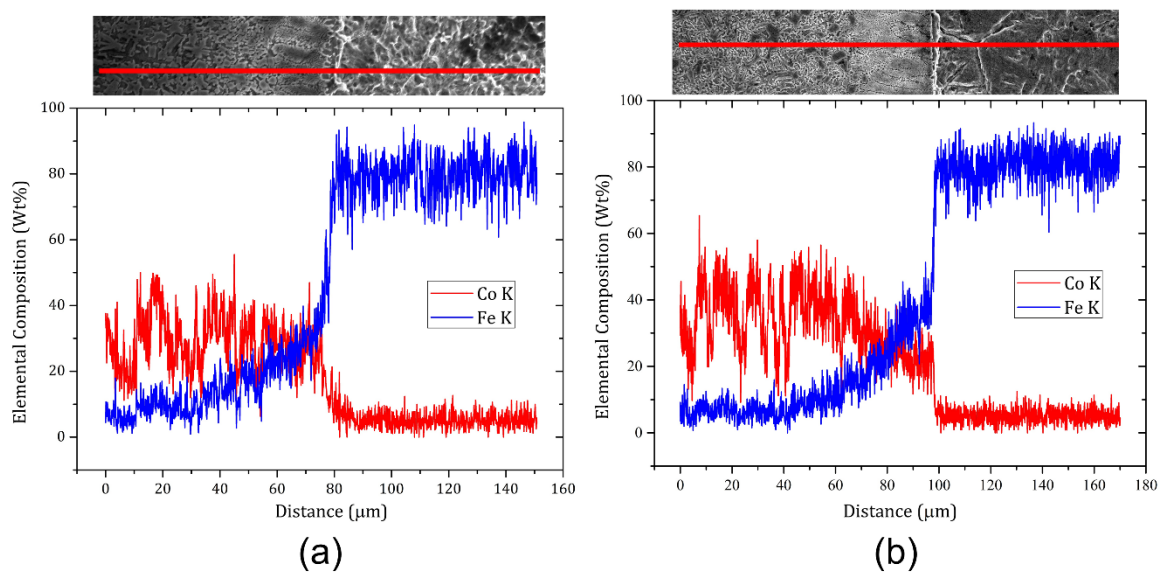


Figure 5. EDS line scan result for samples with 45° (a) and 75° (b) sidewall damage

3.3. TENSILE TESTING OF THE REPAIRED SAMPLES

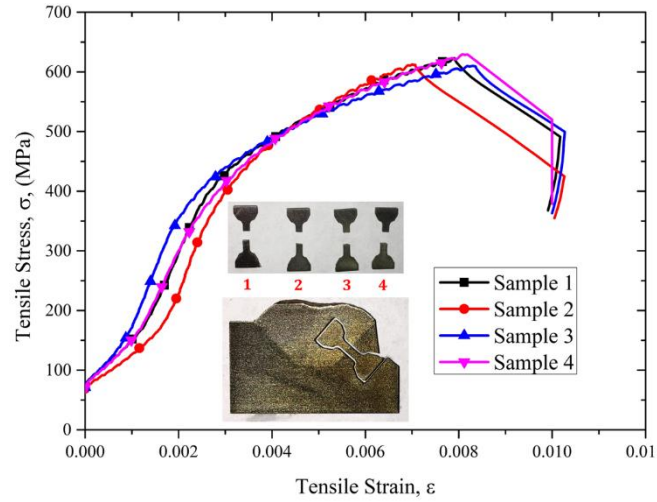
Four tensile specimens were cut from each repaired sample. The tensile stress-strain curves were plotted in Figure 6, the ultimate tensile strength (UTS) is summarized in Table 3, and the tensile fracture surface is in Figure 7. The tensile stress-strain curves reveal that the tensile stress increased with the increase of tensile strain to a peak stress of approximately 620 MPa. Then the tensile samples fractured abruptly. The stress-strain curves did not reveal yielding phenomenon during the tensile testing. The ductility of the tensile samples was extremely low. Further investigation reveals all samples fractured at the as-deposited Wallex 50 region. Therefore, the as-deposited Wallex 50 alloy shows a brittle fracture mechanism.

The average UTS of the repaired samples with 45° and 75° V-shaped defects is approximately 618 MPa and 624 MPa, respectively. The tensile testing reveals the

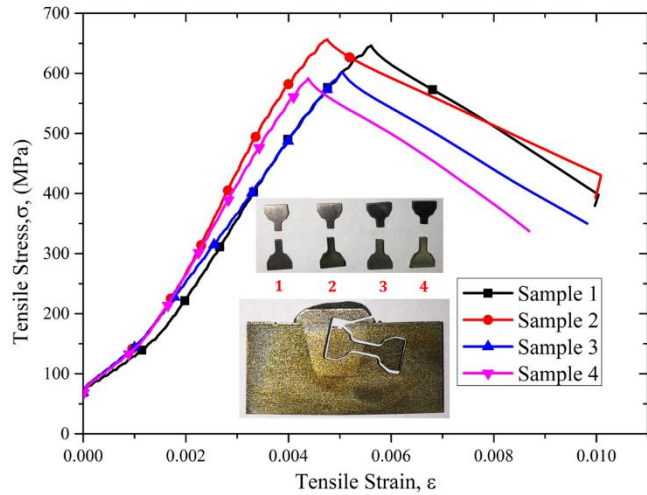
influence of sidewall inclination angle on the UTS is barely recognizable. This result shows that as long as the deposited material bonded well with the substrate, the tensile strength of the repaired sample is relatively consistent. There is a substantial variation of UTS in the tensile result. This variation was possibly attributed to the unevenly located defects in the deposited regions. Some micropores in deposits may affect the UTS and result in the large standard deviation. The strain at UTS for 45° sample is slightly higher but not more substantial than the strain at UTS for 75° sample.

Table 3. UTS obtained from tensile testing

Sidewall angle	Specimen	UTS (MPa)
45°	1	623.06
	2	612.12
	3	610.00
	4	629.46
	Average	618.66
	S.D.	9.19
	75°	1
2		656.36
3		602.61
4		591.73
Average		624.23
S.D.		31.83



(a)



(b)

Figure 6. Tensile stress-strain curves for samples with 45° (a) and 75° (b) damage

The micrographs of the tensile fracture surface are depicted in Figure 7a-d. The overview image in Figure 7a reveals a flat surface that is perpendicular to the tensile loading direction. Magnified view in Figure 7b-d shows microscopically unsmooth areas. Microcracks were observed at such magnified micrographs. A very limited population of

voids and dimples were observed, indicating the brittle fracture of the tensile specimens. The brittle mechanism of as-deposited Wallex 50 can be caused by the chemical composition of the material. Wallex 50 is a cobalt-based alloy that consists of a large number of hard elements including Cr, W, Si that can form very hard phases, resulting in the brittle failure mechanism.

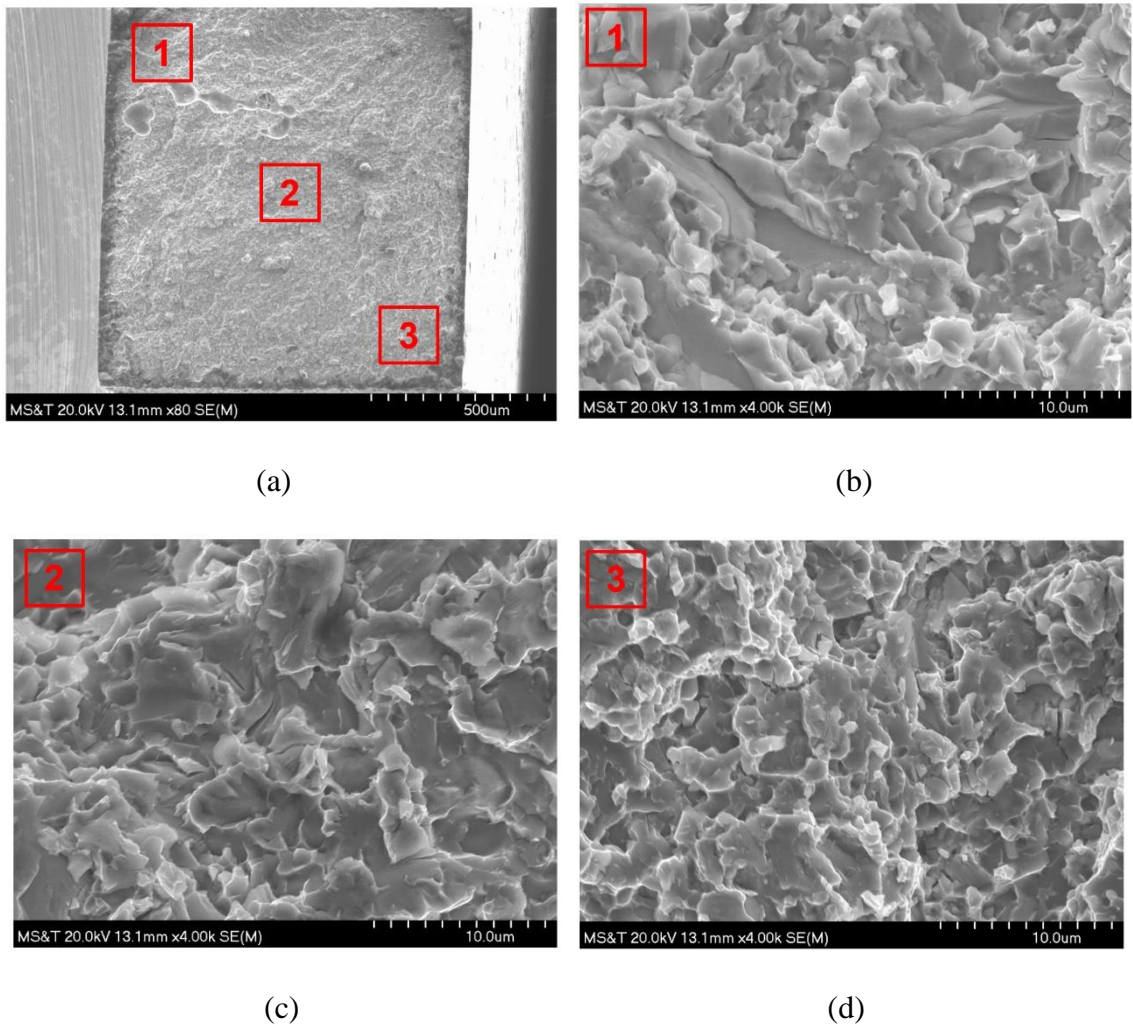


Figure 7. Tensile fracture morphology. (a) Overview of the fracture surface; (b) Magnified view of area 1 in (a), (c) Magnified view of area 2 in (a), (d) Magnified view of area 3 in (a)

3.4. MICROHARDNESS MEASUREMENTS

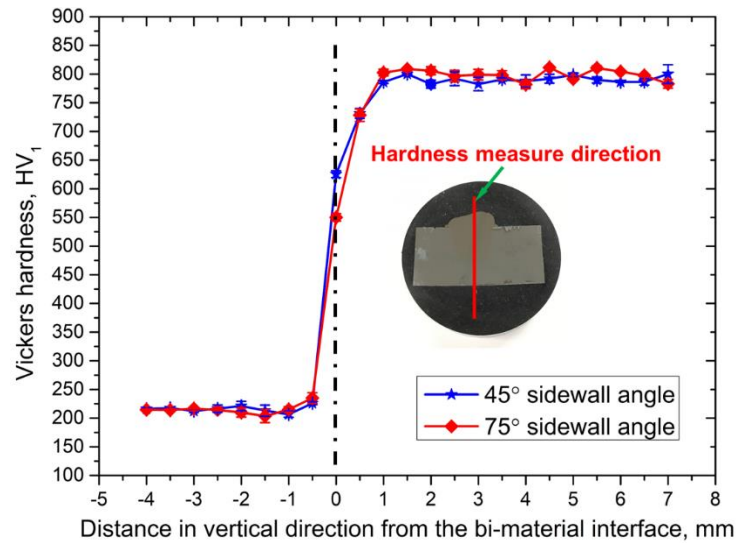
Vickers hardness along two paths was measured on the cross sections of the repaired samples. One is in the vertical direction from as-deposited Wallex 50 to substrate as shown in Figure 8a. Another one is in the horizontal direction passing through substrate, deposits, and substrate, which is shown in Figure 8b.

It is obvious to find out that the hardness of deposits is much higher than the hardness of the substrate. The hardness of the H13 tool steel substrate is approximately 210 HV, while the hardness of as-deposited Wallex 50 is 800 HV, which is almost four times the hardness of the substrate. H13 tool steel used for casting dies is in quenched and tempered condition and usually has a hardness range of 480 – 520 HV. The as-received H13 tool steel used in this research is in an annealed condition that results in the lower hardness of only 210 HV. However, it can be seen that the hardened of H13 tool steel also shows lower hardness values compared with the deposits.

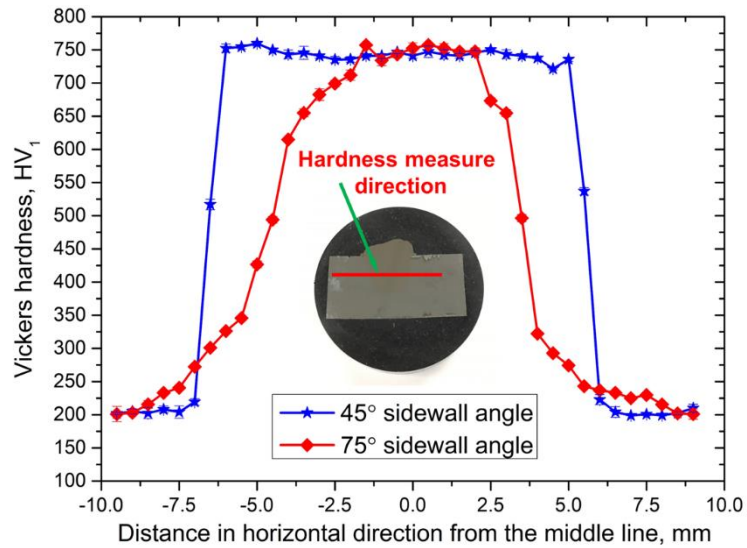
The hardness in the vertical direction depicted in Figure 8a shows a sharp increment at the interface. The transitional distance from lower hardness to a higher hardness is approximately 1.5 mm, which can be linked to the dilution zone. The hardness of deposits from two samples shows consistent and equal values. In the horizontal direction illustrated in Figure 8b, the hardness jumped sharply passing the interface for 45° sidewall damaged sample. For the 75° sidewall sample, however, the hardness increased relatively smoothly.

The sharply increased hardness on the deposits is mainly caused by two reasons. The major reason is that Wallex 50 is a cobalt-based Co-Ni-Cr-W alloy. The cobalt-rich matrix with very hard phases results in the very high hardness. In addition, the cooling rate

during material deposition is extremely high, leading to the formation of the fine microstructure that contributes to the hardening.



(a)



(b)

Figure 8. Vickers hardness distribution. (a) Microhardness measurement in a vertical direction; (b) Microhardness measurement in a horizontal direction

4. CONCLUSION

In this research, Co-Ni-Cr-W hard surfacing alloy Wallex 50 was deposited on H13 tool steel for repair purpose. To perform the repair, V-shaped grooves with a different sidewall inclination angle of 45°, 75°, and 90° were prepared on substrates. For generating the deposition tool path, each substrate with damage was scanned to obtain the 3D model. Damaged points were extracted to provide the missing volume. Once the missing volume was obtained, it was sliced into layers to generate a raster deposition tool path. Wallex 50 particles were injected into the repair zone to restore the missing geometry. To test the properties of the repair samples, macrostructure examination, microstructure, and EDS analysis, tensile testing and microhardness measurement were performed and evaluated.

The macrostructure examination reveals that the samples with 45° and 75° sidewall damage were repaired successfully. For repairing the sample with 90° sidewall damage, since the laser was not able to melt the materials in the vertical zone, filler material was not bonded well with the substrate, causing lack of fusion and a large number of pores. The microstructure of deposits near the interface shows a mostly columnar structure due to the rapid cooling for the first few layers. As materials deposited layer by layer, the microstructure was transformed into the equiaxed structure. The EDS line scan confirms expected elemental distribution from the substrate to deposits. Microstructure and EDS analysis confirm the metallurgical bonding along the interface.

Tensile testing of repaired samples reveals a UTS of approximately 620 MPa where samples fractured at the as-deposited Wallex 50 region. The influence of sidewall inclination angle on the UTS is not observed. The tensile stress-strain curves and fracture

surface show the brittle failure of the tensile specimens. The hardness measurement reveals the hardness of deposits and the substrate is about 800 HV and 210 HV, respectively. The hardness values changed rapidly in a vertical direction no matter the sidewall angle, while they changed smoothly in the horizontal direction for 75° sidewall sample compared to the 45° sidewall sample.

ACKNOWLEDGMENTS

This project was supported by NSF Grants CMMI-1547042 and CMMI-1625736, and the Intelligent Systems Center, Center for Aerospace Manufacturing Technologies, and Material Research Center at Missouri S&T. Their financial support is greatly appreciated.

REFERENCES

- [1] Y. Ding and R. Kovacevic, "Feasibility Study on 3-D Printing of Metallic Structural Materials with Robotized Laser-based Metal Additive Manufacturing," *JOM*, vol. 68, pp. 1774-1779, 2016.
- [2] N. Hopkinson and P. Dickens, "Rapid Prototyping for Direct Manufacture," *Rapid prototype Journal*, vol. 7, pp. 197-202, 2001.
- [3] K. Zhang, S. Wang, W. Liu, and X. Shang, "Characterization of Stainless Steel Parts by Laser Metal Deposition Shaping," *Materials & Design*, vol. 55, pp. 104-119, 2014.
- [4] E. C. Santos, M. Shiomi, K. Osakada, and T. Laoui, "Rapid Manufacturing of Metal Components by Laser Forming," *International Journal of Machine Tools and Manufacture*, vol. 46, pp. 1459-1468, 2006.
- [5] P. Suresh Babu, Y. Madhavi, L. Rama Krishna, D. Srinivasa Rao, and G. Padmanabham, "Thermally-Sprayed WC-based Cermet Coatings for Corrosion Resistance Application," *JOM*, vol. 70, pp. 2636-2649, 2018.

- [6] R. M. Mahamood, E. T. Akinlabi, M. Shukla, and S. Pityana, "Scanning Velocity Influence on Microstructure, Microhardness and Wear Resistance Performance of Laser Deposited Ti6Al4V/TiC Composite," *Materials & Design*, vol. 50, pp. 656-666, 2013.
- [7] F. Weng, H. Yu, C. Chen, J. Liu, L. Zhao, J. Dai, and Z. Zhao, "Effects of Process Parameters on Microstructure Evolution and Wear Property of the Laser Cladding Coating on Ti-6Al-4V Alloy," *Journal of Alloys and Compounds*, vol. 692, pp. 989-996, 2017.
- [8] L. Thivillon, P. Bertrand, B. Laget, and I. Smurov, "Potential of Direct Metal Deposition Technology for Manufacturing Thick Functionally Graded Coatings and Parts for Reactors Components," *Journal of Nuclear Materials*, vol. 385, pp. 236-241, 2009.
- [9] G. P. Dinda, A. K. Dasgupta, and J. Mazumder, "Laser Aided Direct Metal Deposition of Inconel 625 Superalloy: Microstructural Evaluation and Thermal Stability," *Materials Science and Engineering: A*, vol. 509, pp. 98-104, 2009.
- [10] W. Li, L. Yan, X. Chen, J. Zhang, X. Zhang, and F. Liou, "Directed Energy Depositing a New Fe-Cr-Ni Alloy with Gradually Changing Composition with Elemental Powder Mixes and Particle Size' Effect in Fabrication Process," *Journal of Materials Processing Technology*, vol. 255, pp. 96-104, 2017.
- [11] W. Li, X. Chen, L. Yan, J. Zhang, X. Zhang, and F. Liou, "Additive Manufacturing of a New Fe-Cr-Ni Alloy with Gradually Changing Compositions with Elemental Powder Mixes and Thermodynamic Calculation," *International Journal of Advanced Manufacturing Technology*, vol. 95, pp. 1013-1023, 2018.
- [12] W. Li, J. Zhang, X. Zhang, and F. Liou, "Effect of Optimizing Particle Size on Directed Energy Deposition of Functionally Graded Material with Blown Pre-Mixed Multi-Powder," *Manufacturing Letters*, vol. 13, pp. 39-43, 2018.
- [13] V. Ocelík, N. Janssen, S. N. Smith, and J. T. M. De Hosson, "Additive Manufacturing of High-Entropy Alloys by Laser Processing," *JOM*, vol. 68, pp. 1810-1818, 2017.
- [14] W. Cui, X. Zhang, and F. Liou, "Additive Manufacturing of High-Entropy Alloy – A Review," *Solid Freeform Fabrication Symposium Conference, Texas*, pp. 712-724, 2017.
- [15] X. Zhang, W. Li, X. Chen, W. Cui, and F. Liou, "Evaluation of Component Repair using Direct Metal Deposition from Scanned Data," *International Journal of Advanced Manufacturing Technology*, vol. 95, pp. 3335-3348, 2018.

- [16] F. Liou, K. Slattery, M. Kinsella, J. Newkirk, H. Chou, and R. Landers, "Applications of a Hybrid Manufacturing Process for Fabrication of Metallic Structures," *Rapid Prototyping Journal*, vol. 13, pp. 236-244, 2007.
- [17] T. Petrat, B. Graf, A. Gumenyuk, and M. Rethmeier, "Laser Metal Deposition as Repair Technology for a Gas Turbine Burner Made of Inconel 718," *Physics Procedia*, vol. 83, pp. 761-768, 2016.
- [18] X. Zhang, W. Li, W. Cui, and F. Liou, "Modeling of Worn Surface Geometry for Engine Blade Repair using Laser-aided Direct Metal Deposition Process," *Manufacturing Letters*, vol. 15, pp. 1-4, 2018.
- [19] X. Zhang, W. Li, and F. Liou, "Damage Detection and Reconstruction Algorithm in Repairing Compressor Blade by Direct Metal Deposition," *International Journal of Advanced Manufacturing Technology*, vol. 95, pp. 2393-2404, 2018.
- [20] J. Bennett, R. Dudas, J. Cao, K. Ehmann, and G. Hyatt, "Control of Heating and Cooling for Direct Laser Deposition Repair of Casting Iron Components," *International Symposium on Flexible Automation Conference, Ohio*, pp. 229-236, 2016.
- [21] X. Zhang, W. Li, K. M. Adkison, and F. Liou, "Damage Reconstruction from Tri-Dexel Data for Laser-aided Repairing of Metallic Components," *International Journal of Advanced Manufacturing Technology*, vol. 96, pp. 3377-3390, 2018.
- [22] C. P. Paul, H. Alemohammad, E. Toyserkani, A. Khajepour, and S. Corbin, "Cladding of WC-12 Co on Low Carbon Steel using a Pulsed Nd: YAG Laser," *Materials Science and Engineering: A*, vol. 464, pp. 170-176, 2007.
- [23] J. Chen and L. Xue, "Laser Cladding of CPM Tool Steels on Hardened H13 Hot-Work Steel for Low-Cost-High-Performance Automotive Tooling," *JOM*, vol. 64, pp. 688-693, 2012.
- [24] Y. Yang and H. C. Man, "Microstructure Evolution of Laser Clad Layers of W-C-Co Alloy Powders," *Surface and Coatings Technology*, vol. 132, pp. 130-136, 2000.
- [25] J. M. Amado, M. J. Tobar, J. C. Alvarez, J. Lamas, and A. Yáñez, "Laser Cladding of Tungsten Carbides (Spherotene®) Hardfacing Alloys for the Mining and Mineral Industry," *Applied Surface Science*, vol. 255, pp. 5553-5556, 2009.
- [26] V Ocelík, U. de Oliveira, M. de Boer, and J. T. M. de Hosson, "Thick Co-based Coating on Cast Iron by Side Laser Cladding: Analysis of Processing Conditions and Coating Properties," *Surface and Coatings Technology*, vol. 201, pp. 5875-5883, 2007.

- [27] H. Paydas, A. Mertens, R. Carrus, J. Lecomte-Beckers, and J. T. Tchuindjang, "Laser Cladding as Repair Technology for Ti-6Al-4V Alloy: Influence of Building Strategy on Microstructure and Hardness," *Materials & Design*, vol. 85, pp. 497-510, 2015.
- [28] B. Graf, A. Gumenyuk, and M. Rethmeier, "Laser Metal Deposition as Repair Technology for Stainless Steel and Titanium Alloys," *Physics Procedia*, vol. 39, pp. 376-381, 2012.
- [29] A. J. Pinkerton, W. Wang, and L. Li, "Component Repair using Laser Direct Metal Deposition," *Proceedings of the Institution of Mechanical Engineers, Part B: Journal of Engineering Manufacture*, vol. 222, pp. 827-836, 2008.
- [30] R. Liu, Z. Wang, Y. Zhang, T. Sparks, and F. Liou, "A Smooth Toolpath Generation Method for Laser Metal Deposition," *Solid Freeform Fabrication Symposium Conference, Texas*, pp. 1038-1046, 2016.

II. DEVELOPMENT OF PRE-REPAIR PROCESSING STRATEGIES FOR LASER-AIDED METALLIC COMPONENT REMANUFACTURING

Xinchang Zhang¹, Wenyuan Cui¹, Leon Hill¹, Wei Li¹, and Frank Liou¹

¹Department of Mechanical and Aerospace Engineering,

Missouri University of Science and Technology, Rolla, MO 65409, USA

ABSTRACT

Remanufacturing worn metallic components can prolong the service life of parts that need frequent replacement but are extremely costly to manufacture, such as aircraft titanium components and casting dies. Additive manufacturing (AM) technology enables the repair of such valuable components by depositing filler materials at the worn area layer by layer to regenerate the missing geometry. In general, damaged parts would be inspected and pre-machined prior to deposition to remove oil, residue, oxidized layers or defects located in inaccessible regions. Besides, damaged parts may need re-hardening to restore nominal properties. Therefore, the motivation of this paper is to introduce pre-repair processing strategies, which includes pre-repair machining and heat-treatment. The pre-repair machining targets at common failures comprising surface indentations, erosion, corrosion, wear and cracking. The machining strategies for each type of defect were proposed. Each strategy takes the scanned model as input and the cut-off volume around the defects is defined by using different approaches. Machining toolpath and program were generated based on the cut-off volume and finally, damaged parts were machined. Pre-repair heat-treatment for re-hardening H13 tool steel was also introduced.

Keywords: Pre-Repair Processing; Part Repair; Defects; Additive Manufacturing

1. INTRODUCTION

Aircraft components and casting dies are subjected to premature failure due to impact with foreign objects, thermal fatigue cracking, erosion, corrosion, wear, etc. For obtaining improved performance and mechanical properties in a wide temperature range, such components are usually made of expensive alloys, i.e., titanium- or nickel-based alloys. Besides, most casting dies are extremely high-priced because of their complicated structure and manufacturing costs. Therefore, regular maintenance and repair are necessary to prolong their service life.

Laser-assisted additive manufacturing (AM) process for component repair has been becoming an effective candidate for part refurbishment due to its good fabricated material properties and solid bi-material bonding [1-3], feasibility of depositing a wide range of materials [4-9], high-accurate positioning and motion control using computer [10, 11], as well as easily control of processing parameters [12-14]. AM process can deposit materials on damaged components with different materials to form functional structure [15, 16]. AM has different names at various laboratories such as Direct Metal Deposition (DMD), Laser Engineered Net Shaping (LENS), Laser Metal Deposition (LMD), etc. The basic principle of such techniques is a solid freeform fabrication process which is characterized as a layer-by-layer deposition technology that can directly build near-net shape fully dense components from CAD drawings. For component repair, the laser beam was scanned on the target damaged area to generate a melt pool while a powder stream is injected into the

melt pool. The injected powder undergoes rapid melting and then solidifies on the damaged substrate when the laser jogs away. Layer by layer, the missing volume is reobtained. The shape of the deposits is directly controlled by moving the substrate along a pre-defined pattern. It has been widely reported that AM as a remanufacturing technique has shown great applications in automotive, aerospace and die casting industries [17-24].

It was reported in [25, 26] that an integrated remanufacturing process generally undergoes the following steps: (1) Pre-repair inspection and decision; (2) Additive patch extraction; (3) Subtractive patch extraction; and (4) Quality Inspection. This is a universal repair routine that applied to various metallic components with diverse defects.

(1) In detail, a damaged part will at first experience a complete inspection to assess the feasibility and economy of restoring it. Since there are a variety of defects such as cracks, dents, wear, erosion, distortion, etc., and possibility in locating at a wide range of positions, the inspection and decision making is highly a case to case basis. However, the crucial factors are limited which comprise accessibility of defects, the volume of damage, the geometry of the base structure and post-repair machining possibility.

(2) When repair is scheduled, the repair volume of the part is then extracted to generate additive toolpath. Damage extraction is a key to guarantee a successful repair because the refilled volume is directly determined by the additive toolpath. This process usually requires creating the damaged model through 3D scanning and then conducting a Boolean operation between the recreated damaged model with the nominal model. A few algorithms have been developed for regenerating the geometry of the worn-out area [11], [18], [25], [27], and [28].

(3) Subtractive machining succeeds the additive process since the as-deposited part may have unsatisfied surface roughness and inaccurate dimensions.

(4) In the quality inspection, the remanufactured part is checked for any appearance of defects to ascertain that the repair is successful. In addition, the restored part is 3D scanned and then compared with the nominal model to catch possible dimensional distortion due to errors in damage extraction, and heating and cooling introduced residual stress.

However, the abovementioned repair routine is not complete because, in general, worn components cannot be directly deposited without pre-repair machining. Ultrasonic cleaning or rinse can only remove surface oil or debris on worn parts but cannot remove materials surrounding inaccessible defects (such as cracks or defects in sharp corners) or contaminated materials on worn surfaces. Depositing materials on such regions cannot guarantee the interfacial bonding strength. Unsolid bonding could cause delamination when putting the part into service. Contaminated inclusion of filler material and base part decimates the mechanical properties and therefore leaves great threaten especially on key components such as aircraft turbine and compression blades. Therefore, this research introduced pre-repair machining before additive patch extraction to assure the repairability of the damaged part.

Another issue associated in component repair is that after serving for a large number of heating and cooling cycles, damaged parts could show lower mechanical properties, mainly due to fatigue failure. Therefore, proposing a re-hardening process to recover the nominal properties is essential.

The aim of this paper is to develop pre-repair processing methodologies for component repair. The purpose of the proposed methodologies aims to benefit the repair process by not only providing pre-repair machining strategies but also introducing pre-repair heat-treatment procedures.

2. PRE-REPAIR MACHINING STRATEGIES FOR SURFACE DENTS

The pre-repair machining procedure for surface impact defects such as dents, notches, grooves and material overcut is illustrated in Figure 1, which includes (1) Damaged part cleaning and pre-repair inspection; (2) Model reconstruction; (3) Cut-off volume definition; (4) Target geometry acquisition; (5) Pre-machining toolpath and NC code generation; and (6) Pre-repair machining. The procedure is summarized in this section and detailed discussed in sections 2.1 – 2.5.

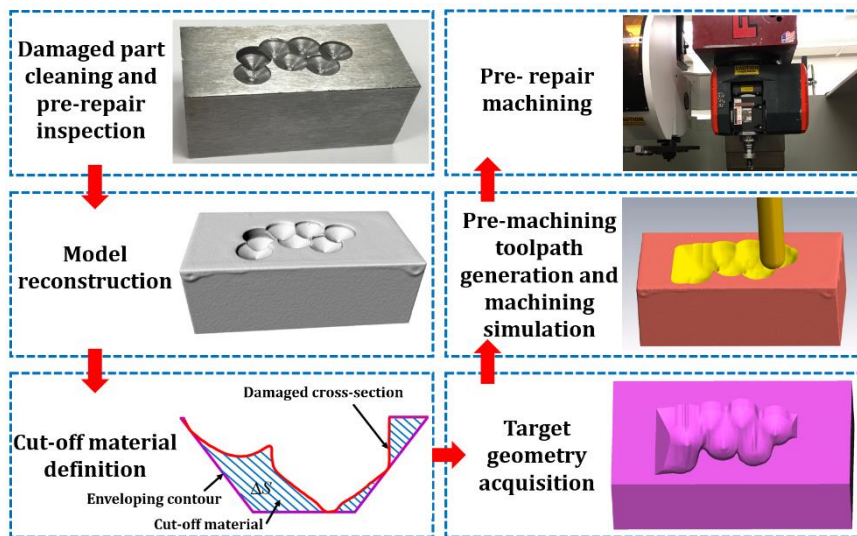


Figure 1. Pre-repair machining procedure for surface impact damage

In the beginning, the damaged part is throughout ultrasonic cleaned and inspected to determine the repair possibility. The inspection is mainly conducted by technicians due to the excess possible locations and geometries of different defects. When pre-repair machining is needed, the model of the damaged part is then reconstructed. After that, the volume of materials enveloping the damage is defined. Thereafter, the target geometry can be obtained to provide objective geometry for machining. Subsequently, based on the target geometry, pre-machining toolpath and NC node can be generated. The NC code can be exported to the machining system for machining.

2.1. DAMAGED PART CLEANING AND PRE-REPAIR INSPECTION

An H13 tool steel block with dimensions of 50 mm × 25.4 mm × 25.4 mm was utilized as an example for illustrating the pre-machining strategy of surface impact damage (Figure 2). Ball-indented defects were randomly prepared on the surface of the substrate using an 8 mm drill bit. The holes on the block have varied depths and overlap ratios.

One can see in Figure 2 that the damaged substrate cannot be repaired directly without pre-repair machining due to at least two reasons. One is that the vertical surfaces on the side of the holes are not accessible to the laser beam and powder feed nozzle for 3-axis system. Directly depositing materials on such areas cannot guarantee the sound bi-material bonding. Therefore, materials surrounding vertical surfaces need to be machined to reveal a tilt surface to guarantee accessibility. Another reason is that the rough tiny edges in the damaged area not only complicate the toolpath planning for material deposition but also may distort during deposition due to heat input that ruins the accuracy of deposited

geometry. Therefore, it is necessary to machine off a certain amount of materials enveloping the damage to provide a repairable geometry.

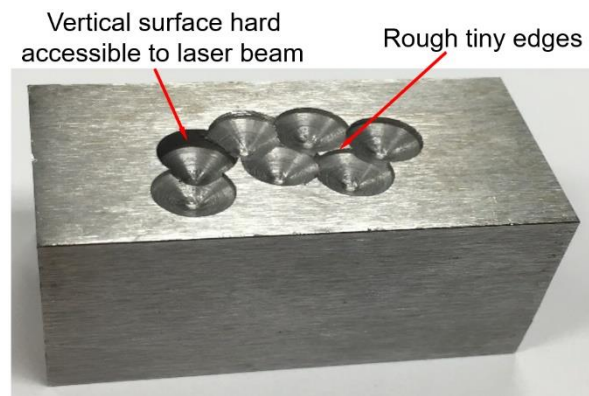


Figure 2. An H13 tool steel substrate with ball-indented damage on the top surface

2.2. MODEL RECONSTRUCTION OF A BLOCK

Recreating the model of the worn part is required for planning the pre-repair machining. In this research, models of damaged parts were reconstructed using a structured-light optical 3D scanner as shown in Figure 3 (Shining3D OptimScan-5M). The scanner has a blue light projector that emits structured-light patterns on an object and two CCD cameras on the scanner measure the distorted dimensions of the pattern. The alteration in dimensions provides the three-dimensional coordinates of the object. In order to acquire a complete model, multiple scans are demanded to capture different orientations of the object. For registering point cloud from different scans to a single model, indexing targets need to be randomly put around the object to be scanned. Figure 4a depicts the point

cloud of the substrate and the point cloud was further processed to create the STL model shown in Figure 4b.

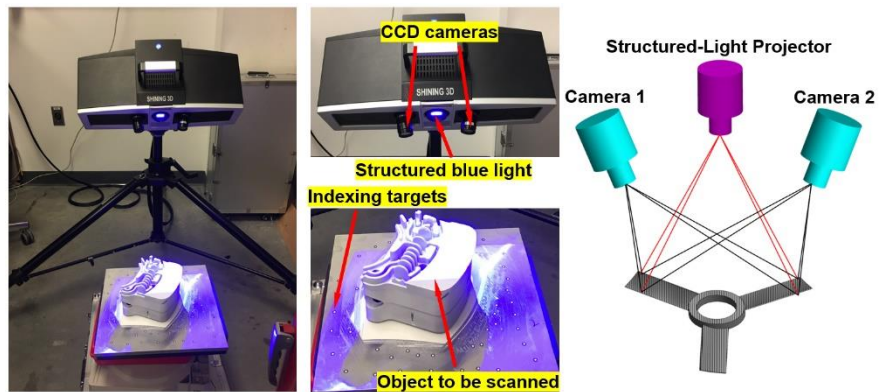


Figure 3. Structured-light 3D scanner for model reconstruction

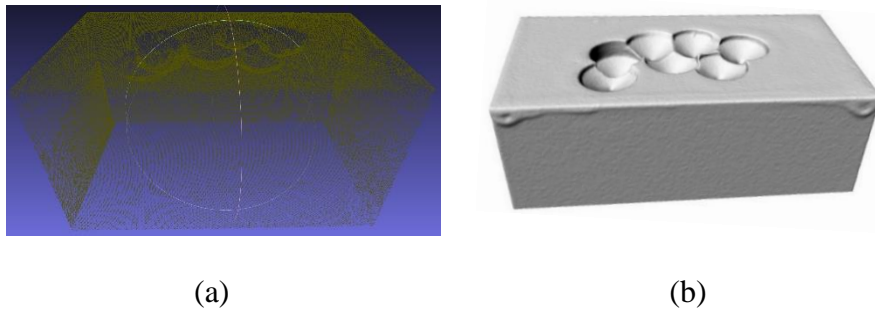
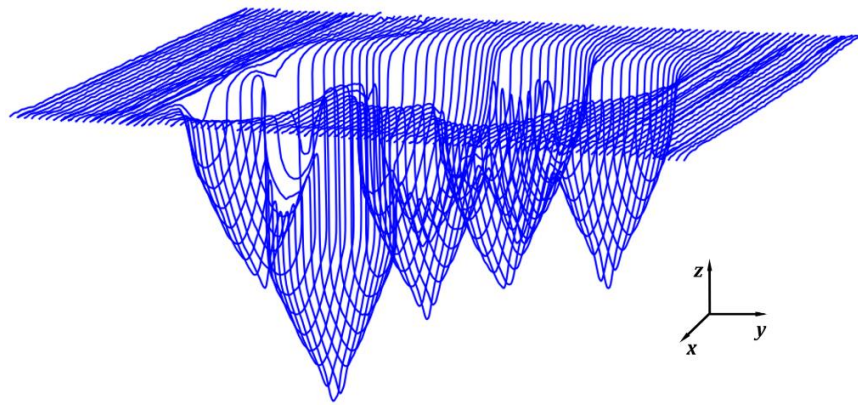


Figure 4. Point cloud (a) and reconstructed STL model (b) of the substrate

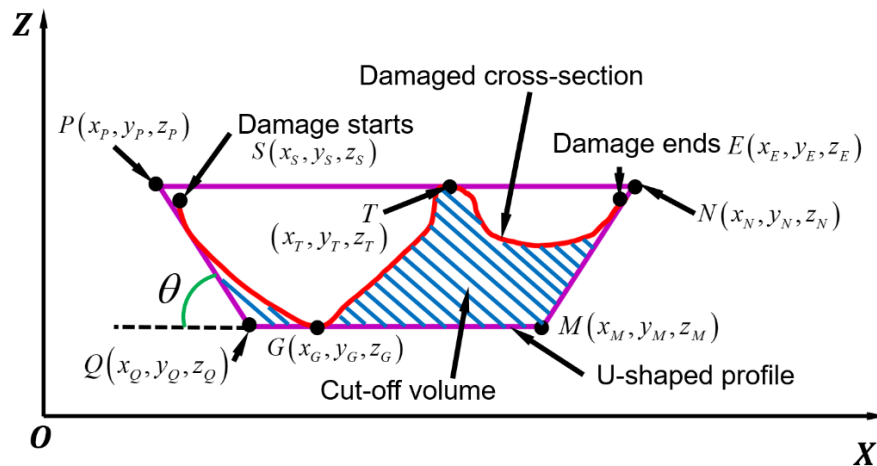
2.3. CUT-OFF VOLUME DEFINITION

The model of the damaged part was sliced into a number of layers along the y-axis with a layer thickness of 0.5 mm as shown in Figure 5a. The slicing outputs a series of

layers that combined damaged and undamaged cross-sections. Damaged cross-sections also contain points in damaged and undamaged regions. Damaged points can be extracted by calculating the distance from the points to the nominal surface. A tolerance can be set so that points with distance beyond the tolerance were defined as damaged points.



(a)



(b)

Figure 5. Model slicing and enveloping boundary determination. (a) Cross-sections of the damaged model; (b) U-shaped enveloping boundary

In order to machine off materials around the defects, based on the damaged cross-sections, two enveloping boundaries, U-shaped boundary and convex-hull boundary, were utilized. Both closed profiles contain the damaged area and surrounding materials to provide good accessibility to the AM system.

2.3.1. U-Shaped Boundary Definition. As shown in Figure 5b, for U-shaped contour, two approaching lines with an inclination angle θ (PQ on the left and MN on the right) were utilized to approach the damaged cross-section. The damage starting point $S(x_S, y_S, z_S)$ and ending point $E(x_E, y_E, z_E)$ were known during the damaged point searching stage. It is necessary to find points $P, Q, M,$ and N to define the two approaching lines. Once such points were determined, the U-shaped boundary can be obtained. The coordinates of such points can be defined as follows: z_P and z_N were defined by finding the maximum z -coordinate on the damaged cross-section, which is z_T in Figure 5b. z_Q and z_M were defined by exploring the minimum z -coordinate on the damaged cross-section, which is z_G . Since the damaged model was sliced along the y -axis, $y_P = y_Q = y_M = y_N = y_S = y_E$. x_P and x_N were randomly defined as long as x_P is much less than the minimum x -coordinate of the damaged points and x_N is much larger than the maximum x -coordinate of the damaged points. Once x_P, x_N and the side wall inclination angle θ were defined, the coordinates x_Q and x_M can be calculated according to Equation (1):

$$\begin{cases} x_Q = \frac{z_P - z_Q}{\tan \theta} + x_P \\ x_M = x_N - \frac{z_N - z_M}{\tan \theta} \end{cases} \quad (1)$$

Once the two approaching lines were defined, relationship check between the approaching lines and the cross-section was conducted. If there is no intersection, a step

was applied to x_P and x_N to make the approaching lines closer to the cross-section, and another checking iteration was conducted. Two approaching lines that firstly have intersections with the damaged curve can be obtained and lines before this iteration were gathered, which is shown in Figure 5b. Finally, line PN and QM were added to close the U-shaped contour.

The inclination angle θ of the two approaching lines can be operator determined and adjusted flexibly according to the specifications and performance of the AM system. It should be noted that θ has a significant effect on the cut-off volume that should be machined in the pre-repair machining step. A small θ can give good accessibility to the AM system but may result in a much more cut-off volume. An optimized θ needs to be determined which not only reveals good accessibility but also holds a minimized cut-off volume. For this purpose, a series of approaching lines with varied inclination angle was adopted to intersect a cross-section shown in Figure 6a. Inclination angle θ controls the accessibility and it shouldn't approach 90° .

A series of experiments were conducted that aim to refill slots with different sidewall inclination angles (45° , 75° , 90°) on H13 tool steel in Paper I and it was found that 75° tilt angle can still yield a sound bi-material bonding and good material properties. Therefore, the range of angle θ was limited in $[10^\circ, 75^\circ]$. The area difference between the U-shaped profile and the cross-section, ΔS shown in Figure 6b, can indicate the cut-off area. A series of approaching lines were processed on cross-sections A and B as shown in Figures 6a and 6b and the relationship between ΔS and inclination angle θ was plotted in Figure 6c.

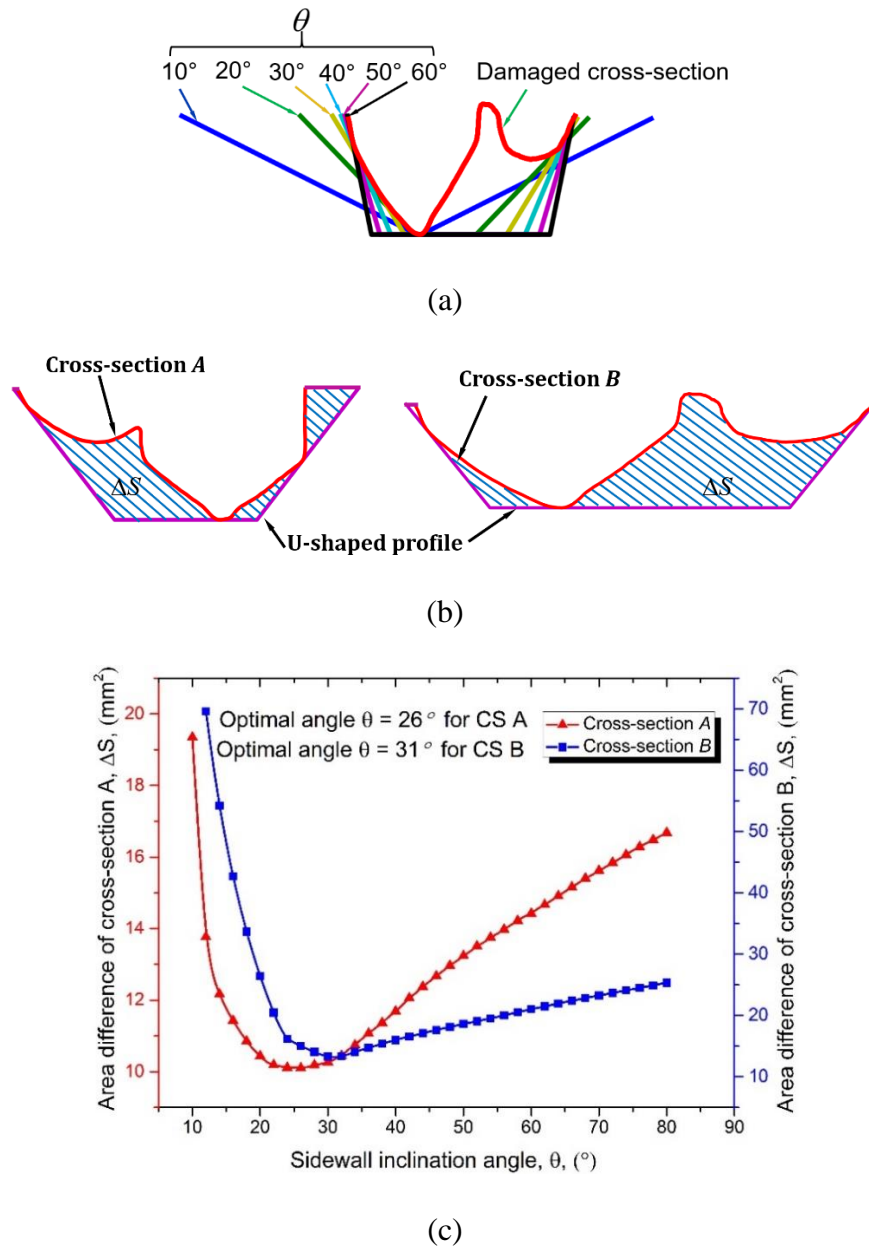


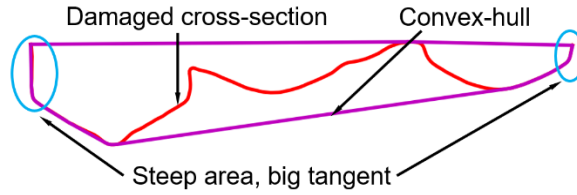
Figure 6. Sidewall inclination angle optimization for the U-shaped boundary. (a) U-shaped boundary with varied approaching lines; (b) U-shaped boundary for cross-sections A and B; (c) Relationship between area difference ΔS and sidewall inclination angle θ

It was observed from Figure 6c that for both cross-sections, the area ΔS decreases and then increases with the increase of angle θ . The curves indicate that neither a minimum

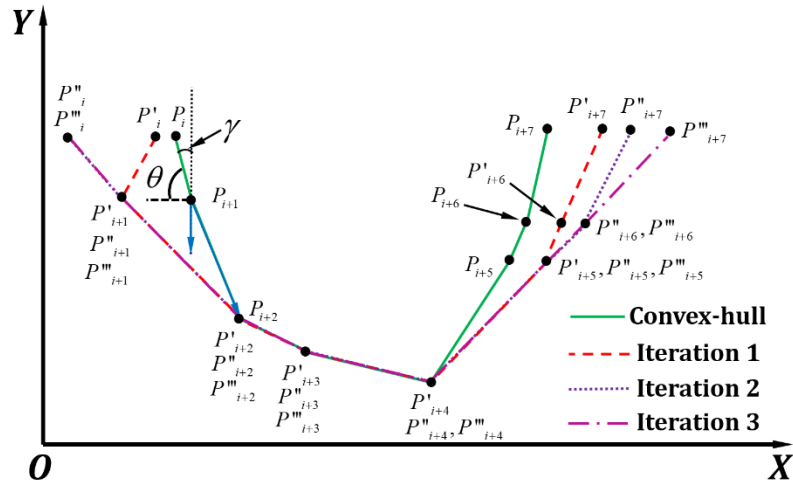
or a maximum tile angle can result in the minimum cut-off volume. It was found that the optimal angle θ for CS A is 26° and is 31° for CS B. Therefore, the optimal angle θ is highly dependent on the profile of the cross-section and should be determined for each cross-section. It can be found that for very deep but thin damage, the minimum cut-off volume is nearly at an angle of 90° . This is because the closer of the angle to 90° , the less the cut-off will be.

2.3.2. Convex-Hull Boundary Definition. One can see in Figure 5b that for U-shaped boundary, the bottom connecting line QM is parallel to the x-axis, and this may result in extra material cut-off in the polygon $GMETG$. This material over-cut comes worse when one deep defect is presented while majority defects are shallow because the depth of the bottom line QM is determined by finding the minimum z-coordinate across the damaged cross-sections. If a deep damage was presented, materials located between the bottom plane and the shallow defects also need to be machined. Because such material has to be deposited back through additive manufacturing process, this machining methodology will consume more time and efforts.

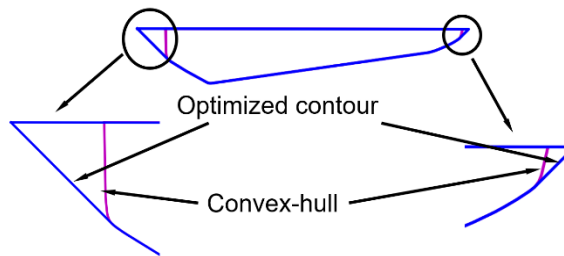
To further minimize cut-off volume, the convex-hull boundary was obtained as shown in Figure 7a. The convex-hull of any polygon can be easily obtained based on the existing algorithm [29]. However, one should notice that the convex-hull cannot be directly utilized as the boundary for pre-machining owing to the possibility of the steep area as shown in Figure 7a. The line segments in those regions have big tangents that cannot guarantee the accessibility to laser beam and powder feed nozzles. Therefore, such lines need to be tilted. The algorithm for tilting lines with big tangent is schematically depicted in Figure 7b and discussed below.



(a)



(b)



(c)

Figure 7. Convex-hull boundary definition. (a) Convex-hull processed on a cross-section; (b) Sidewall inclination angle optimization for convex-hull boundary; (c) Optimized contour

Suppose polygon $P_i P_{i+1} \dots P_{i+6} P_{i+7}$ is a convex-hull of one cross-section. The inclination angle of $P_i P_{i+1}$ is indicated as θ . Because θ is beyond the allowed accessible

angle, P_i needs to be rotated around P_{i+1} to P'_i . The coordinate of $P'_i(x'_i, y'_i, z'_i)$ can be calculated according to Equation. 2, where $(x_{i+1}, y_{i+1}, z_{i+1})$ is the coordinate of P_{i+1} and γ is the complementary angle of θ . The inclination angle of $P_{i+1}P_{i+2}$ also exceeds the allowed angle and therefore, P_{i+1} also needs to be rotated around P_{i+2} to P'_{i+1} . After that, the shifted polygon is $P'_iP'_{i+1} \cdots P'_{i+6}P'_{i+7}$. However, the inclination angle $P'_iP'_{i+1}$ still surpasses the desired angle and therefore, P'_i needs to be further rotated around P'_{i+1} to P''_i . After the second iteration, the shifted polygon became $P''_iP''_{i+1} \cdots P''_{i+6}P''_{i+7}$. There is another iteration to move P''_{i+7} to P'''_{i+7} . Finally, the contour $P'''_iP'''_{i+1} \cdots P'''_{i+6}P'''_{i+7}$ is obtained that satisfies the accessibility requirement, and therefore, can be used as a boundary for cut-off volume definition.

$$\begin{array}{ll}
 \text{when } y_{i+1} < y_i \text{ (Decreasing):} & \text{when } y_{i+1} > y_i \text{ (Increasing):} \\
 x'_i = x_{i+1} - \sqrt{\left(\frac{y_{i+1} - y_i}{\cos \gamma}\right)^2 - (y_{i+1} - y_i)^2} & \text{and } x_{i+1}' = x_i + \sqrt{\left(\frac{y_{i+1} - y_i}{\cos \gamma}\right)^2 - (y_{i+1} - y_i)^2} \\
 y'_i = y_i & y_{i+1}' = y_i \\
 z'_i = z_i & z_{i+1}' = z_i
 \end{array} \quad (2)$$

The aforementioned algorithm was applied to a cross-section as shown in Figure 7a and the optimized contour is depicted in Figure 7c. As illustrated in Figure 7c, the steep area in the original convex hull was successfully tilted.

2.4. MACHINING VOLUME ACQUISITION

U-shaped and convex-hull strategies were processed on the STL model with ball-indentations as shown in Figure 8a. For U-shaped strategy, sidewall with fixed inclination angle $\theta = 45^\circ$ and optimized angle were both conducted, and the target models were

shown in Figures 8b and 8c, respectively. The model processed using convex-hull strategy was presented in Figure 8d.

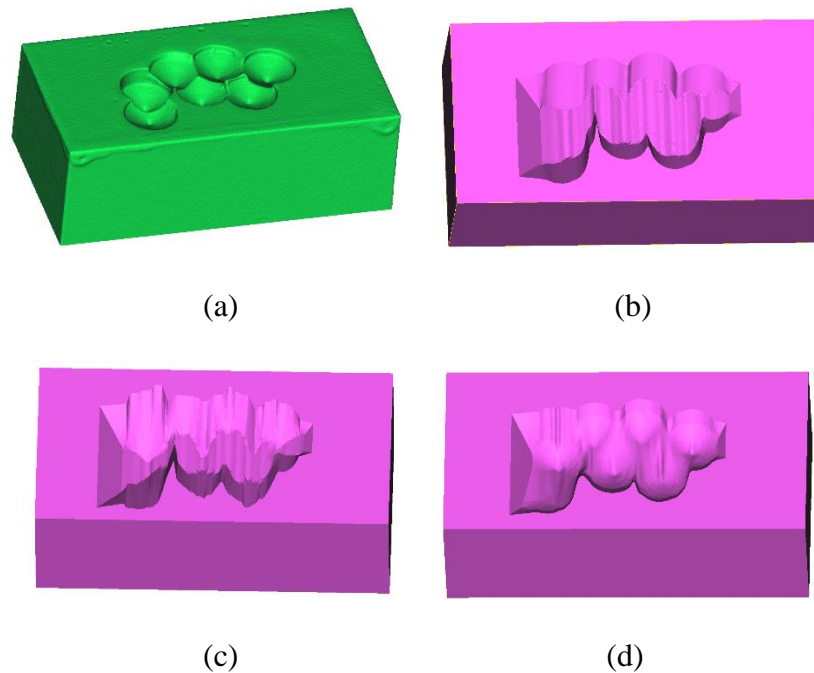


Figure 8. Unprocessed and processed models. (a) Model of the damaged substrate; Model pre-machined using U-shaped strategy (b), U-shaped strategy with an optimized sidewall inclination angle (c) and convex-hull strategy (d)

The volume of the unprocessed damaged model (Figure 8a) and volumes of processed models (Figures 8b-d) using proposed strategies were summarized in Table 1. The volumes of machined models are different based on the strategies for target geometry acquisition. It can be observed from Table 1 that the U-shaped strategy with optimized sidewall inclination angle will machine off less material compared with non-optimized U-shaped strategy. However, the convex-hull strategy results in the least amount of cut-off

volume, which is expected. Therefore, in the next machining step, convex-hull strategy-generated geometry was adopted as the guide model for machining toolpath and NC code generation.

Table 1. The volume of the model with varied pre-machining strategies

Model	Damaged	U-shape	U-shape, optimized	Convex-Hull
Volume (mm ³)	22245.1	21216.3	21251.6	21331.8
Cut-off volume (mm ³)	-	1028.8	993.5	913.3

2.5. PRE-REPAIR MACHINING PROGRAM GENERATION

Once the target geometry was obtained, it was loaded to CAM software to generate the machining toolpath as shown in Figure 9. NC code was generated to drive the CNC mill. The milling parameters are listed in Table 2. The damaged substrate was clamped on a fixture and machined on a Fryer MC-30 CNC machine with the setup shown in Figure 9b. The machined part is shown in Figure 9c.

Table 2. Pre-repair machining parameters for surface impact damage

Tool	Feed rate	Spindle speed	Stepdown	Stepover	Toolpath
0.25'' Ball-end	508 mm/min	2000 r/min	0.5 mm	33%	Spiral

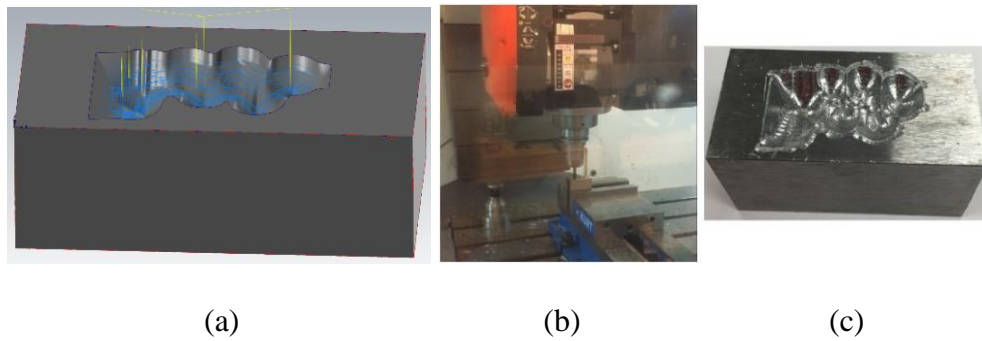


Figure 9. (a) Machining toolpath; (b) Machining setup; (c) Machined substrate

3. PRE-REPAIR MACHINING STRATEGY FOR SURFACE EROSION, WEAR, CORROSION, AND HEAT CHECKS

Casting dies are subjected to rapid heating and cooling cycles during their service that causes dimensional distortion and cracking. In addition, contacting with casting alloys such as liquid aluminum alloys causes surface defects such as erosion, wear, and corrosion. It is reported that thermal fatigue and erosion are major contributions to the failure of casting dies [30]. Die defects destruct the quality of copies, therefore needs frequent repair.

Directly depositing materials on damaged die surfaces is not suggested because of the following reasons. Firstly, the damaged surface usually contains impurities such as oxidized and contaminated materials. Surface pitting may also cause numerous tiny localized defects. Coating materials on such untreated surfaces cannot guarantee the solid bi-material bonding which may cause unpredictably delamination during application. Secondly, the AM process requires a certain surface roughness for material deposition (shiny surface requires high laser power and rough surface requires lower laser power). Damaged surfaces may not have a constant, defined roughness, whereas a machined

surface can provide this. Fortunately, such surface defects are usually superficial and can be easily removed by cutting off a thin layer of material from the target surface. The thickness of machined material can be determined as long as the machined surface is defect-free. Once such layer is machined, the material can be coated on such region to reobtain the designed dimensions.

The current research proposes a general procedure for treating surfaces with erosion, wear, heat checks, and corrosion. In general, the damaged component is 3D scanned to recreate its STL model. After that, the model is loaded to CAM software, and the target regions are selected. Machining parameters including cut-off thickness are determined and the machining program is generated. Subsequently, the program is transferred to CNC for pre-machining. The following sections detailed the pre-repair machining procedure for such damage.

3.1. MODEL RECONSTRUCTION OF A DIE

A die shown in Figure 10a has damage on the convex area. Such defects are common in dies due to corrosion and heating-cooling cycles in the casting process. To machine off a thin layer of material from the part, the model of the die was generated using the configuration in Figure 3 and the recreated model is shown in Figure 10b. It should be pointed out that creating the model of the whole part is not necessary for pre-repair machining. This is because only the surface with defects needs to be targeted and other regions are not necessarily required. Generating the whole model not only dramatically slow down the 3D scanning process, but also sophisticate the toolpath generation process due to the large size of the model. Therefore, only the area requires machining was scanned.

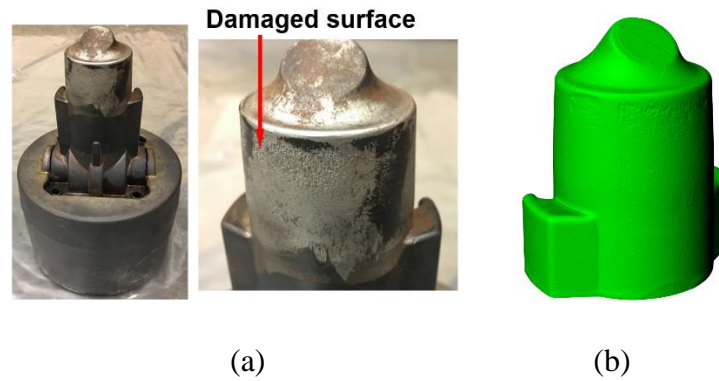


Figure 10. (a) A casting die with surface erosion, wear, and corrosion; (b) STL model of the damaged region of the casting die

3.2. MACHINING VOLUME DETERMINATION AND MACHINING

The cut depth for machining can be determined based on the condition of damaged components. For the part in Figure 10, materials with 0.5 mm layer thickness were machined. The toolpath was generated as shown in Figure 11a and the simulated machined part is shown in Figure 11b.

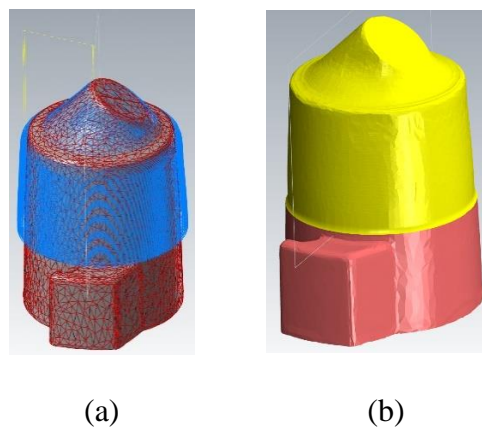


Figure 11. (a) Machining tool path generation; (b) Machined model

4. PRE-REPAIR MACHINING STRATEGY FOR CRACKING


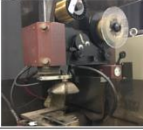

The heating and cooling cycles during metal casting cause cyclic compressive and tensile stress conditions which led to thermal fatigue to the casting die [31]. That is why H13 hot work tool steel is usually adopted as die material owing to its high hardenability and good thermal fatigue resistance. Thermal fatigue cracking is a common failure in die-casting dies and engine blades after thousands of shots. The cracking is first to like to appear at corners and edges with small radius [32].

Detailed machining procedure for cracking highly depends on the appearance of cracks and can be determined only after considering a number of factors, such as the depth and length of cracks, surrounding structures, accessibility of cracks to machining tool and AM system, surface or internal cracking, etc. Therefore, this paper presents some candidate machining approaches that can be considered for cracking removal.

Table 3 lists a few machining methods for cracking. Cracks are classified into shallow and deep cracks because they may need different machining methods. For example, for shallow cracks, they can be easily and effectively removed by surface grinding. Therefore, 3D scanned models of such parts are not needed. For deep cracks, electrical discharge machining (EDM) and computerized numerical control (CNC) machining can be utilized. EDM can cut off materials with cracks much more efficiently, but it is only applicable to cracks that can be accessible to EDM wire. If the cracking is surrounded by other structures, EDM is not applicable and therefore, CNC machining can be considered. Such machining procedures will consume more material over surface grinding. One should know that internal cracking is not easy to observe visually and then

may require nondestructive testing. Material defects such as intergranular cracking are not visually observable and require examination using optical microscope or scanning electron microscope. The observation needs to provide the position and shape of the internal defects. Once the internal cracking is located, a slot can be made to remove the cracks. However, machining a slot is not always working because a very deep slot is difficult to refill, especially when the edge of the slot is near vertical. In such cases, the U-shaped strategy can be applied or the portion of the component with cracks can be completely cut-off and rebuild. This approach is applicable to any cracks regardless of depth, but it will cut-off a huge amount of material. Therefore, one needs to evaluate the cost by repairing them over replacement with a new copy. In this paper, a titanium engine blade with cracks was machined using EDM to show the machining procedure.

Table 3. Candidate machining approaches for cracking

Cracking depth	Machining method	Machining overview	Cut-off material	Remarks
Shallow	Grinding	Cracking removal by grinding 	Small	Applicable to surface cracking. Convex grinding wheel for good accessibility
Deep	EDM (Electro-discharge machining)	Cracking removal using EDM 	Moderate	Applicable to cracks that are accessible to EDM wire
	CNC machining	Cracking removal using CNC 		Applicable to cracks that are accessible to cutting tools
	Cracking piece replacement	Cut off the portion that has cracks. Rebuild the cut-off part for replacement	Large	Applicable to all cracks regardless of depth

4.1. MACHINING STRATEGY FOR CRACKING ON BLADES

An engine blade was utilized to demonstrate the pre-repair machining strategy for cracking. Trailing edge cracking is a common failure in turbine or compressor blade mainly due to excessive stress, overloading, overheating, defective materials and impact with foreign objects. Several studies have been targeting on blade repair, mainly focusing on damage extraction [18], [33], and [34], material deposition process [35-37] and repair automation [38, 39], while no reporting on strategies of pre-machining. It is required to cut off the material surrounding cracks because non-machined cracks give no accessibility to the AM system, as shown in Figure 12a. This is why the defects in blade edge reported in [19], [38] and [40] have U or V-shaped geometries when conducting repair.

To perform pre-machining, the blade as shown in Figure 12a was digitally scanned to acquire its 3D model as shown in Figure 12b. After that, the defective area was selected as shown in Figure 12c. By selecting the damaged area, the points located at the worn domain can be easily extracted which is shown in Figure 13a, and subsequently, the convex-hull of the point set was obtained. However, the convex-hull cannot be directly used for pre-machining because the bottom portion of the convex-hull blocks the accessibility. In order to create an open V-shaped geometry, the line segments of the convex-hull were tilted according to the algorithm illustrated in 2.3.2. The maximum sidewall inclination angle θ is limited at 60° . The finally optimized contour was shown in Figure 13b. EDM wire then followed the optimized contour for machining and the pre-machined blade is shown in Figure 13c. This machining approach provides a feasible shape for material deposition as the original cracking was removed and the repair volume is clear and accessible to additive equipment.

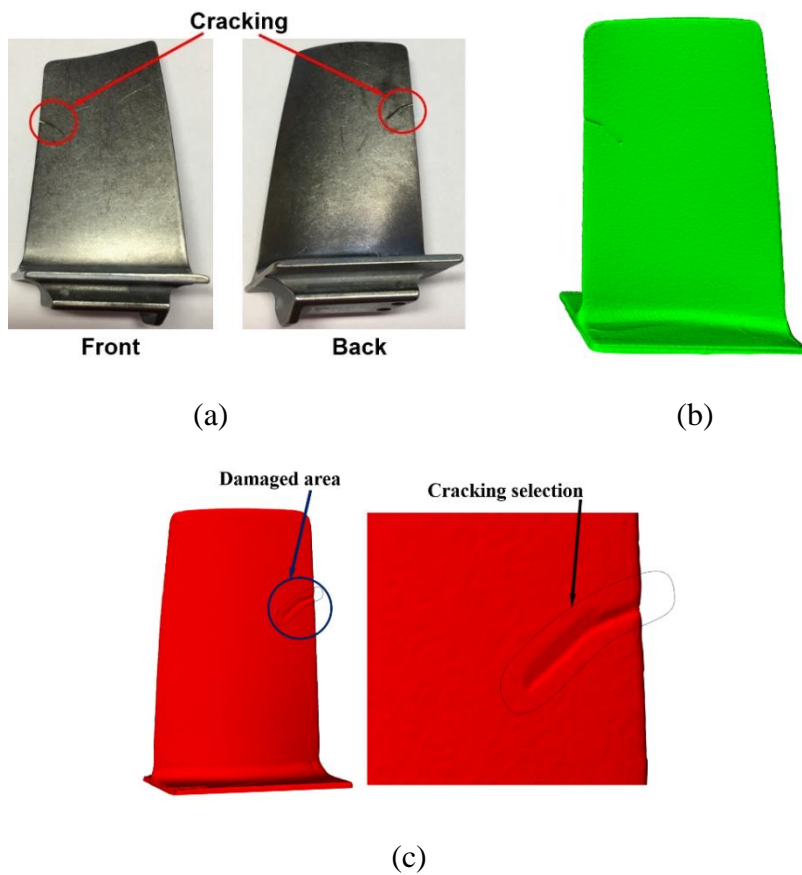


Figure 12. (a) Titanium blade with cracks; (b) Reconstructed model of the blade; (c) Selection of points located at the damaged area

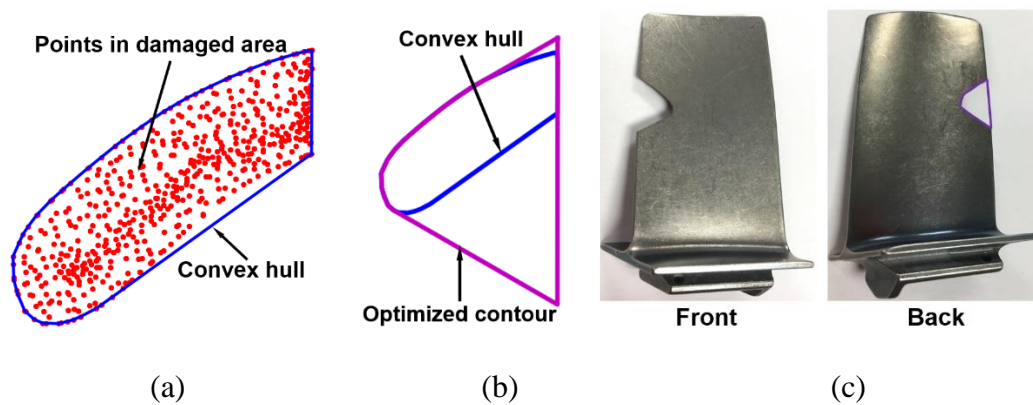


Figure 13. (a) Damaged point set extraction and its convex-hull; (b) Optimized contour; (c) Blade after pre-machining

5. PRE-REPAIR HETA-TREATMENT OF DAMAGED DIE

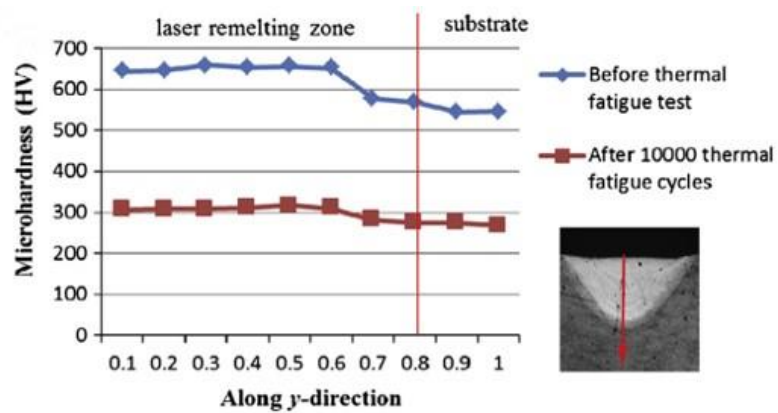
Many parts such as H13 tool steel dies/molds undergo heating and cooling cycles in service and will finally result in thermal fatigue failure. It is reported in [41] that with increasing numbers of thermal cycles, the hardness and microstructure of H13 tool steel can change, which eventually results in loss of mechanical strength and plastic deformation. As shown in Figure 14, the hardness of H13 tool steel after 10000 thermal fatigue cycles decreased from 650 HV to 300 HV. The microstructure became coarser and lots of carbides with V and Cr appeared. Without re-hardening the material, its nominal mechanical properties cannot be restored even the geometry is repaired. Therefore, the re-hardening process should be conducted on the worn material before laser metal deposition.

Figure 15 depicted the re-hardening procedure for H13 tool steel. It should be noted that H13 tool steel for die/mold applications is already in quenched and tempered condition. In order to re-harden it, annealing must be conducted at first.

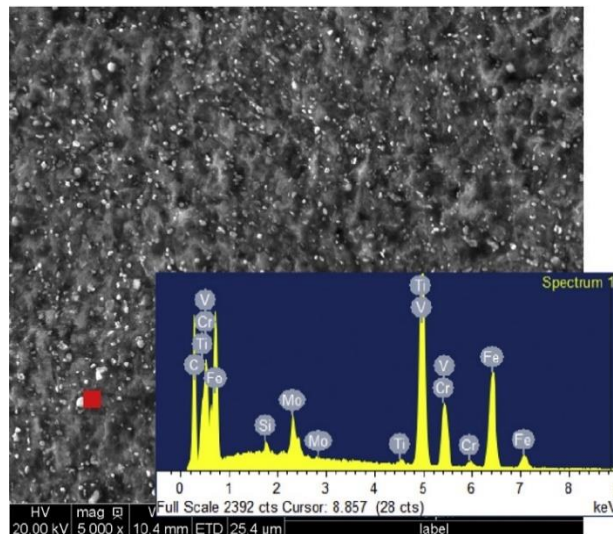
Figure 16 shows the tensile testing data of worn H13 tool steel (BH), re-hardened H13 tool steel (AH) and new quenched and tempered H13 tool steel (N). It can be observed that the UTS of worn H13 tool steel before re-hardening is 1427.9 MPa. By re-hardening it, the UTS can be increased to 1846.7 MPa and the ductility is also increased a lot. The tensile properties of re-hardened H13 tool steel are comparable with that of the new H13 steel in quenched and tempered condition. Therefore, it can be concluded that re-hardening can restore the tensile strength of worn H13 tool steel.

Figure 17 shows the hardness measurements of worn H13 tool steel (BH), re-hardened H13 tool steel (AH) and new quenched and tempered H13 tool steel (N). In terms

of hardness, the worn H13 tool steel has a hardness of around 420 - 440 HV while the re-hardened H13 steel is about 540 - 550 HV which is similar to the hardness of new quenched and tempered H13 tool steel. Therefore, by re-hardening the worn H13 tool steel, its hardness can be increased.



(a)



(b)

Figure 14. (a) The hardness of H13 tool steel before and after thermal fatigue cycles [41];
(b) Microstructure of H13 tool steel after thermal fatigue cycles [41]

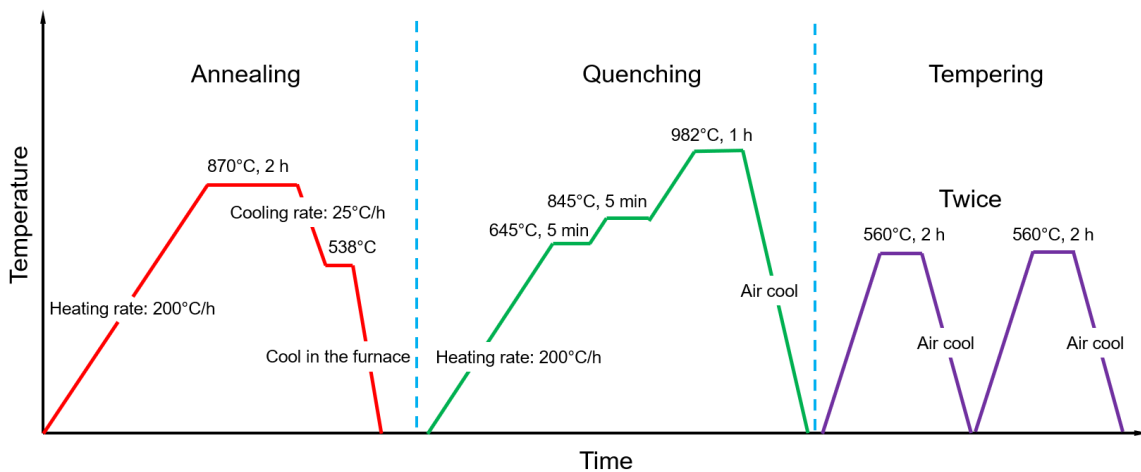


Figure 15. Schematic diagram of the re-hardening process for H13 tool steel

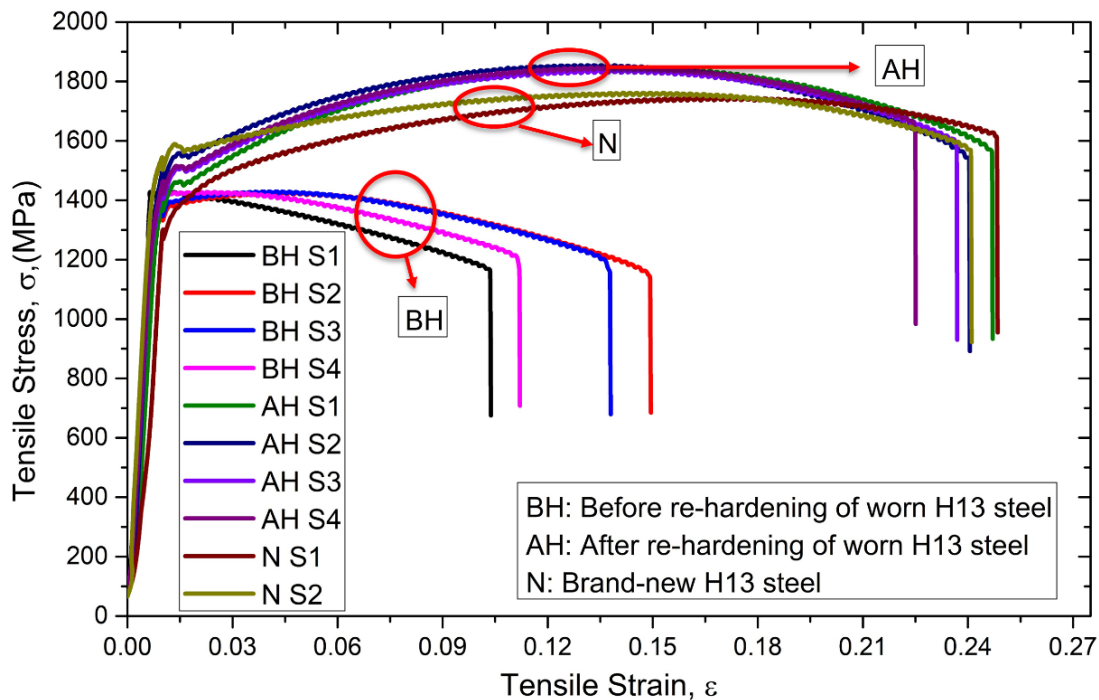


Figure 16. Tensile testing data of worn H13 tool steel (BH), re-hardened H13 tool steel (AH) and brand-new H13 tool steel in quenched and tempered condition

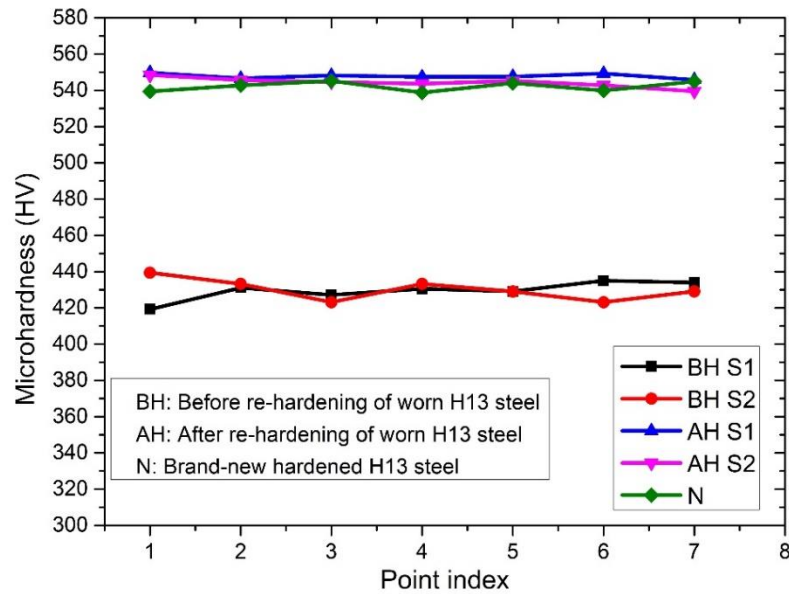


Figure 17. The hardness of worn H13 tool steel (BH), re-hardened H13 tool steel (AH) and brand-new H13 tool steel in quenched and tempered condition

6. CONCLUSION

Pre-repair processing of damaged components is crucial before additive manufacturing to make sure the damage is accessible, the part is free of contamination, and the mechanical properties are restored. For this purpose, this paper presents pre-repair machining strategies targeting surface defects and cracking, and pre-repair heat-treatment procedure for H13 tool steel. Damaged part was first inspected and machining tool was determined. Reconstructed model of the damage component is usually required for pre-repair machining toolpath generation. For surface impact defects, two strategies, U-shaped, and convex-hull strategies were introduced for cut-off volume definition. The convex-hull method results in less material removal and is, therefore, preferred. For surface erosion, wear, and corrosion, a thin layer of material at the damaged region was removed to get rid

of contaminated layers or numerous tiny defects. Approach for removing cracking should be determined after considering several factors such as the depth and length of cracks, surrounding structures, accessibility of cracks, surface or internal cracking, etc. This study presents an approach for removing cracks in blade edge using EDM. At last, the mechanical properties of damaged H13 tool steel was successfully restored through the re-hardening procedure.

ACKNOWLEDGMENTS

This project was supported by TOYOTA/Bodine Aluminum, NSF Grants CMMI-1547042, and CMMI-1625736, and the Intelligent System Center, Center for Aerospace Manufacturing Technology, and Material Research Center at Missouri S&T. Their financial support is greatly appreciated.

REFERENCES

- [1] R. Raju, M. Duraiselvam, V. Petley, S. Verma, and R. Rajendran, "Microstructural and Mechanical Characterization of Ti6Al4V Refurbished Parts obtained by Laser Metal Deposition," *Materials Science and Engineering: A*, vol. 643, pp.64-71, 2015.
- [2] K. Zhang, S. Wang, W. Liu, and X. Shang, "Characterization of Stainless Steel Parts by Laser Metal Deposition Shaping," *Materials & Design*, vol. 55, pp. 104-119, 2014.
- [3] E. Brandl, B. Baufeld, C. Leyens, and R. Gault, "Additive Manufactured Ti-6Al-4V using Welding Wire: Comparison of Laser and Arc Beam Deposition and Evaluation with Respect to Aerospace Material Specifications," *Physics Procedia*, vol. 5, pp. 595–606, 2010.

- [4] W. Li, X. Chen, L. Yan, J. Zhang, X. Zhang, and F. Liou, "Additive Manufacturing of a New Fe-Cr-Ni Alloy with Gradually Changing Compositions with Elemental Powder Mixes and Thermodynamic Calculation," *International Journal of Advanced Manufacturing Technology*, vol. 95, pp. 1013-1023, 2018.
- [5] W. Li, L. Yan, X. Chen, J. Zhang, X. Zhang, and F. Liou, "Directed Energy Depositing a New Fe-Cr-Ni Alloy With Gradually Changing Composition With Elemental Powder Mixes and Particle Size' Effect in Fabrication Process," *Journal of Materials Processing Technology*, vol. 255, pp. 96-104, 2018.
- [6] W. Cui, X. Zhang, and F. Liou, "Additive Manufacturing of High-Entropy Alloy - A Review," *Solid Freeform Fabrication Symposium Conference, Texas*, pp. 712-724, 2017.
- [7] R. M. Mahamood and E. T. Akinlabi, "Laser Metal Deposition of Functionally Graded Ti6Al4V/TiC," *Materials & Design*, vol. 84, pp. 402-410, 2015.
- [8] G. P. Dinda, A. K. Dasgupta, and J. Mazumder, "Laser Aided Direct Metal Deposition of Inconel 625 Superalloy: Microstructural Evolution and Thermal Stability," *Materials Science and Engineering: A*, vol. 509, pp. 98-104, 2009.
- [9] X. Zhang, W. Li, X. Chen, W. Cui, and F. Liou, "Evaluation of Component Repair using Direct Metal Deposition from Scanned Data," *International Journal of Advanced Manufacturing Technology*, vol. 95, pp. 3335-3348, 2018.
- [10] X. Zhang, W. Li, K. M. Adkison, and F. Liou, "Damage Reconstruction from Tri-Dexel Data for Laser-Aided Repairing of Metallic Components," *International Journal of Advanced Manufacturing Technology*, vol. 96, pp. 337-3390, 2018.
- [11] J. Gao, X. Chen, O. Yilmaz, and N. Gindy, "An Integrated Adaptive Repair Solution for Complex Aerospace Components through Geometry Reconstruction," *International Journal of Advanced Manufacturing Technology*, vol. 36, pp. 1170-1179, 2008.
- [12] H. Qi, M. Azer, and P. Singh, "Adaptive Toolpath Deposition Method for Laser Net Shape Manufacturing and Repair of Turbine Compressor Airfoils," *International Journal of Advanced Manufacturing Technology*, vol. 48, pp. 121-131, 2010.
- [13] X. Penaranda, S. Moralejo, A. Lamikiz, and J. Figueras, "An Adaptive Laser Cladding Methodology for Blade Tip Repair," *International Journal of Advanced Manufacturing Technology*, vol. 92, pp. 4337-4343, 2017.
- [14] J. Bennett, R. Dudas, J. Cao, K. Ehmann, and G. Hyatt, "Control of Heating and Cooling for Direct Laser Deposition Repair of Cast Iron Components," *2016 International Symposium on Flexible Automation (ISFA)*, pp. 229-236, 2016.

- [15] W. Li, J. Zhang, X. Zhang, and F. Liou, "Effect of Optimizing Particle Size on Directed Energy Deposition of Functionally Graded Material with Blown Pre-mixed Multi-powder," *Manufacturing Letters*, vol. 13, pp. 39-43, 2017.
- [16] W. Li, X. Zhang, and F. Liou, "Modeling Analysis of Argon Gas Flow Rate's Effect on Pre-Mixed Powder Separation in Laser Metal Deposition Process and Experimental Validation," *International Journal of Advanced Manufacturing Technology*, vol. 96, pp. 4321-4331, 2018.
- [17] W. Wang, A. J. Pinkerton, L. M. Wee, and L. Li, "Component Repair Using Laser Direct Metal Deposition," *Proceedings of the 35th International MATADOR Conference*, pp. 345-350, 2007.
- [18] X. Zhang, W. Li, and F. Liou, "Damage Detection and Reconstruction Algorithm in Repairing Compressor Bode by Direct Metal Deposition," *International Journal of Advanced Manufacturing Technology*, vol. 95, pp. 2393-2404, 2018.
- [19] X. Zhang, W. Li, W. Cui, and F. Liou, "Modeling of Worn Surface Geometry for Engine Blade Repair using Laser-Aided Direct Metal Deposition Process," *Manufacturing Letters*, vol. 15, pp. 1-4, 2018.
- [20] T. Petrat, B. Graf, A. Gumenyuk, and M. Rethmeier, "Laser Metal Deposition as Repair Technology for a Gas Turbine Burner Made of Inconel 718," *Physics Procedia*, vol. 83, pp. 761-768, 2016.
- [21] P. Kattire, S. Paul, R. Singh, and W. Yan, "Experimental Characterization of Laser Cladding of CPM 9V on H13 Tool Steel for Die Repair Applications," *Journal of Manufacturing Processes*, vol. 20, pp. 492-499, 2015.
- [22] J. M. Wilson, C. Piya, Y. C. Shin, F. Zhao, and K. Ramani, "Remanufacturing of Turbine Blades by Laser Direct Deposition with its Energy and Environmental Impact Analysis," *Journal of Cleaner Production*, vol. 80, pp. 170-178, 2014.
- [23] K. Eiamsa-ard, H. J. Nair, L. Ren, J. Ruan, T. Sparks, and F. W. Liou, "Part Repair using a Hybrid Manufacturing System," *Solid Freeform Fabrication Symposium Conference, Texas*, pp. 425-433, 2005.
- [24] C. Bremer, "Automated Repair and Overhaul of Aero-Engine and Industrial Gas Turbine Components," *ASME Proceedings-Manufacturing Materials and Metallurgy*, vol. 2, pp. 841-846, 2005.
- [25] J. Gao, X. Chen, O. Yilmaz, and N. Gindy, "An Integrated Adaptive Repair Solution for Complex Aerospace Components through Geometry Reconstruction," *International Journal of Advanced Manufacturing Technology*, vol. 36, pp. 1170-1179, 2008.

- [26] O. Yilmaz, N. Gindy, and J. Gao, "A Repair and Overhaul Methodology for Aeroengine Components," *Robotics and Computer-Integrated Manufacturing*, vol. 26, pp. 190-201, 2010.
- [27] X. Zhang, W. Li, K. M. Adkison, and F. Liou, "Damage Reconstruction from Tri-Dexel Data for Laser-Aided Repairing of Metallic Components," *International Journal of Advanced Manufacturing Technology*, vol. 96, pp. 3377-3390, 2018.
- [28] J. M. Wilson, C. Piya, Y. C. Shin, F. Zhao, and K. Ramani, "Remanufacturing of Turbine Blades by Laser Direct Deposition with its Energy and Environmental Impact Analysis," *Journal of Cleaner Production*, vol. 80, pp. 170-178, 2014.
- [29] J. Sklansky, "Finding the Convex Hull of a Simple Polygon," *Pattern Recognition Letters*, vol. 1, pp. 79-83, 1982.
- [30] S.-H. Chang, T.-P. Tang, Y.-C. Chen, and J.-K. Chen, "Enhancement of Erosion Resistance on AISI H13 Tool Steel by Oxynitriding Treatment," *ISIJ International*, vol. 49, pp. 421-424, 2009.
- [31] A. Persson, S. Hogmark, and J. Bergström, "Failure Modes in Field-Tested Brass Die Casting Dies," *Journal of Materials Processing Technology*, vol. 148, pp. 108-118, 2004.
- [32] Z. X. Jia, J. Q. Li, L. J. Liu, and H. Zhou, "Performance Enhancements of High-Pressure Die-Casting Die Processed by Biomimetic Laser-Remelting Process," *International Journal of Advanced Manufacturing Technology*, vol. 58, pp. 421-429, 2012.
- [33] Y. Rong, J. Xu, and Y. Sun, "A Surface Reconstruction Strategy based on Deformable Template for Repairing Damaged Turbine Blades," *Proceedings of the Institution of Mechanical Engineers, Part G: Journal of Aerospace Engineering*, vol. 228, pp. 2358-2370, 2014.
- [34] J. Gao, X. Chen, D. Zheng, O. Yilmaz, and N. Gindy, "Adaptive Restoration of Complex Geometry Parts through Reverse Engineering Application," *Advances in Engineering Software*, vol. 37, pp. 592-600, 2006.
- [35] G. Bi and A. Gasser, "Restoration of Nickel-Base Turbine Blade Knife-Edges with Controlled Laser Aided Additive Manufacturing," *Physics Procedia*, vol. 12, pp. 402-409, 2011.
- [36] S. Nowotny, S. Scharek, E. Beyer, and K.-H. Richter, "Laser Beam Build-Up Welding: Precision in Repair, Surface Cladding, and Direct 3D Metal Deposition," *Journal of Thermal Spary Technology*, vol. 16, pp. 344-348, 2007.

- [37] M. Gäumann, C. Bezençon, P. Canalis, and W. Kurz, "Single-Crystal Laser Deposition of Superalloys: Processing-Microstructure maps," *Acta Materialia*, vol. 49, pp. 1051-1062, 2001.
- [38] J. Gao, X. Chen, O. Yilmaz, and N. Gindy, "An Integrated Adaptive Repair Solution for Complex Aerospace Components through Geometry Reconstruction," *International Journal of Advanced Manufacturing Technology*, vol. 36, pp. 1170-1179, 2008.
- [39] J. Gao, J. Folkes, O. Yilmaz, and N. Gindy, "Investigation of a 3D Non-Contact Measurement based Blade Repair Integration System," *Aircraft Engineering and Aerospace Technology*, vol. 77, pp. 34-41, 2005.
- [40] C. Piya, J. M. Wilson, S. Murugappan, Y. Shin, and K. Ramani, "Virtual Repair: Geometric Reconstruction for Remanufacturing Gas Turbine Blades," *16th Design for Manufacturing and the Life Cycle Conference*, Washington, DC, USA, vol. 9, pp. 895-904, 2011.
- [41] Z. Jia, Y. Liu, J. Li, L. Liu, and H. Li, "Crack Growth Behavior at Thermal Fatigue of H13 Tool Steel Processed by Laser Surface Melting", *International Journal of Fatigue*, vol. 78, pp. 61-71, 2015.

III. DAMAGE DETECTION AND RECONSTRUCTION ALGORITHM IN REPAIRING COMPRESSOR BLADE BY DIRECT METAL DEPOSITION

Xinchang Zhang¹, Wei Li¹, and Frank Liou¹

¹Department of Mechanical and Aerospace Engineering,

Missouri University of Science and Technology, Rolla, MO 65409, USA

ABSTRACT

Aero-engine blade repair is challenging due to its complicated geometry and unique defects after serving in a harsh environment. Traditional manual-based remanufacturing processes are not capable of yielding consistently repaired part quality, significantly limiting the application of repair technologies. For building up materials on damaged blades, it is required to detect and extract the repair volume and generate a corresponding tool path for additive manufacturing. Therefore, the objective of this paper is to propose an automated damage detection and reconstruction algorithm for jet engine blade repair. Reverse Engineering was utilized to reconstruct models of nominal and damaged blades. The reconstructed damaged model was best-fitted with the nominal model by a transformation matrix and using overlapping area comparison method. Through the area comparison method, the damaged blade was separated into the intact section and damaged section. A set of parallel and equidistant casting rays were used to intersect with damaged layers to extract the repair volume. Laser scanning tracks were generated according to the extracted geometry. The laser-assisted direct metal deposition process was performed to deposit Ti-6Al-4V particles on the damaged region. Finally, microstructure analysis was

carried out to evaluate the repaired part quality. The repair experiment validated that the proposed algorithm is suitable and efficient for automated repair of curved blades.

Keywords: Damage Detection and Reconstruction; Component Repair; Direct Metal Deposition; Compressor Blade

1. INTRODUCTION

Turbine and compressor blades are crucial components in modern aircraft engines to produce powerful thrust by rotating at a very high speed. The presence of unavoidable harsh working environments such as elevated temperature and pressure, impact with foreign objects, wear, corrosion and fatigue may damage blades prematurely [1]. Failures of blades including causes and appearance are systematically illustrated in [2], where the failure modes were classified, according to failure mechanisms, into low cycle fatigue, high cycle fatigue, thermal fatigue, environmental attack, creep damage, erosion, wear, overload damage and thermal aging. Because of the extremely hard-working conditions, modern aero-engine blades are made of titanium or nickel-based alloys in order to survive for a longer time [3, 4]. However, such alloys are expensive, and they require special tools for machining, which in combination increase the cost of such parts. Therefore, to improve the life cycle of blades is of immense importance.

It is illustrated that the cross-section profiles of blades are crucial as even a small change of dimensions may damage the aerodynamic performance of the blade and reduce the efficiency and reliability of engines [5]. Many studies have been focusing on strategies

to reinforce blades to achieve maximum durability by more proper design [6], using advanced materials [7], and coating thermal barrier coatings (TBCs) on blade surfaces [8].

Besides, considerable researchers are focusing on the repair of damaged blades to restore them to a desirable working condition. Generally, the repair process involves pre-inspection, damage reconstruction, build-up process, post-machining and post-inspection [5]. For the build-up process, laser direct metal deposition (DMD) [9, 10] is a good candidate because of many advantages, such as less heat input [11-13], compatible with many advanced materials [14], generate fully dense deposits [15], process flexibility [16, 17], and good for automation [18, 19].

DMD is an additive manufacturing (AM) process to build complex component layer by layer following user-defined tool path [20-22]. Therefore, reconstructing defects of damaged blades is crucial to provide a deposition tool path. However, it is very challenging due to the complex and unique defective geometric shape of blades. Defining the defective region manually is not reliable, time-consuming and error-prone.

To automatically restore defects, an approach was proposed by Jones, et al. [23] to integrate laser cladding, machining and in-process scanning in one machine. However, there is no discussion about how to compare the scanned model with the CAD model. Also, using a probe is not efficient for curved blades. To accelerate the process, a laser scanning system was used to capture surface points of a broken blade [24]. In order to extract the broken domain, the distance from each of the scanned point to the nominal surface was calculated. Based on the distance values, the point cloud on the damaged area was defined. However, the calculating process is very time-consuming. Defect detection using Iterative Closest Point (ICP) algorithm was proposed in [25] where the initially scanned data was

registered on the CAD model. The method concentrated on point cloud matching while defect extraction was not discussed. He and Li [26] developed a curved surface extension approach to reconstruct the missing volume based on continuous curvature. This method, however, has limitations for constructing complex curved blade due to part to part defects variation. In [27], a defect-free polygonal model was obtained by a surface extension method and can be used as a nominal geometry to extract the worn area's geometry. The reconstruction method in [5] resolves this issue by sweeping a surface across the defective region. The sweep is based on the cross-section lying immediately outside. Both studies were limited to the blade tip repair.

Reconstructing repair volume of damaged blades is the key to guarantee a successful repair. Therefore, the objective of this research is to explore an algorithm to regain the missing volume of a damaged blade. For this purpose, a nominal blade was scanned using a 3D scanner. Then defects were created on the blade edge to simulate the impact failure with foreign objects. The damaged blade was scanned to generate the damaged model. After that, the damaged model was best-fitted with the nominal model through proposed model alignment algorithm. Area comparison method was adopted to separate the damaged blade into the intact section and damaged section. Afterward, ray casting method was used to intersect damaged layers to extract the missing volume. Finally, the tool path was generated based on the repair volume, and then repair experiment was carried out. Titanium alloy powder was used as feedstock and deposited on the damaged zone by direct metal deposition process. The quality of the repaired part was analyzed through microstructure characterization to validate the repair through the proposed damage detection and reconstruction algorithm.

2. GENERAL STRUCTURE OF DAMAGE DETECTION AND RECONSTRUCTION ALGORITHM

Figure 1b shows a comparison of two cross-sections obtained by two parallel planes intersecting with the curved blade in Figure 1a. Because of a curved profile, the cross-sections at different levels are different and therefore, the model cannot be simply defined by one cross-section. Because of the complex shape of engine blades, an algorithm to automatically restore the damaged geometry is critical to provide accurate repair volume for repair.

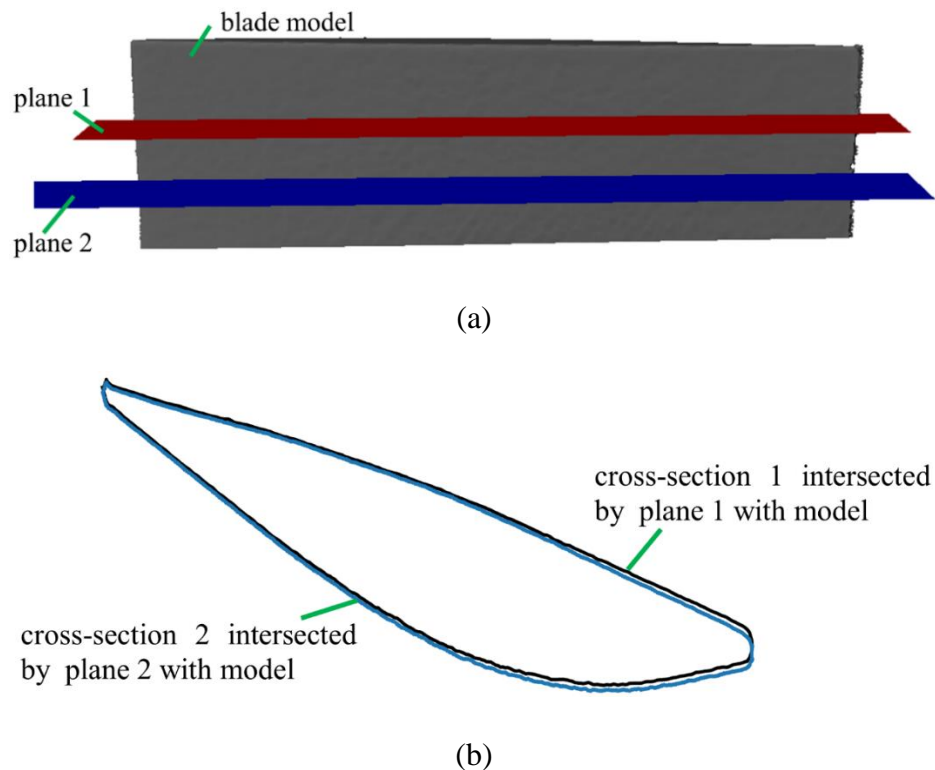


Figure 1. Cross-section comparison showing the curved profile of a blade. (a) The intersection of plane 1 and plane 2 with the blade; (b) Comparison of cross-section 1 with cross-section 2

Figure 2 shows the general structure of damage detection and reconstruction algorithms proposed in this paper. The method includes four sections: (1) Model acquisition, (2) Model best-fit, (3) Damage detection, and (4) Damage reconstruction. The general procedure is illustrated in this section and detailed information is presented in the following sections.

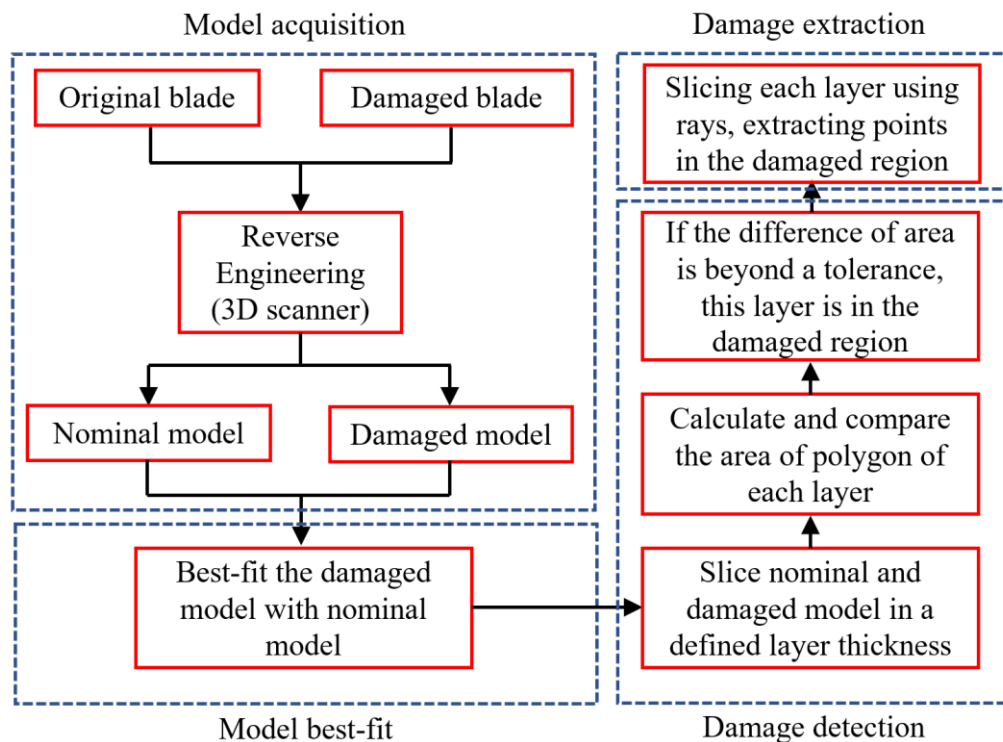


Figure 2. General structure of damage detection and reconstruction algorithms

In order to obtain the damaged region, reconstructing the 3D model of the damaged blade is the first step. Reverse Engineering is usually adopted to recreate models of physical

objects. In this study, both the nominal and damaged models were recreated using a highly accurate structured-light 3D scanner and both models were output in STL format.

Once the nominal and damaged models were obtained, the damaged model was usually in arbitrary position and orientation with the nominal model. Therefore, it is required to best-fit the damaged model with the nominal one. After that, both models were sliced into a number of layers creating a polygon on each layer. The area of each polygon from the damaged model and nominal models was calculated and compared. If the area difference was beyond tolerance, then it can be defined that this layer was damaged. After all damaged layers were defined, a series of lines were used to slice each damaged layer and the intersections of each line with the polygon were obtained. The intersection points in the damaged region were extracted as the missing volume's surface points, which created the geometry of the defective area.

2.1. MODEL ACQUISITION

The nominal compressor blade is shown in Figure 3a. Because the dimensions of the blade are larger than the working space of the DMD machine used in this research, the blade was sectioned to a small piece as shown in Figure 3b using EDM. The nominal blade was fixed on a fixture and was scanned using a 3D scanner. When the nominal model was generated, the blade edge was cut using EDM to simulate impact failure (Figures 3c and 3d). The damaged blade was then fixed on the fixture and scanned to generate the damaged model.

The scanning system is shown in Figure 4a. Both the nominal and damaged blades were scanned using a structure-light metrology 3D scanner (OptimScan 5M, Shining 3D)

to reconstruct models of them. The blue light 3D scanner using non-contact scanning method can reach an accuracy of 0.005 – 0.015 mm, which yields a highly accurate 3D model. This high accuracy feature is crucial for scanning delicate jet engine blades. Because of the shiny surface of the blade, a developer (Spotcheck SKD-S2 Non-Halogenated Solvent Developer) was sprayed evenly on the surface of the blade prior to scanning. The reconstructed models are shown in Figure 4b and c, respectively.

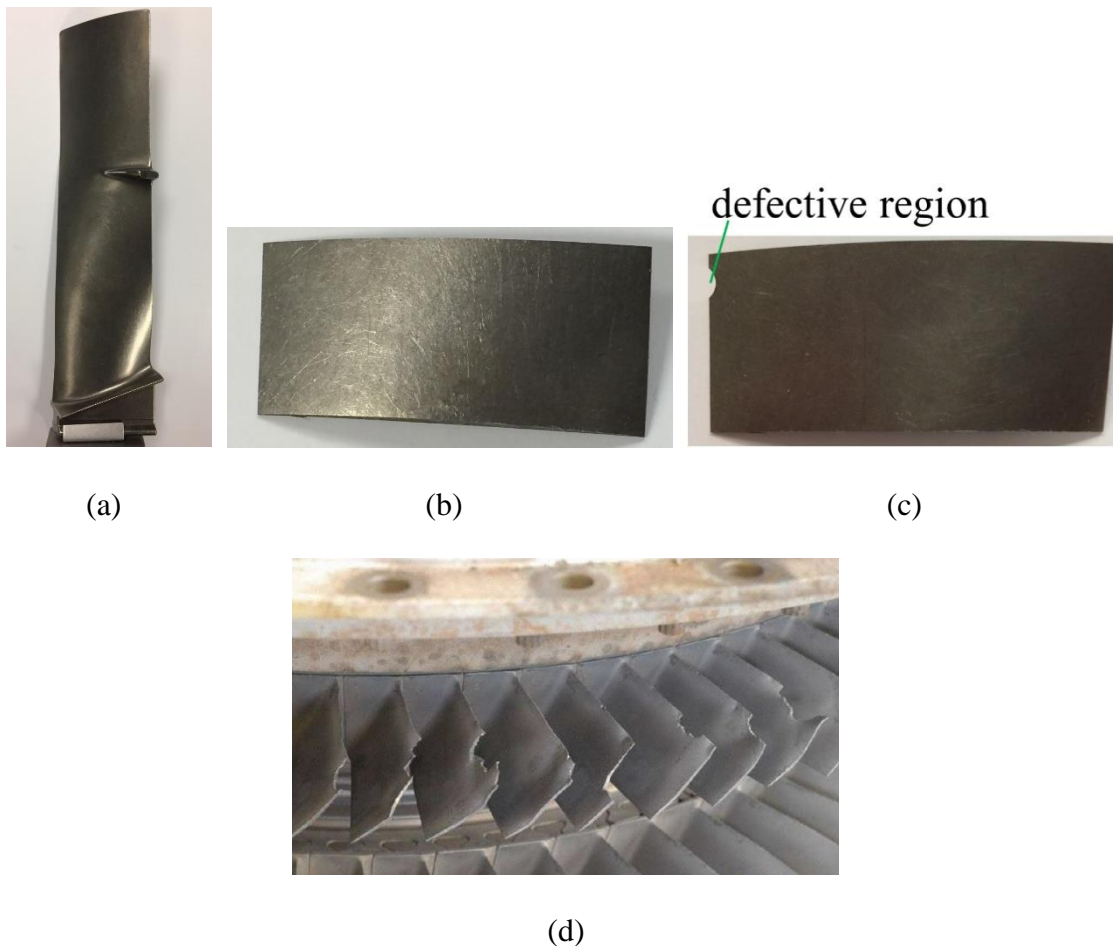
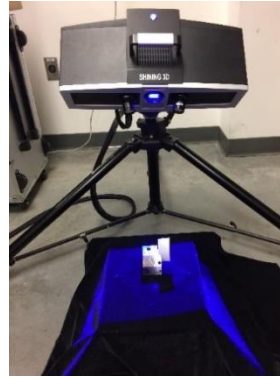


Figure 3. Blade preparation. (a) Original blade without defects; (b) One section of the blade; (c) Damaged blade with defective region on the edge; (d) Compressor blade failure due to impact with foreign objects



(a)



(b)



(c)

Figure 4. Model acquisition process. (a) 3D scanning setup for recreating model of a damaged blade; (b) Reconstructed nominal model; (c) Reconstructed damaged model

2.2. MODEL BEST FIT

It was found that the reconstructed damaged model is in an arbitrary position and orientation with the nominal model as shown in Figure 5a. Therefore, it is required to best-fit the damaged model with the nominal model. The model best-fit process includes the following steps: (1) Surface best fit; (2) Convex-hull centroid best-fit; (3) Cross-section best-fit, and (4) Model best-fit.

Step 1: Surface best fit

Because top surfaces of the damaged and nominal models are identical, they can be used for surface best fit. At first, the point cloud on the top surface of the nominal and

damaged models was obtained and two planes were fitted through the point cloud. The normal vectors of two best-fitted planes were obtained, which is $\vec{n}_n = (v_{nx}, v_{ny}, v_{nz})$ for the nominal model and $\vec{n}_d = (v_{dx}, v_{dy}, v_{dz})$ for the damaged model. Both models were transformed so that the top surfaces are parallel to xoy plane. The normal vector of the xoy plane is $\vec{n}_{oz} = (0, 0, 1)$. This transformation can be represented in Equation (1):

$$\vec{n}_n \bullet A = \vec{n}_{oz} \quad \text{and} \quad \vec{n}_d \bullet B = \vec{n}_{oz} \quad (1)$$

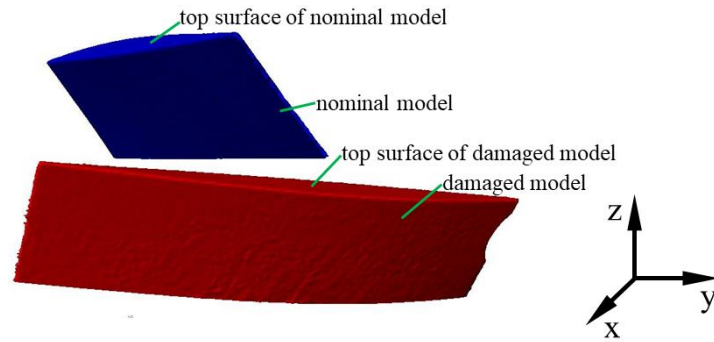
where $A(B)$ is the transformation matrix to transform the top surface of the nominal (damaged) model parallel to the xoy plane.

Figure 5b shows the relative position of nominal and damaged models after transformation. It can be seen that the top surfaces from the two models were parallel to each other although they were not located in the same plane. Therefore, another transformation was executed to the damaged model to translate the top surface of the damaged model to the same position as the nominal model.

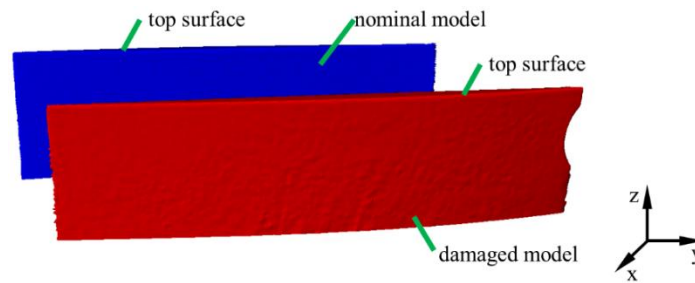
The z coordinates of both transformed planes were obtained, supposing the z coordinate of the plane from the nominal model is z_n and from the damaged model is z_d . Therefore, the transformation vector can be obtained in Equation (2), where T_t is the transformation vector to move the top surface of the damaged model to the same position as the nominal model, V_d is the vertices of the damaged model and V_t is the vertices after transformation. All points of the damaged model were processed with the transformation in Equation (3), after which the top surface of the damaged model can be moved to the same position as the nominal model (Figure 5c).

$$T_i = (0, 0, z_n - z_d) \quad (2)$$

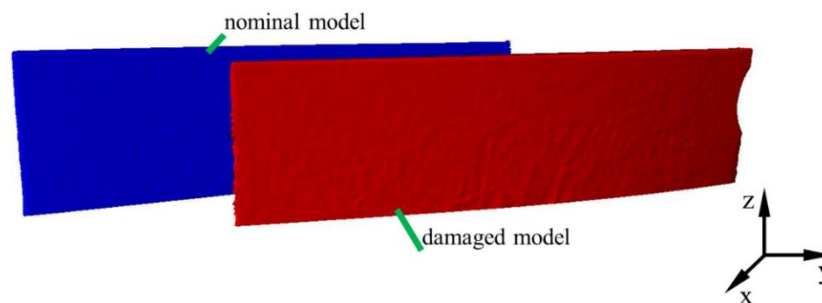
$$V_i = V_d + T_i \quad (3)$$



(a)



(b)



(c)

Figure 5. Surface best-fitting process. (a) The initial position of the reconstructed nominal model and damaged model; (b) Aligned position with a paralleled top surface; (c) Aligned position after surface best fit

Step 2: Convex-hull centroid best-fit

After surface best-fit, both models were sliced with the same plane which is vertical to the oz axis. This plane was selected so that it intersected with the damaged model at the undamaged section. The plane intersected with both models and the intersected cross-sections are shown in Figures 6a and 6b. The convex-hull centroids of both cross-sections were calculated according to [28]. The convex-hull centroid of the layer of the nominal model is (x_n, y_n, z_n) and of the damaged model is (x_d, y_d, z_d) . Translating vector is obtained in Equation (4) to move the convex-hull centroid of the damaged model to the corresponding centroid of the nominal model. All vertices of the damaged model were processed with the transformation in Equation (5). The relative position of the damaged model with the nominal model after convex-hull centroid best-fit is shown in Figure 7.

$$T_t = (x_n - x_d, y_n - y_d, z_n - z_d) \quad (4)$$

$$V_t = V_d + T_t \quad (5)$$

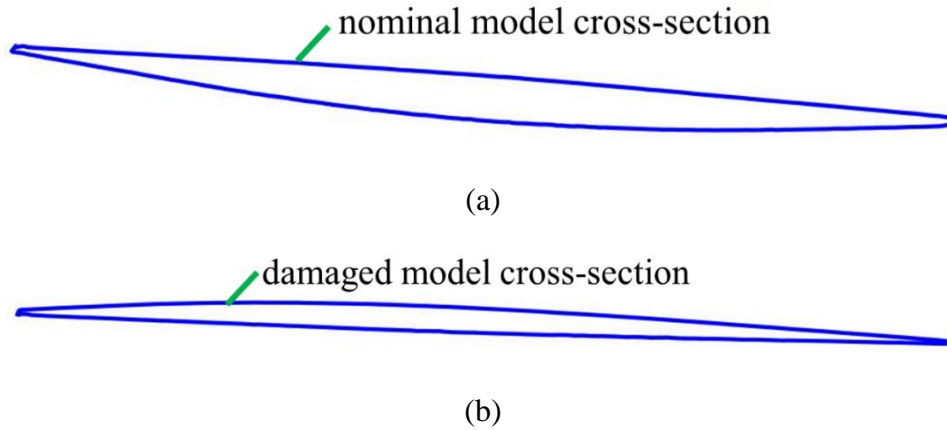


Figure 6. A cross-section of the nominal model (a) and damaged model (b)

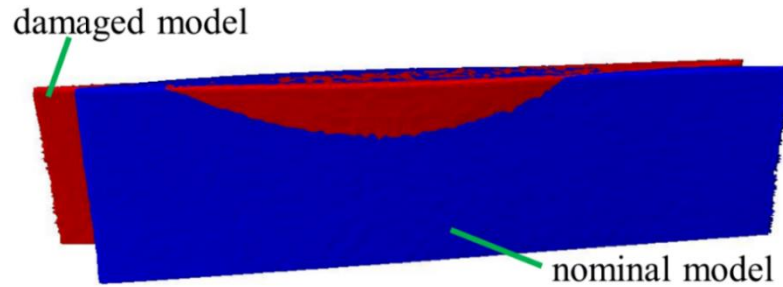


Figure 7. Aligned position after convex-hull centroid best fit

Step 3: Cross-section best-fit

It can be found in Figure 7 that the top surface and convex-hull centroid of the damaged model were best fitted with the nominal model. However, the cross-section of the damaged model is not best fitted with the nominal model. It can be seen that by rotating around the convex-hull centroid, the damaged model cross-section can be aligned with the nominal model cross-section. Therefore, the objective of the cross-section best fit is to find the optimum degree θ that the damaged model should rotate to best-fit with the nominal model. Area of the cross-section of the damaged model is compared with the nominal model to converge to the optimum degree θ .

The method for calculating the area of an irregular polygon is illustrated below. Because the scanned blade STL model is determined by a large number of facets and vertices (190686 faces and 95346 vertices for the nominal model, 175258 faces and 88612 vertices for the damaged model in this study), each cross-section sliced by a plane with the STL model has numerous vertices. Therefore, a curve from one vertex A to the next vertex B illustrated in Figure 8 can be approximated by a line segment connecting vertices A and B .

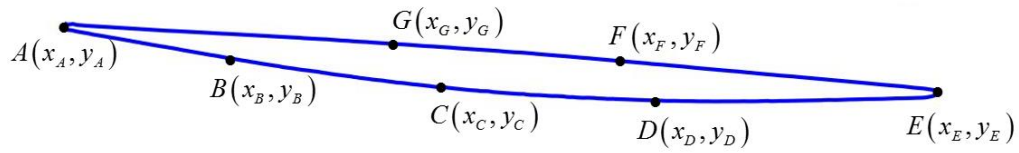


Figure 8. An irregular closed polygon illustrating the area calculation

Suppose a closed irregular polygon as shown in Figure 8 is defined by vertices A, B, C, D, E, F and G . Then the area of the polygon can be obtained by Equation (6) according to the algorithm in [29].

$$Area = \frac{P - Q}{2}$$

(6)

where $P = x_A \bullet y_B + x_B \bullet y_C + x_C \bullet y_D + x_D \bullet y_E + x_E \bullet y_F + x_F \bullet y_G + x_G \bullet y_A$ and

$$Q = y_A \bullet x_B + y_B \bullet x_C + y_C \bullet x_D + y_D \bullet x_E + y_E \bullet x_F + y_F \bullet x_G + y_G \bullet x_A.$$

The equation for obtaining point A' after A rotating around a reference point U is obtained as follows. As shown in Figure 9, (x_0, y_0) is the coordinates of the point A and (x, y) is the coordinates of point A' after point A rotating a degree θ around point $U(a, b)$. Equation (7) can be obtained from the depicted geometrical relationship.

$$\begin{cases} (x-a)^2 + (y-b)^2 = (x_0-a)^2 + (y_0-b)^2 \\ \cos \theta = \frac{(x-a)^2 + (y-b)^2 + (x_0-a)^2 + (y_0-b)^2 - (x-x_0)^2 - (y-y_0)^2}{2\sqrt{(x-a)^2 + (y-b)^2} \sqrt{(x_0-a)^2 + (y_0-b)^2}} \end{cases} \quad (7)$$

Then x and y can be obtained in Equation (8)

$$\begin{cases} x = (x_0 - a) \cos \theta - (y_0 - b) \sin \theta + a \\ y = (y_0 - a) \cos \theta + (x_0 - a) \sin \theta + b \end{cases} \quad (8)$$

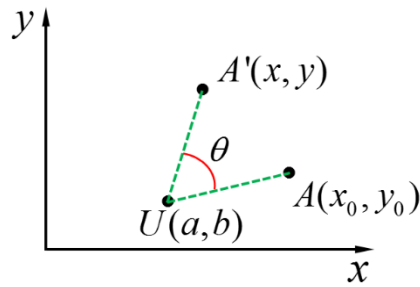


Figure 9. Schematic diagram showing the relationship between A and A'

The diagram of the cross-section best-fit process is shown in Figure 10. To begin with, an initial guess interval $[M, N]$ was given. The cross-section of the damaged model rotated a degree M and N around the convex-hull centroid. Then the intersection of the cross-section of the nominal model with the damaged model was calculated and the overlapping area was obtained as A and B , respectively. Then the cross-section of the damaged model rotated around the convex-hull centroid at $\frac{M+N}{2}$. The area of intersection of the polygon of the nominal model and the damaged model was obtained as C . A comparison between area B and area C was performed. If the area C is larger than area B , then the objective degree $\theta = \frac{N+M}{2}$, $M = \frac{N+M}{2}$ and N is unaltered (N is equal to the previous N). Otherwise, if C is smaller than B but is larger than A , the objective $\theta = \frac{M+N}{2}$, $N = \frac{N+M}{2}$ and M is unaltered (M is equal to the previous M). If C is smaller than B and also smaller than A , the initial guess M and N should be re-selected. The stopping criteria is $|N-M| < 0.001$. Finally, the optimum degree θ for cross-section best fit was obtained.

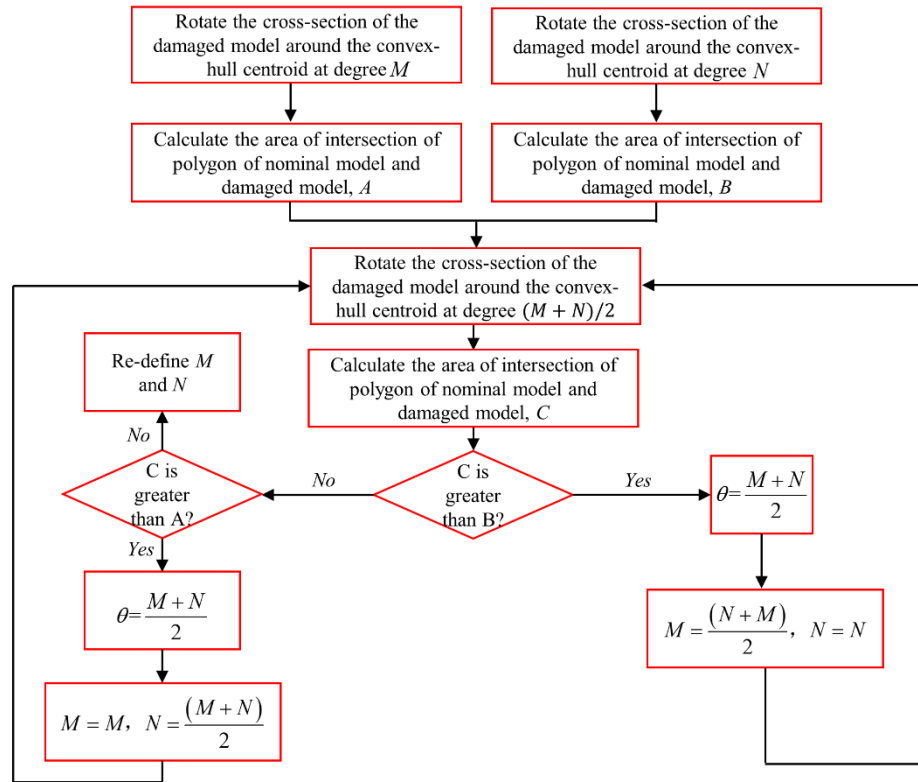


Figure 10. Cross-section best-fit process

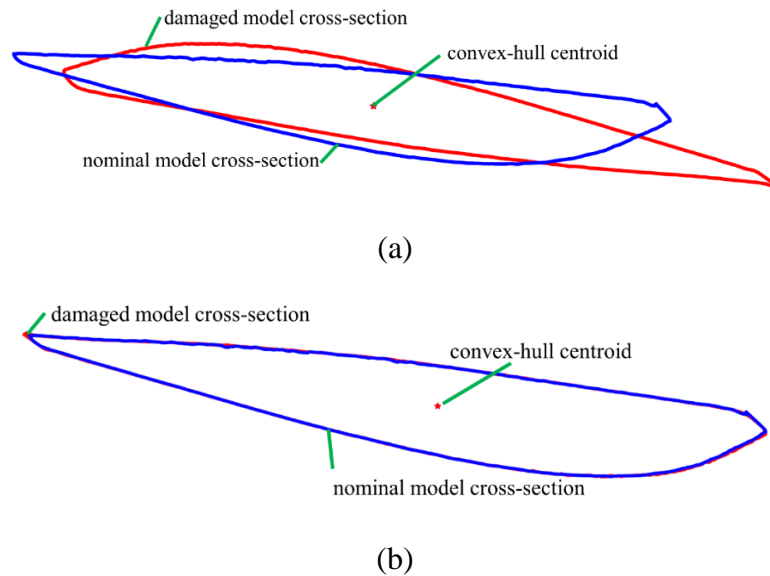


Figure 11. Nominal and damaged profiles before (a) and after (b) cross-section best-fit

Figures 11a and 11b show two cross-sections of nominal and damaged models before and after cross-section best-fit. It can be found that the cross-section of the damaged model was best-fitted with the cross-section of the nominal model after cross-section best-fit process.

Step 4: Model best-fit

After the degree θ was converged, the damaged model rotated degree θ around the vertical vector $(0,0,z_n)$, where z_n is the z coordinate of the convex-hull centroid. After that, the damaged model was best fitted with the nominal model as shown in Figure 12. It can be found in Figure 12 that there is a missing volume on the damaged model and it is required to extract the points from the defective region. These extracted points can be used to reconstruct the model of the missing volume to provide a build-up tool path and machining tool path. Then the laser can follow the build-up path to deposit material in this region. CNC machining tool path can be used to remove the extra deposited material to regain the designed dimensions.

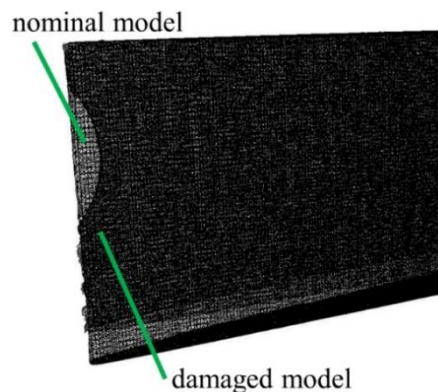


Figure 12. Best-fitted position of the damaged model with nominal model

2.3. DAMAGE DETECTION

Once the damaged model was best fitted with the nominal model, both models were sliced to a number of layers with a layer thickness of 0.5 mm as shown in Figure 13. Then the area of each layer from both models was calculated and compared. Area comparison method was adopted to detect the defective region on the damaged model as shown in Figure 14.

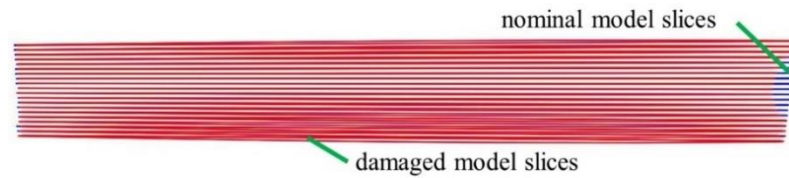


Figure 13. Slices of the nominal model and damaged model

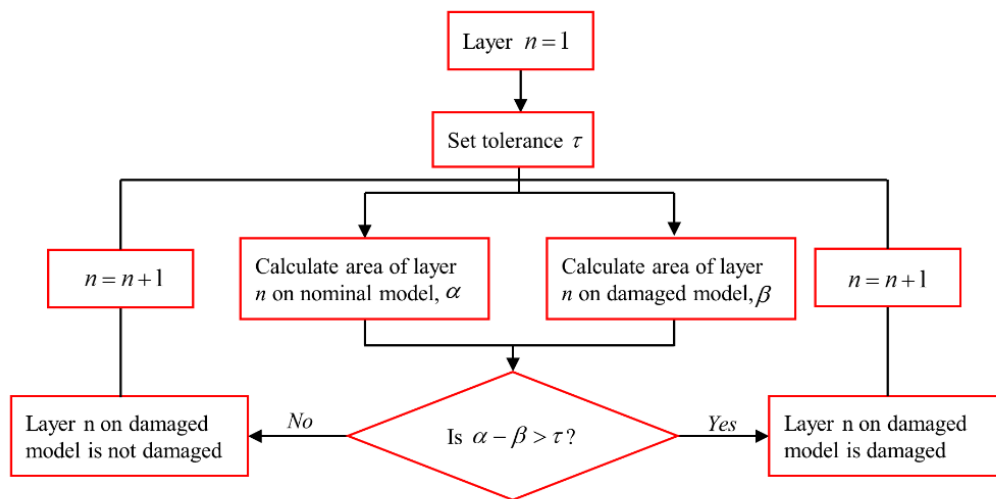


Figure 14. Defect detection process

For each layer, the area of the polygon of the nominal model was obtained as α and the area of the corresponding layer of the damaged model was obtained as β . A tolerance τ was set to deal with the error in the model reconstruction process. If the difference $\Delta = \alpha - \beta$ was larger than the pre-defined tolerance τ , this layer on the damaged model was defined as a defective layer. This process continues throughout all slices. Finally, the damaged layers of the damaged model were defined as shown in Figure 15.

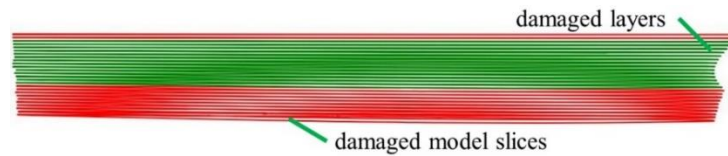


Figure 15. Damaged layers detection

2.4. DAMAGE EXTRACTION

The method for extracting the repair volume is using ray casting method. As shown in Figure 16, two cross-sections at the same layer, one from the damaged model and another one from the nominal model, were sliced by a set of parallel and equidistant rays. Each ray intersects with the cross-section at two intersections. Due to the presence of missing volume, the intersections of casting lines with the cross-section of the damaged model was from a_1b_1 to a_8b_8 . For the corresponding layer from the nominal model, because of no defective area, the intersections of lines with the cross-section was from a_1b_1 to a_9b_9 . It can be seen that the intersections a_9 and b_9 only belong to the defective area, forming

outer points on the blade surface. By reducing the slicing lines interval, more points on the defective region can be obtained. Figure 17a shows the intersections of a number of lines with the layered damaged model and the nominal model. The interval between two adjacent lines is set at 0.2 mm. By searching points in the damaged region, the point cloud that constructing the missing volume was obtained as shown in Figure 17b.

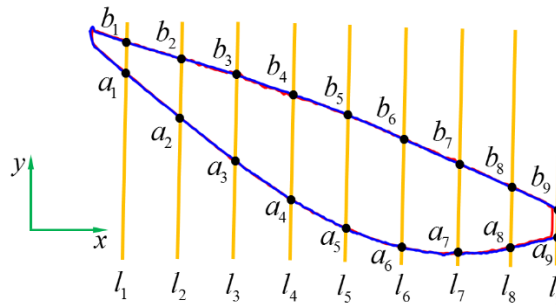


Figure 16. Cross-sections of blade models and intersections with casting rays

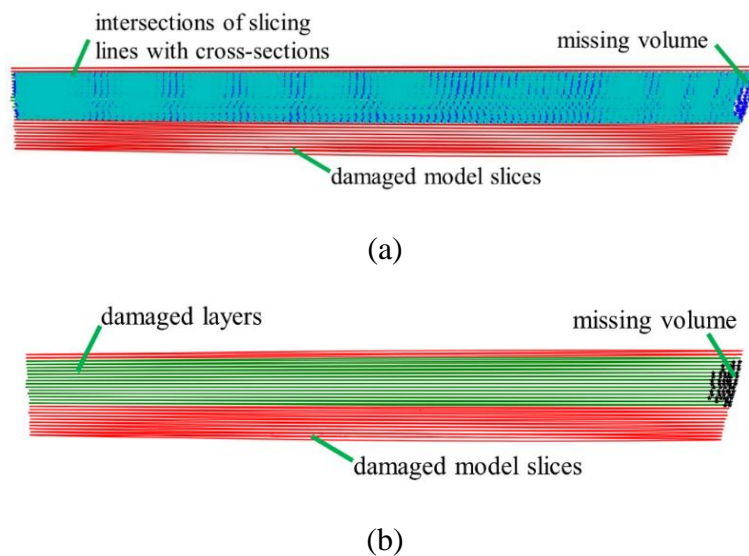


Figure 17. (a) Damage detection process; (b) Damage extraction processes

3. BLADE REPAIR EXPERIMENT

3.1. EXPERIMENTAL SETUP

The DMD system as shown in Figure 18 employed in this study consists of a laser heat source (YLR-1000-MM-WC), powder feeder (Model 1200, Bay State Surface Technologies), 3-axis motion table, shielding gas units. Fiber laser with maximum power of 1000 W was used as the laser source. The laser head is tilted and the powder feed nozzle is vertical. The laser beam diameter which is focused on the damaged blade is 1.8 mm. The relative movement between the laser head and the blade was achieved by a 3-Axis motion table. Argon gas was used as the shielding gas to avoid oxidation to the titanium blade. Ti-6Al-4V particles were used as the deposited material. Micrograph of target particles was taken using a Field Emission Scanning Electron Microscopy (Hitachi S4700) and was shown in Figure 18d. It can be found that most powders were spherical although some irregularly shaped powders were detected. Table 1 summarizes the processing parameters used in the experiment. It should be noted that the highest thickness of the extracted missing volume geometry is 1.22 mm, which is smaller than the laser beam diameter. Therefore, only one track was planned for each layer. The tool path was shown in Figure 18c.

Table 1. The DMD processing parameters

Material	Laser power (W)	Powder flow rate (g/min)	Scan speed (mm/min)	Nozzle stand-off distance (mm)
Ti6Al4V	400	2.8	200	10

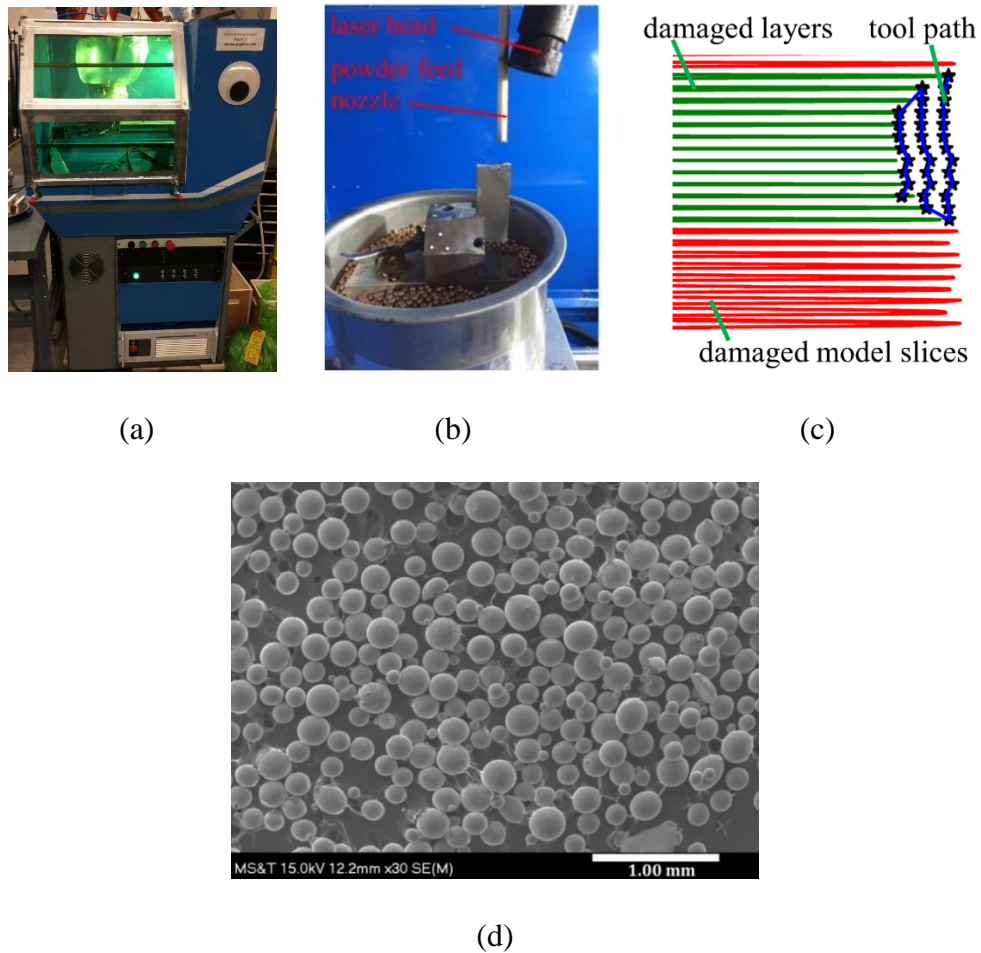


Figure 18. (a) DMD system; (b) DMD experimental setup; (c) Tool path generation for material deposition; (d) SEM images of Ti-6Al-4V particles

3.2. REPAIR RESULT AND MICROSTRUCTURE EVALUATION

The images of the blade after metal deposition and after post-machining is depicted in Figure 19. The microstructure of deposits was analyzed to evaluate the repair quality. The blade was sectioned to prepare samples for microstructure analysis. The cross-section of the sample was ground using sand papers from 120 silicon carbide grids to 1200 grids

and polished using 0.05 microns silica suspension. The sample was mounted, etched using Kroll's reagent, and examined using HIRO KH-8700 digital optical microscope.

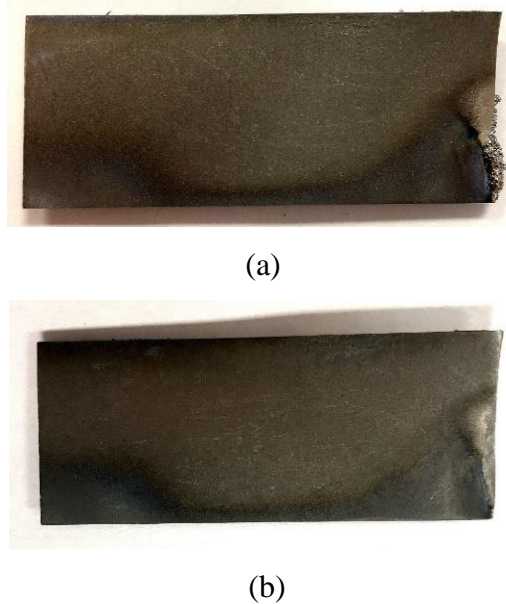


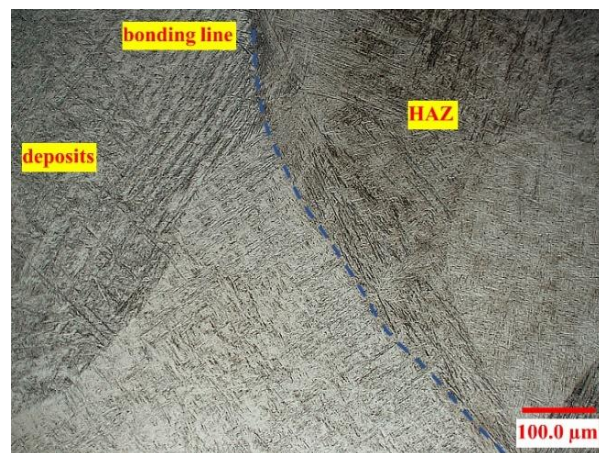
Figure 19. Compressor blade after the DMD process (a) and after machining (b)

The microstructure of the substrate in Figure 20a shows equiaxed alpha grains in the beta matrix, which is a common structure for forged and annealed Ti-6Al-4V alloy. The microstructure of deposits exhibited Widmanstätten pattern [3]. Further analysis reveals a mixture of alpha and beta phases in the deposits, which is a typical structure observed in DMD-fabricated titanium alloys [30]. Beta transit was initiated by solidification from melting temperature to room temperature, passing through beta transit temperature (800 °C - 1000°C). Very thin lamellar structure was caused by the high cooling rate associated in the DMD process. Alpha acicular phase near the interface grows

perpendicular to the laser scanning direction and along the direction of solidification. It can also be seen that the as-deposited material is fully dense and free of defects. The interface between deposits and substrate is defect-free. This good metallurgical bonding guarantees the functionality of repaired blades.



(a)



(b)

Figure 20. Microstructure of substrate (a) and as-deposited titanium alloy (b)

4. CONCLUSION

Detection and reconstruction of the defective region on a damaged blade are crucial to provide repair volume geometry for building-up toolpath generation. For this purpose, this paper presents a damage detection and reconstruction algorithm for blade repair. Reverse engineering was adopted to generate the nominal and damaged models of a compressor blade. The reconstructed damaged model was best fitted with the nominal model by a transformation matrix and using overlapping area comparison method. Taking the area comparison method, the defective layers of the damaged model were detected. Therefore, the damaged blade was sectioned into two parts: an undamaged section that is the same as the nominal model and damaged section that should be repaired. A set of parallel and equidistant casting rays were used to intersect damaged layers to extract the repair volume. Finally, laser scanning tool path was generated and DMD experiment was performed to deposit Ti-6Al-4V particles on the defective region to validate the repair. Microstructure analysis was carried out to evaluate the repair. The result shows that the damage detection and reconstruction method gives a feasible way for blade repair.

ACKNOWLEDGMENTS

This project was supported by National Science Foundation Grants CMMI-1547042 and CMMI 1625736, and the Intelligent Systems Center, Center for Aerospace Manufacturing Technologies, and Material Research Center at Missouri S&T. Their financial support is greatly appreciated.

REFERENCES

- [1] J. Gao, J. Folkes, O. Yilmaz, and N. Gindy, "Investigation of a 3D Non-Contact Measurement based Blade Repair Integration System," *Aircraft Engineering and Aerospace Technology*, vol. 77, pp. 34-41, 2005.
- [2] R. Dewangan, J. Patel, J. Dubey, P. K. Sen, and S. Kumar Bohidar, "Gas Turbines Blades – A Critical Review of Failure on First and Second Stages," *International Journal of Mechanical Engineering and Robotics Research*, vol. 4, pp. 216-223, 2015.
- [3] S. L. Lu, M. Qian, H. P. Tang, M. Yan, J. Wang, and D. H. StJohn, "Massive Transformation in Ti-6Al-4V Additively Manufactured by Selective Electron Beam Melting," *Acta Materialia*, vol. 104, pp. 303-311, 2016.
- [4] G. Xiao and Y. Huang, "Equivalent Self-Adaptive Belt Grinding for the Real-R Edge of an Aero-Engine Precision-Forged Blade," *International Journal of Advanced Manufacturing Technology*, vol. 83, pp. 1697-1706, 2016.
- [5] O. Yilmaz, N. Gindy, and J. Gao, "A Repair and Overhaul Methodology for Aeroengine Components," *Robotics and Computer-Integrated Manufacturing*, vol. 26, pp. 190-201, 2010.
- [6] L. M. Amoo, "On the Design and Structural Analysis of Jet Engine Fan Blade Structures," *Progress in Aerospace Sciences*, vol. 60, pp. 1-11, 2013.
- [7] M. Hetmańczyk, L. Swadzba, and B. Mendala, "Advanced Materials and Protective Coatings in Aero-Engines Application," *Journal of Achievements in Materials and Manufacturing Engineering*, vol. 24, pp. 372-381, 2007.
- [8] N. P. Padture, M. Gell, and E. H. Jordan, "Thermal Barrier Coatings for Gas Turbine Engine Applications," *Science*, vol. 296, pp. 280-284, 2002.
- [9] J. M. Wilson, C. Piya, Y. C. Shin, F. Zhao, and K. Ramani, "Remanufacturing of Turbine Blades by Laser Direct Deposition with its Energy and Environmental Impact Analysis," *Journal of Cleaner Production*, vol. 80, pp. 170-178, 2014.
- [10] A. Gasser, G. Backes, I. Kelbassa, A. Weisheit, and K. Wissenbach, "Laser Additive Manufacturing: Laser Metal Deposition (LMD) and Selective Laser Melting (SLM) in Turbo-Engine Applications," *Laser Material Processing*, pp. 58-63, 2010.

- [11] L. Song, V. Bagavath-Singh, B. Dutta, and J. Mazumder, "Control of Melt Pool Temperature and Deposition Height During Direct Metal Deposition Process," *International Journal of Advanced Manufacturing Technology*, vol. 58, pp. 247-256, 2012.
- [12] S. Nowotny, S. Scharek, E. Beyer, and K.-H. Richter, "Laser Beam Build-Up Welding: Precision in Repair, Surface Cladding, and Direct 3D Metal Deposition," *Journal of Thermal Spray Technology*, vol. 16, pp. 344-348, 2007.
- [13] T. Petrat, B. Graf, A. Gumenyuk, and M. Rethmeier, "Laser Metal Deposition as Repair Technology for a Gas Turbine Burner Made of Inconel 718," *Physics Procedia*, vol. 83, pp. 761-768, 2016.
- [14] D. D. Gu, W. Meiners, K. Wissenbach, and R. Poprawe, "Laser Additive Manufacturing of Metallic Components: Materials, Processes and Mechanisms," *International Materials Reviews*, vol. 57, pp. 133-164, 2012.
- [15] A. Jabbari and K. Abrinia, "A Metal Additive Manufacturing Method: Semi-Solid Metal Extrusion and Deposition," *International Journal of Advanced Manufacturing Technology*, vol. 94, pp. 3819-3828, 2017.
- [16] H. D. Morgan, J. A. Cherry, S. Jonnalagadda, D. Ewing, and J. Sienz, "Part Orientation Optimisation for the Additive Layer Manufacture of Metal Components," *International Journal of Advanced Manufacturing Technology*, vol. 86, pp. 1679-1687, 2016.
- [17] M. Fera, R. Macchiaroli, F. Fruggiero, and A. Lambiase, "A New Perspective for Production Process Analysis using Additive Manufacturing-Complexity vs Production Volume," *International Journal of Advanced Manufacturing Technology*, vol. 95, pp. 673-685, 2017.
- [18] J. Ruan, K. Eiamsa-ard, and F. W. Liou, "Automatic Process Planning and Toolpath Generation of a Multiaxis Hybrid Manufacturing System," *Journal of Manufacturing Processes*, vol. 7, pp. 57-68, 2005.
- [19] D. Boisselier, S. Sankaré, and T. Engel, "Improvement of the Laser Direct Metal Deposition Process in 5-axis Configuration," *Physics Procedia*, vol. 56, pp. 239-249, 2014.
- [20] W. Li, X. Chen, L. Yan, J. Zhang, X. Zhang, and F. Liou, "Additive Manufacturing of a New Fe-Cr-Ni Alloy With Gradually Changing Compositions with Elemental Powder Mixes and Thermodynamic Calculation," *International Journal of Advanced Manufacturing Technology*, vol. 95, pp. 1013-1023, 2017.

- [21] C. G. Mançanares, E. de S. Zancul, J. da Silva, and P. A. Cauchick Miguel, "Additive Manufacturing Process Selection based on Parts' Selection Criteria," *International Journal of Advanced Manufacturing Technology*, vol. 80, pp. 1007-1014, 2015.
- [22] M. Vaezi, H. Seitz, and S. Yang, "A Review on 3D Micro-Additive manufacturing Technologies," *International Journal of Advanced Manufacturing Technology*, vol. 67, pp. 1721-1754, 2013.
- [23] J. B. Jones, P. McNutt, R. Tosi, C. Perry, and D. I. Wimpenny, "Remanufacture of Turbine Blades by Laser Cladding, Machining and In-Process Scanning in a Single Machine," *International Solid Freeform Fabrication Symposium Conference*, Texas, USA, pp. 821-827, 2012.
- [24] J. Zheng, Z. Li, and X. Chen, "Worn Area Modeling for Automating the Repair of Turbine Blades," *International Journal of Advanced Manufacturing Technology*, vol. 29, pp. 1062-1067, 2006.
- [25] P. Hong-Seok and T. U. Mani, "Development of an Inspection System for Defect Detection in Pressed Parts using Laser Scanned Data," *Procedia Engineering* vol. 69, pp. 931-936, 2014.
- [26] H. Junjie and L. Liangyu, "Research of Key-Technique on Automatic Repair System of Plane Blade Welding," *International Conference on Control, Automation and Systems Engineering*, Singapore, pp. 1-4, 2011.
- [27] J. Gao, X. Chen, O. Yilmaz, and N. Gindy, "An Integrated Adaptive Repair Solution for Complex Aerospace Components through Geometry Reconstruction," *International Journal of Advanced Manufacturing Technology*, vol. 36, pp. 1170-1179, 2008.
- [28] C. B. Barber, D. P. Dobkin, and H. Huhdanpaa, "The Quickhull Algorithm for Convex hulls," *ACM Transactions on Mathematical Software*, vol. 22, pp. 469-483, 1996.
- [29] R. Nürnberg, "Calculating the Area and Centroid of a Polygon," Available: <http://local.wasp.uwa.edu.au/~pbourke/geometry/lineline/polyarea/>.
- [30] A. Reichardt, R. P. Dillon, J. P. Borgonia, A. A. Shapiro, B. W. McEnerney, T. Momose, and P. Hosemann, "Development and Characterization of Ti-6Al-4V to 304L Stainless Steel Gradient Components Fabricated with Laser Deposition Additive Manufacturing," *Materials & Design*, vol. 104, pp. 404-413, 2016.

IV. DAMAGE RECONSTRUCTION FROM TRI-DEXEL DATA FOR LASER-AIDED REPAIRING OF METALLIC COMPONENTS

Xinchang Zhang¹, Wei Li¹, Katelyn M. Adkison², and Frank Liou¹

¹Department of Mechanical and Aerospace Engineering,
Missouri University of Science and Technology, Rolla, MO 65409, USA

²Department of Material Science and Engineering,
Penn State University, University Park, PA, 16801, USA

ABSTRACT

The laser-assisted additive manufacturing process for component repair requires the repair volume to generate the tool path for building up specific material in the worn area. This paper introduces a damage reconstruction algorithm benefits from tri-dexel modeling. At first, nominal and damaged models were acquired through robot-aided 3D scanning process. Then damaged models were aligned with nominal models by aligning the associated features using the least-squares method. The area covering the defective region was manually selected, and the minimum bounding box of the area was defined and subsequently sliced into a number of grids according to a user-defined grid interval. After that, rays were projected from each grid node in three orthogonal directions to intersect the selected region of nominal and damaged models. Point set in the damaged zone was extracted by comparing intersections of rays with nominal and damaged models. Stereolithography model of damage was reconstructed based on extracted point cloud using Screened Poisson Surface Reconstruction algorithm. Reconstructed damage was compared

with real damage to test the accuracy of the damage reconstruction process. Regained damage was sliced into layers to generate the tool path for material deposition. Repair experiments were conducted to deposit materials in the defective area. Illustrating examples were implemented at last to test the functionality and reliability of the proposed methodology.

Keywords: Damage Reconstruction; Tri-Dexel Model; Component Repair; Additive Manufacturing

1. INTRODUCTION

A promising application of Additive Manufacturing (AM) process is for component restoration, in which the damaged region of a worn part is defined, and metal powders are conveyed into the damaged zone, which will experience melt and solidification to recover the missing geometry [1]. The critical surfaces of the repaired component then undergo final machining before getting reinserted into service [2]. Repair of costly metallic components (e.g., titanium aircraft parts or high-precision die/mold) is crucial for maximizing service life to reduce costs of replacement [3].

Among categories of AM technologies according to ASTM F42, Directed Energy Deposition (DED) which covers a range of terminologies such as direct metal deposition, laser engineered net shaping and laser cladding is appropriate for repairing high-value complex components that need frequent replacement but are expensive to machine. Laser-aided DED system consists of a powder feed nozzle on a multi-axis table, which deposits materials melted by the laser beam on the target surface, where it solidifies [4]. DED

process can print a wide variety of metals including titanium [5, 6], nickel- and cobalt-based superalloys [7-9], tool steels [10, 11] – all of which are commercially available, and customized materials by mixing powders with specified composition ratio [12]. Besides, with optimized parameters, the process can precisely deposit materials in a specified area with a small heat affected zone, enabling repair of fine thin-wall structures [13, 14]. Moreover, the metallurgical bond can be formed between deposits and substrates to guarantee excellent interfacial adhesion strength [15]. All these specialties make DED process for component repair a research hotspot.

Reconstructing worn geometry is essential in the remanufacturing process. That is because, similar to desktop 3D printer where STL model of a part is needed to generate a printing tool path, for component repair, the geometry of damage is also crucial to generate tool path so that materials can be precisely built-up on the desired region. It is possible to manually generate tool paths for very simple cases. For example, Bennett et al. investigated the repair of a grey cast iron diesel engine component by depositing 316L stainless steel following a manually defined spiral tool path [16]. Pinkerton et al. machined V-slot and U-slot defects on AISI H13 tool steel substrates and refilled the damaged area with H13 powder [17]. Liu et al. created circular groove defects on TC17 (Ti-5Al-2Sn-2Zr-4Mo-4Cr) plates and performed repair by depositing TC17 powder [18]. Similar work was conducted in [19, 20] although the target materials are different. In the aforementioned research, geometries of defects are very simple and regular. Thus, it is able to generate a tool path manually. However, in the majority situation, damaged structures are complex, which requires a significant amount of time, if possible, to define the worn shape manually. In addition, the manual-defined damage is error-prone and hence is inappropriate for

precise parts repair. Therefore, automated damage reconstruction strategies have been proposed to address this issue.

Gao et al. introduced an approach by comparing the damaged model with the nominal model to define the damaged geometry [21]. Wilson et al. demonstrated a method to generate the damage of an aero-engine blade by using the extruded fracture surface to cut the nominal model [22]. A damaged blade model was acquired using a laser scanning system and for regaining the damaged geometry, distance from acquired points to the nominal surface was calculated [23]. Points with distance beyond acceptable tolerance were extracted as worn area. Defect detection based on Iterative Closest Point algorithm was presented in [24] where the acquired data was registered on the CAD model. However, the research didn't investigate defect reconstruction. He and Li proposed a curved surface extension method to reconstruct the missing geometry of a blade based on continuous curvature [25]. Zhang et al. investigated a damage detection and reconstruction algorithm for compressor blade repair using ray casting method [26]. As we can see, the existing damage reconstruction algorithms are mainly focusing on the aero-engine blade. Therefore, a damage reconstruction approach that can be effectively implemented to a variety of components is urgently needed.

In the present research, a novel damage reconstruction method was proposed based on tri-dexel modeling. At first, damaged and nominal models were acquired using a robot-assisted 3D scanning configuration. Then damaged models were aligned with nominal models based on the associated features. After that, the damaged zone was manually selected, and the minimum bounding box of the selected area was obtained. The minimum bounding box was sliced to a number of grids based on a user-defined grid interval δ .

Casting rays in three orthogonal directions were emitted from each node of the grid to intersect the nominal and damaged models. Points in the damaged area were automatically extracted by comparing intersections with both models. STL model of the damage was reconstructed based on extracted points. Toolpath was generated by slicing the STL model into layers. Repair experiment was conducted to deposit materials in the defective area following the tool path. To test the accuracy of damage reconstruction from tri-dexel data, damage of a CAD model was obtained and the damage was compared with the real damage. Finally, several illustrating examples were implemented to show the feasibility of the proposed damaged reconstruction approach.

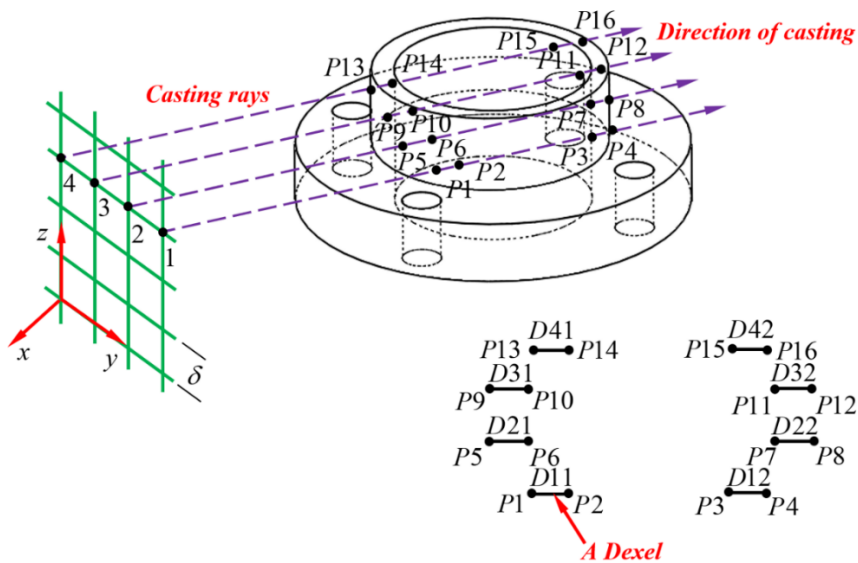
2. DAMAGE RECONSTRUCTION METHODOLOGY

2.1. TRI-DEXEL MODEL AND DATA STRUCTURE

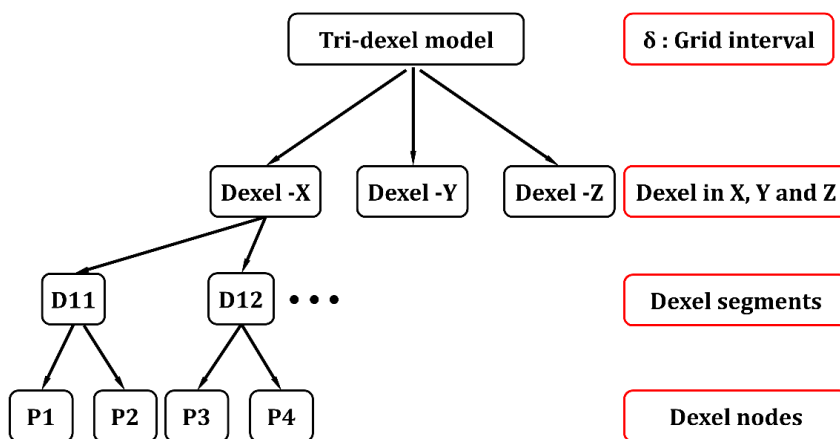
Dexel model was first proposed by Tim Van Hook in [27]. A dexel model represents a solid model by a number of columns along a certain direction (i.e. x-axis direction) as shown in Figure 1a. To generate a dexel model from a polyhedral model, casting rays at a specific interval δ are utilized to intersect the polyhedral model. Intersections of the rays with the model are called dexel points (such as $P_1, P_2, P_3 \dots$). The line segment connecting adjacent dexel points is a dexel (such as $D_{11}, D_{12}, D_{21} \dots$).

The data structure of the tri-dexel model is depicted in Figure 1b. In the beginning, the minimum bounding box of an object was obtained and sliced into grids with an interval δ . Then casting rays in three directions are emitted at grid nodes. A tri-dexel model was formed by three individual dexels along each specified direction (such as dexel-X, dexel-

Y, and dixel-Z). Dixel along each direction consists of an amount of dixel segments and dixel nodes. All the dixel segments and nodes joined together to create a tri-dixel model.



(a)



(b)

Figure 1. (a) Single dixel representation; (b) Data structure of a tri-dixel model

Compared with voxel model which represents an object with a large collection of small cubes (Figure 2b), the single-dexel model representation can yield a high accuracy except at certain locations where the normal is nearly perpendicular to the dexel direction (Figure 2c). Therefore, the accuracy of single-dexel model relies on the orientation of the model relative to casting rays. Tri-dexel model (Figure 2d) with rays along three orthogonal directions, i.e. x-, y-, and z-axis direction, could achieve good accuracy to precisely represent the polyhedral model. Tri-dexel model has been used for virtual sculpting [28-31] and geometric simulation of additive manufacturing [32-34].

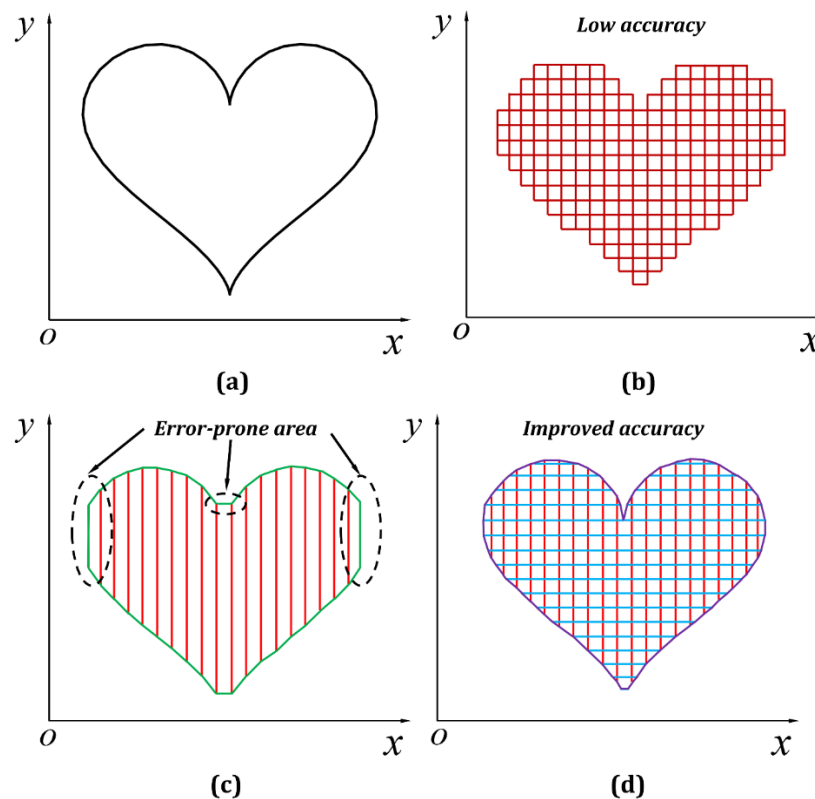


Figure 2. Comparison of a cross-section of a polyhedral model (a), voxel model (b), single-dexel model (c) and tri-dexel model (dexel along z-axis not shown) (d)

2.2. ROBOT-ASSISTED 3D SCANNING

In order to reconstruct damaged geometry, it is necessary to recreate the model of a worn part using scanners. Model of the nominal part can be regenerated by scanning the original part or from the CAD database. In this study, models of objects were recreated using a structured light metrology 3D scanner (OptimScan 5M, Shining 3D Co., Figure 3).

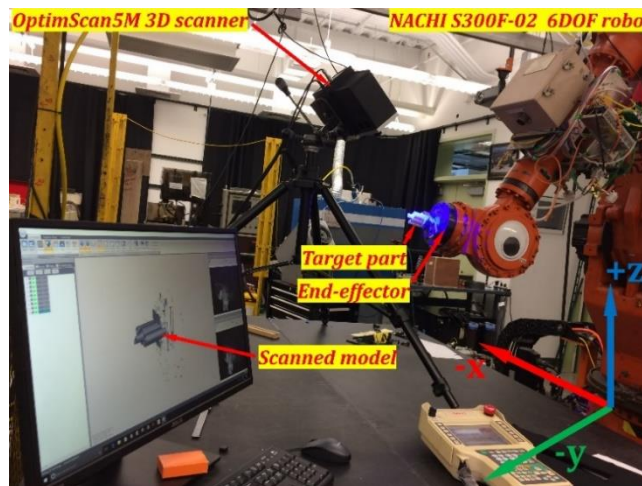


Figure 3. The Nachi robot and 3D scanner setup

To automate the scanning process, a scanning system assisted by a 6-axis robot (NACHI SC300F-02) was proposed as shown in Figure 3. In the process, an object is clamped on the robot end-effector. The scanner is fixed while the position of the end-effector is precisely manipulated in the view of the 3D scanner cameras so that all surfaces of the object can be captured. The robot eliminates the time-consuming process of manually turning the object to find appropriate angles to capture all surfaces.

A model is used to assess the configuration to find general scanning procedures and common problems (Figure 4a). The test model was designed in OpenSCAD and printed on the Stratasys uPrint SE plus FDM 3D printer. The dimensions of the model are 120 mm × 23.24 mm × 49.41 mm.

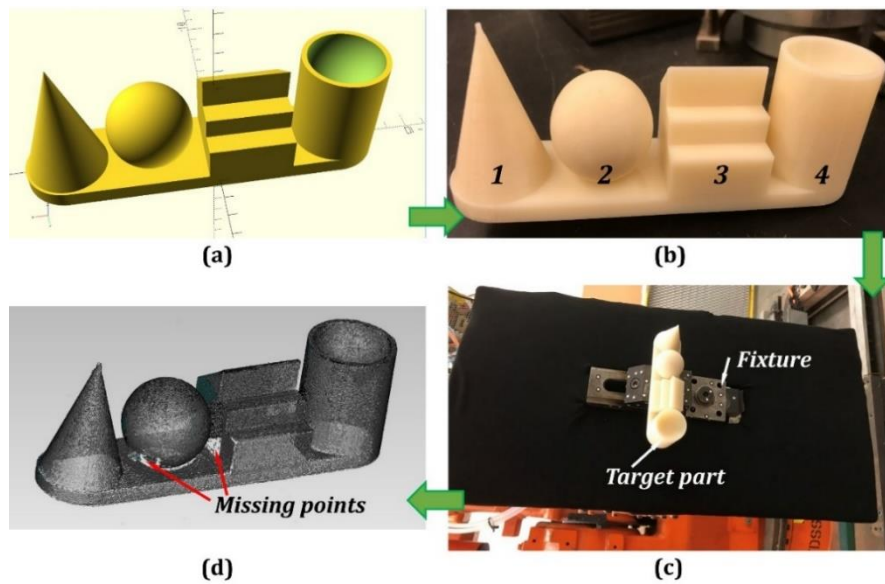


Figure 4. Evaluation of the robot-assisted part scanning process. (a) 3D model designed in OpenSCAD; (b) 3D printed ABS plastic part; (c) Part clamped to Nachi end-effector; (d) A complete scan of the test model

The model was designed with features to simulate common scenarios. (1) Cone: to test the ability to generate accurate point cloud at fine tips and curved surfaces of conical geometries. (2) Sphere: to test the ability to scan points at the boundary of the sphere and the base. (3) Stairs: to test the ability to scan depth accurately and fine edges of stairs. (4) Cylinder: the bowl in the top is to test the ability to scan an object with interreflections.

18 scans were taken at identical angles for the first five-axis of the robot but with rotating the end-effector with an increment of 20° . Using the robot to adjust the orientation of the object allows the part to be scanned entirely, without the cumbersome steps of altering the scanner head angles. The scanned point cloud is shown in Figure 4d. After scanning, there are still missing points between closely spaced objects, especially on sides of the stairs and underneath the sphere. The missing points are likely due to both cameras not being able to see the shapes at the same time. In order to correct this issue, one can increase scan steps of the missing areas to capture as more originally missed points as possible.

2.3. MODEL RECONSTRUCTION AND MODEL ALIGNMENT

A die is adopted to illustrate the damage reconstruction process from tri-dexel data. The nominal model as shown in Figure 5a was obtained by scanning the nominal part. After that, a defect was created on the convex of the die using wire electrical discharge machining. Then the damaged part was scanned to reconstruct the damaged model which is shown in Figure 5c. Both nominal and damaged models were output in STL format. It is usually observed that the scanned damaged model is in an arbitrary position and orientation with the nominal model as shown in Figure 5e. The damaged model must be aligned with the nominal one in order to perform damage reconstruction. In this study, mutual features of the nominal and damaged models including convex-hull centroids and cross-sections were utilized for alignment.

The aligning process is presented in Figure 5. The nominal and damaged models were sliced into a number of layers and the convex-hull centroid of each layer was

calculated. The steps of generating convex-hull centroids and cross-sections of a model are presented below.

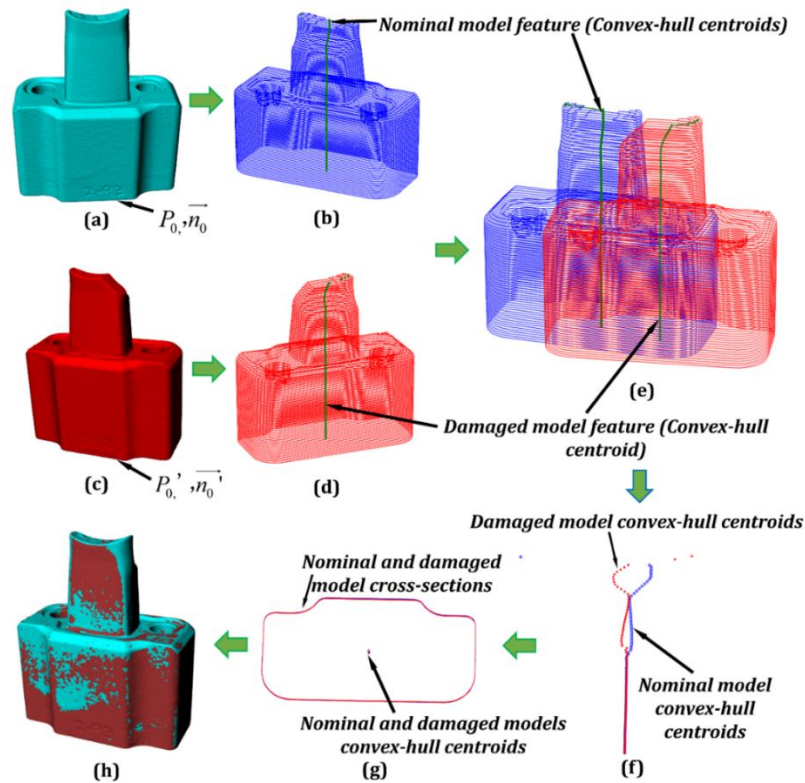


Figure 5. Model alignment. (a) Nominal model; (b) Nominal model cross-sections and convex-hull centroids; (c) Damaged model; (d) Damaged model cross-sections and convex-hull centroids; (e) Models before alignment; (f) Aligned convex-hull centroids; (g) Aligned cross-sections; (h) Aligned models

Step 1: Select an initial slice vertex P_0 and normal direction n_0 . The vertex P_0 is the point where the slicing initiates and the normal direction n_0 is the slicing direction.

Step 2: Once the initial slicing vertex and direction were defined, a planar reference going through the slicing vertex was used to slice the model to generate a cross-section.

After that, the slicing plane moved to slice another layer according to a layer thickness (0.6 mm for the current model). The slicing process continues through the model. The sliced nominal and damaged models are shown in Figure 5b and 5d, respectively.

Step 3: The convex-hull centroids of the nominal and damaged models were calculated and obtained as shown in Figure 5b and 5d, respectively.

The model alignment algorithm is to align the associated features (e.g. convex-hull centroids, cross-sections) of the nominal and damaged models [35]. The damaged model can be aligned with the nominal model via three translation values x, y, z and three rotational variables α, β, γ . The least-squares method was used to acquire x, y, z and α, β, γ . The objective of the least-squares method is to minimize the distance of the transformed points $P_d^t = (x_d^t, y_d^t, z_d^t)$ to the points of the nominal model $P_n = (x_n, y_n, z_n)$. The models before and after alignment are depicted in Figure 5e and 5h, respectively.

2.4. DAMAGE RECONSTRUCTION FROM TRI-DEXEL DATA

The flowchart of the proposed damage reconstruction algorithm is illustrated in Figure 6, which includes the following eight steps:

Step 1: Import the aligned damaged and nominal STL models for processing.

Step 2: Select an area that covers damaged geometry. Computing intersections of casting rays with the entire model is very time-consuming, especially for 3D scanned models because of numerous small facets. Reducing grid interval δ to improve accuracy will also increase computing time significantly. Therefore, by selecting the area that covers the damage, the damage reconstruction process can be accelerated.

Step 3: Compute the minimum bounding box of the selected area.

Step 4: Slice the minimum bounding box into grids according to a user-defined grid interval δ . Three initial casting rays along x-, y- and z-axis were created, respectively.

Step 5: Calculate intersections of the casting rays in three orthogonal directions with the nominal and damaged models.

Step 6: The quantity and values of intersections from the nominal and damaged models were compared. Based on the comparison, damaged points were extracted.

Step 7: The extracted point set was output.

Step 8: After the above steps, the X, Y, and Z coordinates were updated according to the grid interval to generate the next rays to intersect the nominal and damaged models.

The above steps continue until the casting rays reach the boundary of the minimum bounding box. The extracted points form the damaged areas that need to be rebuilt.

Step 6 in the above flowchart is crucial to extract points in the damaged zone. The method for determining such points was illustrated as follows: As shown in Figure 7a, $P(x_p, y_p, z_p)$ and $Q(x_q, y_q, z_q)$ are intersections of a ray with the nominal model. In general, there are two situations of the intersections between nominal and damaged models: (1) Identical intersection quantity but different values as shown in Figure 7b. This situation can be taken place by partial fracture such as hole fracture shown in Figure 7b. (2) Different intersection quantity as shown in Figures 7c and 7d. In Figure 7c, the inner hole is fractured, and some materials are missing. Therefore, no intersections will be obtained from casting ray with the damaged model. In Figure 7d, a slot was created inside the hole, resulting in four intersections (P''', M, N, Q''') of the ray with the damaged model.

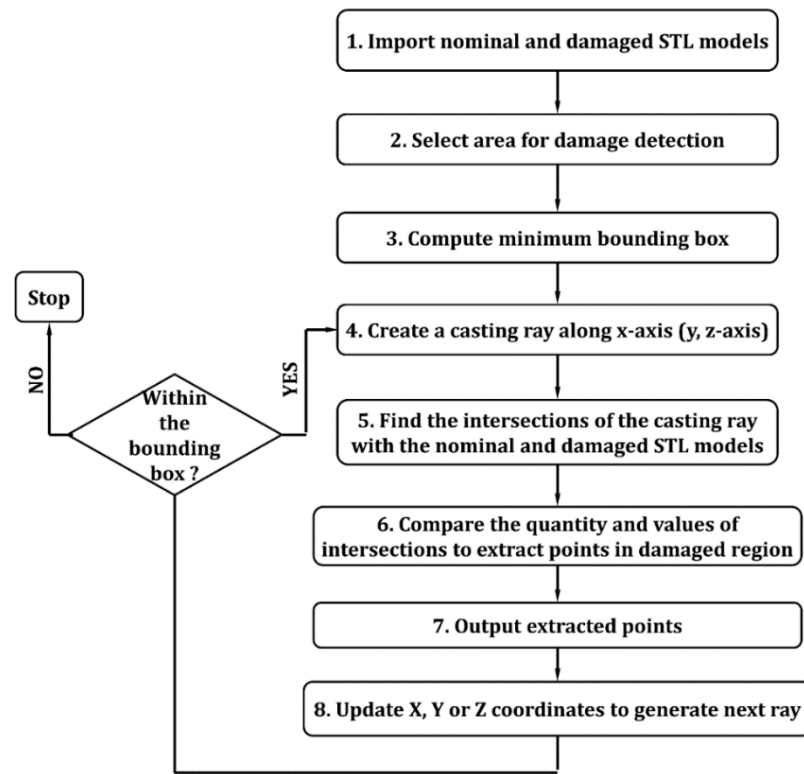


Figure 6. Flowchart of the damage reconstruction process from tri-dexel data

Based on the two scenarios, points enveloping the damaged region are extracted as follows: First, the quantity of the intersections of a ray with the nominal model and damaged model were compared. If the quantity was identical, coordinates of each point from the nominal model were compared with the coordinates of the point from the damaged model, e.g., $P(x_p, y_p, z_p)$ compared with $P'(x_{p'}, y_{p'}, z_{p'})$, $Q(x_q, y_q, z_q)$ compared with $Q'(x_{q'}, y_{q'}, z_{q'})$. Points with coordinates that beyond an acceptable tolerance were extracted, such as $Q(x_q, y_q, z_q)$ and $Q'(x_{q'}, y_{q'}, z_{q'})$. However, if the quantity of intersections is different and if there are no intersections of a ray with the damaged model (Figure 7c), the

intersections of the ray with the nominal model are extracted, such as $P(x_p, y_p, z_p)$ and $Q(x_q, y_q, z_q)$. If the quantity of intersections is different and there are intersections of the ray with the damaged model (Figure 7d), a set difference between the intersections from the nominal model and intersections from the damaged model is conducted. The set difference operation will extract the points that envelope the damage, such as $M(x_m, y_m, z_m)$ and $N(x_n, y_n, z_n)$.

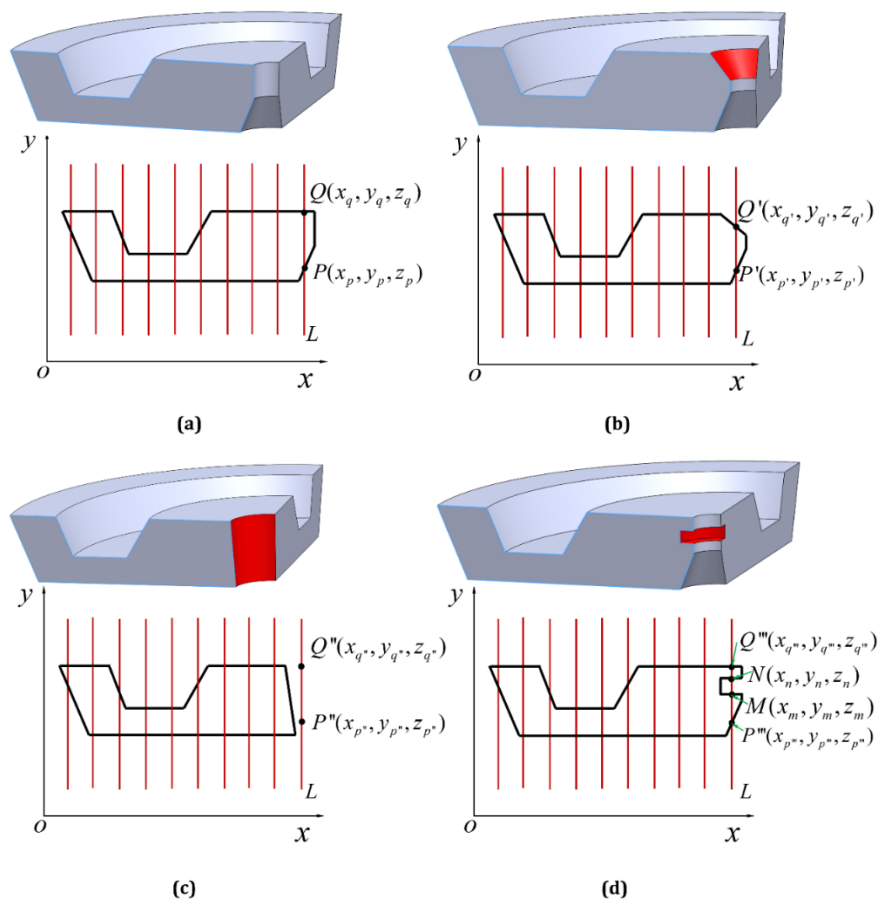


Figure 7. Damage extraction. (a) Intersections of casting rays with the nominal model; Intersections of casting rays with the damaged model with hole boundary fracture (b), inner hole penetrating fracture (c) and inner hole inside fracture (d)

Figure 8 depicts the damage reconstruction process using tri-dexel data for the die part. Figure 8a shows the selected area for damage extraction. The intersections of casting rays with the selected region of nominal and damaged models were shown in Figure 8b. The grid interval is 0.2 mm. The points that enveloping damaged zone were extracted as shown in Figure 8c. The STL model of the damage was reconstructed using the Screened Poisson Surface Reconstruction with reconstruction depth of 10 (Figure 8d) [36].

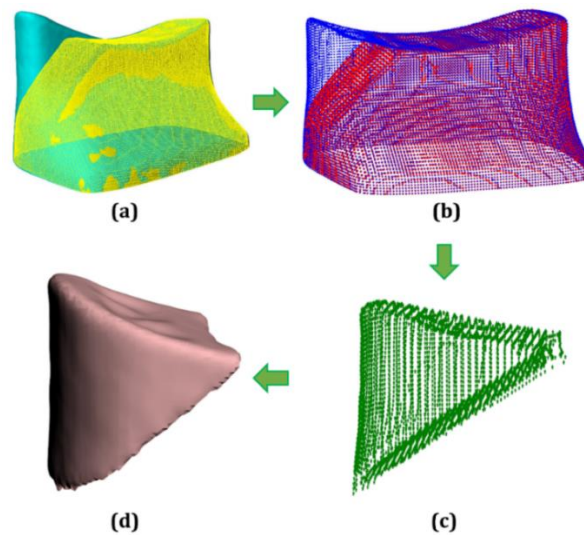


Figure 8. Damage reconstruction for a fractured die. (a) Selected area for damage extraction; (b) Intersections of casting rays with selected area of nominal and damaged models; (c) Extracted points; (d) STL model of the damage

3. REPAIR EXPERIMENTS AND RESULTS

3.1. EXPERIMENTAL SETUP AND MATERIAL PREPARATION

In this study, the laser-aided DED process was conducted using a maximum 1 kW fiber laser from IPG Photonics, a commercial powder feeder from Bay State Surface

Technologies, argon gas delivery unit, a designed off-axis powder feeding tube, and 3-axis motion table. Argon was also used to avoid deposits from oxidation.

The material of the die is AISI H13 tool steel. To improve the corrosion and abrasive resistance of the repaired sample, Co-based alloy Wallex 40 from Wall Colmonoy Limited was selected as the filler material. SEM micrograph and particle size distribution of Wallex 40 powder are depicted in Figure 9. The average particle diameter was 71 μm . The chemical composition of Wallex 40 and H13 tool steel is listed in Table 1.

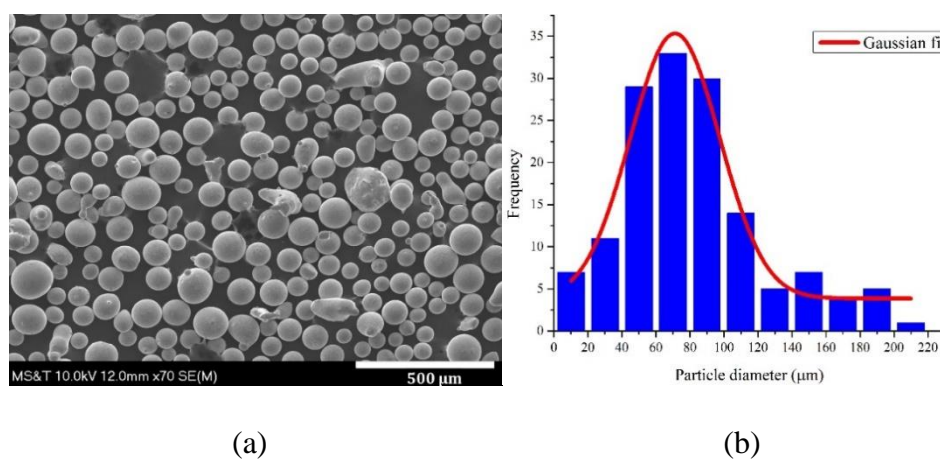


Figure 9. (a) SEM micrograph (a) and particle size distribution (b) of Wallex 40 powder

Table 1. Chemical composition of the target materials (wt.%)

Materials	C	Mn	Si	Cr	Ni	Mo	V	W	B	Fe	Co
H13 tool steel	0.4	0.4	1.0	5.25	-	1.35	1.0	-	-	Bal.	-
Wallex 40	0.6	-	1.9	16.2	23.5	-	-	7.6	2.0	1.3	Bal.

3.2. REPAIR RESULTS

The reconstructed damage as shown in Figure 10a was sliced into 10 layers with a layer thickness of 0.5 mm. Then raster deposition tool path was generated as shown in Figure 10b. Repair experiment was conducted according to the processing parameters listed in Table 2. Images of the repaired die are shown in Figure 10c.

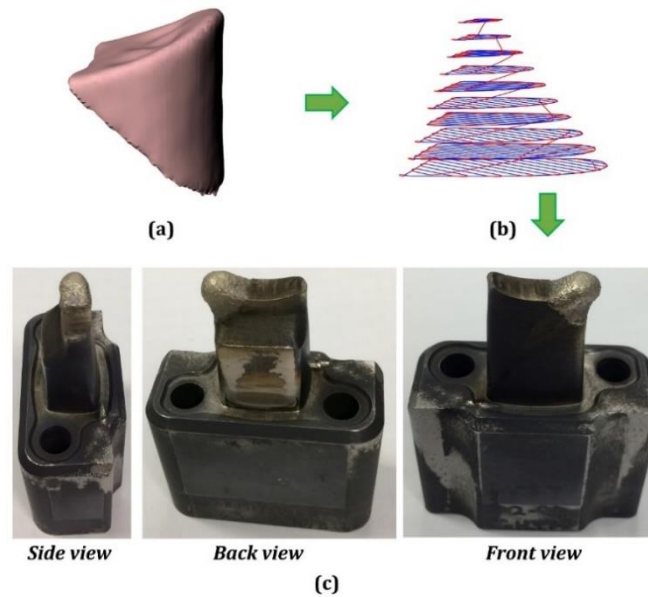


Figure 10. Tool path generation and repair result. (a) Reconstructed STL model of the damage; (b) Deposition tool path; (c) Die after material deposition

Table 2. Laser-aided DED processing parameters

Laser powder (W)	Scan speed (mm/min)	Powder feed rate (g/min)	Layer thickness (mm)	Track overlap
600	220	4	0.5	0.5

4. ACCURACY OF DAMAGE RECONSTRUCTION

High accuracy of the reconstructed damage is critical to assure a successful repair. Only the reconstructed damage is precise enough can the missing geometry be accurately restored. To evaluate the accuracy level of reconstructed damage from the tri-dexel data, a bracket model was designed in SolidWorks and output as the STL model (Figure 11a). Damage was created on the bracket model to obtain a damaged model as shown in Figure 11b. Because the bracket was designed in CAD software, the damaged geometry can be precisely obtained as shown in Figure 11c.

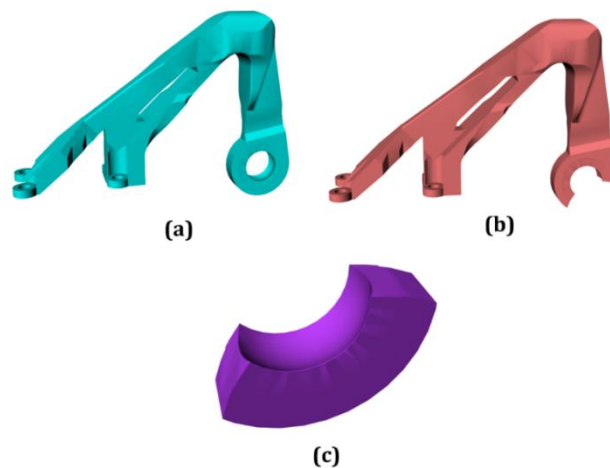


Figure 11. (a) A bracket nominal model; (b) Damaged model; (c) Defects

Intersections of casting rays with nominal and damaged models are shown in Figure 12a and 12b, respectively, where the grid interval δ is 1mm. Points in the damaged area were extracted and the STL model of the damaged geometry was reconstructed as shown

in Figure 12c-e, where grid interval $\delta = 1\text{ mm}$, $\delta = 0.5\text{ mm}$ and $\delta = 0.2\text{ mm}$, respectively. By visual inspection, it can be clearly seen that, by reducing the grid interval, the accuracy of the reconstructed damage is greatly enhanced. When $\delta = 1\text{ mm}$, the reconstructed damage is relatively coarse, and when $\delta = 0.2\text{ mm}$, the reconstructed damage is in a good correspondence to the real damage.

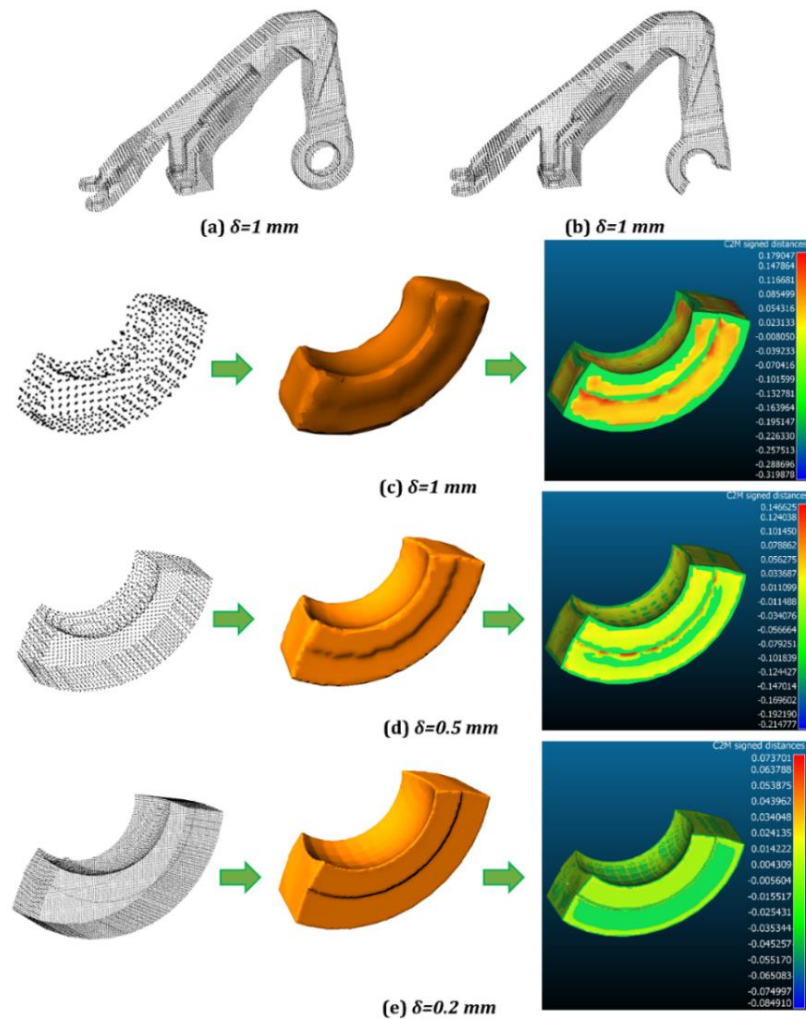


Figure 12. Accuracy analysis with different casting ray spacing. Intersections of casting rays with nominal (a) and damaged models (b). Comparison of reconstructed damage with real damage when $\delta = 1\text{ mm}$ (c), $\delta = 0.5\text{ mm}$ (d) and $\delta = 0.2\text{ mm}$ (e)

For investigating the accuracy, STL model of the damage in different grid interval values, $\delta = 1 \text{ mm}$, $\delta = 0.5 \text{ mm}$, $\delta = 0.2 \text{ mm}$, were compared with the real damage from CAD modeling. The signed distances were obtained and are shown in Figure 12c-e. The signed distance represents the shortest distance of a point to the nearest reference point. The reference point cloud here is the real damage points. Suppose the point cloud of real damage is set Ω . The points of damage reconstructed from tri-dexel is $P_d = (x_d, y_d, z_d)$. Then the signed distance function, f can be defined in Equation (1), where d denotes the distance of a point P_d to the nearest reference in the set Ω .

$$f(P_d) = \begin{cases} d(P_d, \Omega), & \text{if } P_d \in \Omega \\ -d(P_d, \Omega), & \text{if } P_d \notin \Omega \end{cases} \quad (1)$$

It can be seen that when $\delta = 1 \text{ mm}$, $\delta = 0.5 \text{ mm}$, $\delta = 0.2 \text{ mm}$, the error is $[-0.3199, 0.1790]$, $[-0.2148, 0.1466]$ and $[-0.0849, 0.0737]$ mm, respectively. One can see that when $\delta = 1 \text{ mm}$, the accuracy of the damage is low, which may result in poor repair quality. When $\delta = 0.2 \text{ mm}$, the reconstructed damage has a low level of error, which confirms that the reconstructed damage from tri-dexel data when $\delta = 0.2 \text{ mm}$ is sufficient to represent the real damage. Therefore, the grid interval in section 2.4 to reconstruct the damage of the die is chosen at 0.2 mm.

5. ILLUSTRATING EXAMPLES OF DAMAGE RECONSTRUCTION FROM TRI-DEXEL DATA

Two examples as shown in Figure 13 and Figure 14 were conducted to test the functionality and reliability of damage reconstruction from tri-dexel data. A defect was

created on a model as shown in Figure 13b. The damaged model was aligned with the nominal model (Figure 13d) and the damage was reconstructed as shown in Figure 13i.

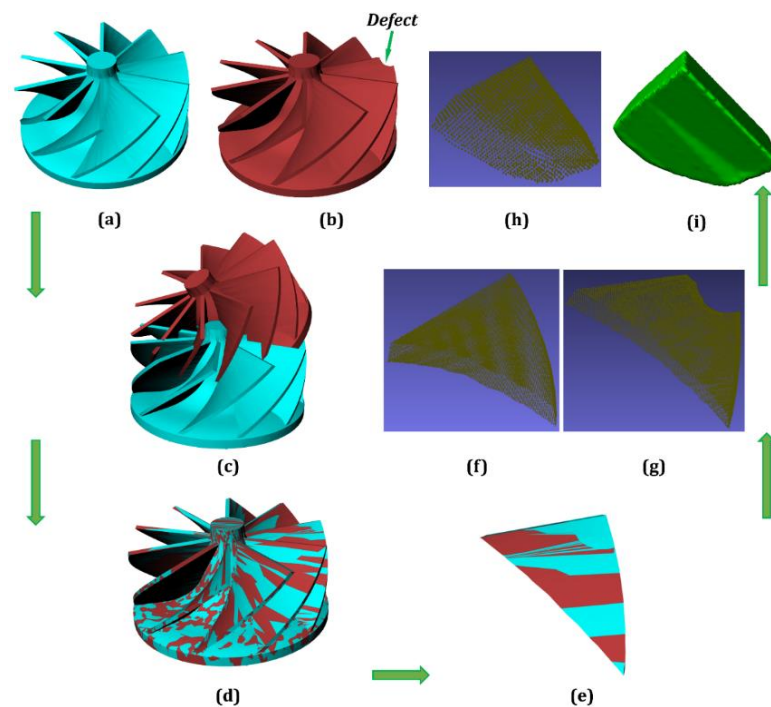


Figure 13. Damage reconstruction for a damaged turbine rotor. (a) Nominal CAD model; (b) Damaged CAD model; (c) Initial relative position of nominal and damaged STL models; (d) Aligned models; (e) Selected area for damage reconstruction; Intersections of casting rays with selected area of nominal (f) and damaged (g) models ($\delta=0.2$ mm); (h) Extracted damaged points; (i) Reconstructed STL model of the damage

Ball indentation defect was machined on the surface of an H13 tool steel die as shown in Figure 14a. After that, the damaged model was obtained through scanning and then aligned with the nominal model (Figure 14e). Tri-dexel method was applied to define the damaged geometry as shown in Figure 14h-i. Deposition tool path was generated by

slicing the damaged geometry into 5 layers and the part after deposition is shown in Figure 14k. The parameters for repairing the sample in Figure 14 are listed in Table 3.

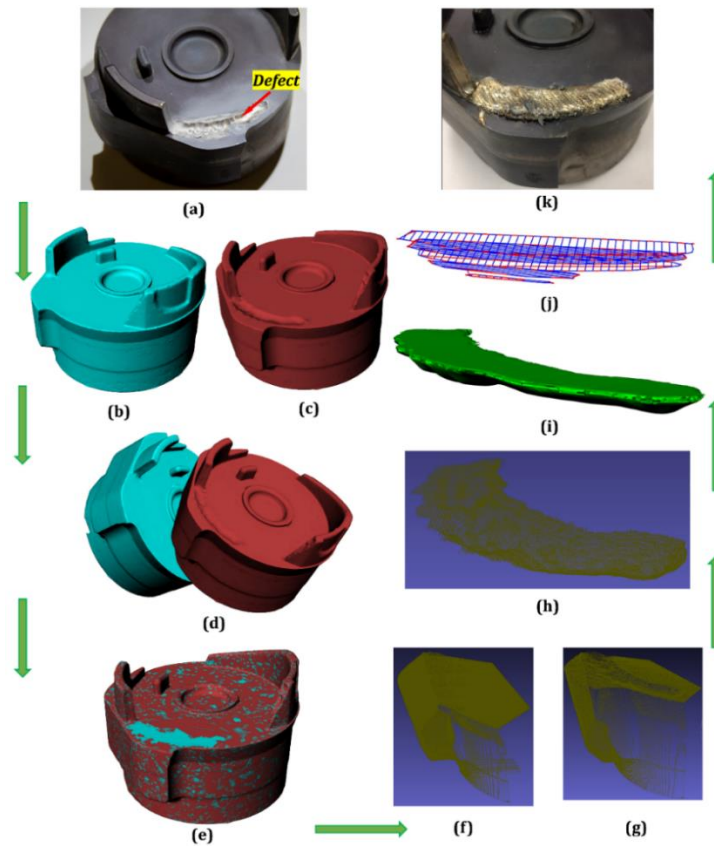


Figure 14. Damage reconstruction for a damaged die. (a) Damaged die; (b) Nominal model; (c) Damaged model; (d) Initial relative position of nominal and damaged models; (e) Aligned models; Intersections of casting rays with selected area of nominal (f) and damaged (g) models ($\delta=0.2$ mm); (h) Extracted damaged points; (i) Reconstructed STL model of the damage; (j) Deposition tool path; (k) Die after deposition

The CPU runtime for damage reconstruction for examples in Figures 8, 12, 13 and 14 are summarized in Table 4. The program was developed using Python and operated on

a personal computer with 2.50 GHz Intel Core i7 and 8GB memory. It can be found that the runtime for the scanned models (examples in Figure 8 and 14) is much higher than the runtime for the CAD model (examples in Figure 12 and 13). One can also notice that by reducing the grid interval δ , the CPU runtime increased significantly.

Table 3. DED processing parameters for the samples in Figure 14

Filler material	Laser power (W)	Scan speed (mm/min)	Powder flow rate (g/min)	Layer thickness (mm)
Inconel 625	500	230	3.74	0.5

Table 4. CPU runtime for damage reconstruction

Example	Figure 8	Figure 12	Figure 13	Figure 14
		2.9s when $\delta=1$		
CPU runtime	251.1s	8.8s when $\delta=0.5$	33.6	375.8s
		39.5s when $\delta=0.2$		

6. CONCLUSION

Reconstructing the damaged geometry is crucial for generating scanning tool path for material deposition. In the present research, tri-dexel method was employed to define the damage. Based on the investigation, some conclusions were summarized as follows:

(1) Models of damaged objects were recreated through a robot-aided 3D scanning process. A scanning routine was determined by scanning a designed part with general features. The integration of 6DOF industrial robot with 3D structured light scanner benefits the scanning process by eliminating the time-consuming process of manually turning the object to find appropriate angles to capture all surfaces.

(2) The reconstructed damaged model was aligned with the nominal model by aligning associated features (e.g., convex-hull centroids, cross-sections) via a transformation matrix. The least-squares method was utilized to converge to the transformation variables.

(3) The area covering the damaged zone was selected and tri-dexel method was used to extract point set in the damaged area by comparing intersections of casting rays with nominal and damaged models. STL model of the defective region was reconstructed through the extracted point cloud using Screened Poisson Surface Reconstruction algorithm.

(4) The reconstructed damage from tri-dexel data was compared with the actual damage generated from CAD modeling. The result shows by reducing the grid interval to 0.2 mm, the accuracy of reconstructed damage could reach up to ± 0.1 mm, which is sufficient for repair purpose. Further reducing the grid interval benefits the accuracy of the damage, but could significantly increase computing time, especially for scanned models with a large number of triangles.

(5) The reconstructed damage was sliced into layers to generate a deposition tool path. Repair experiments were conducted by depositing materials on the damaged area.

The damage reconstruction algorithm from tri-dexel data was evaluated in functionality and reliability by several illustrating examples.

ACKNOWLEDGMENTS

The support from NSF grants CMMI-1547042, CMMI-1625736, EEC-1004839, and Center for Energy Technology and Strategy, National Cheng Kung University, and National Chung-Shan Institute of Science & Technology are appreciated. We also appreciate the financial support provided by the ISC at Missouri S&T.

REFERENCES

- [1] X. Zhang, W. Li, X. Chen, W. Cui, and F. Liou, "Evaluation of Component Repair using Direct Metal Deposition from Scanned Data," *International Journal of Advanced Manufacturing Technology*, vol. 95, pp. 3335-3348, 2017.
- [2] H. D. Morgan, J. A. Cherry, S. Jonnalagadda, D. Ewing, and J. Sienz, "Part Orientation Optimisation for the Additive Layer Manufacture of Metal Components," *International Journal of Advanced Manufacturing Technology*, vol. 86, pp. 1679-1687, 2016.
- [3] X. Penaranda, S. Moralejo, A. Lamikiz, and J. Figueras, "An Adaptive Laser Cladding Methodology for Blade Tip Repair," *International Journal of Advanced Manufacturing Technology*, vol. 92, pp. 4337-4343, 2017.
- [4] C. G. Mançanares, E. de S. Zancul, J. da Silva, and P. A. Cauchick Miguel, "Additive Manufacturing Process Selection based on Parts' Selection Criteria," *International Journal of Advanced Manufacturing Technology*, vol. 80, pp. 1007-1014, 2015.
- [5] B. Baufeld, O. Van der Biest, and R. Gault, "Additive Manufacturing of Ti-6Al-4V Components by Shaped Metal Deposition: Microstructure and Mechanical Properties," *Materials & Design*, vol. 31, pp. S106-S111, 2010.

- [6] B. Dutta and F. H. (Sam) Froes, "The Additive Manufacturing (AM) of Titanium Alloys," *Metal Powder Report*, vol. 72, pp. 96-106, 2017.
- [7] G. P. Dinda, A. K. Dasgupta, and J. Mazumder, "Laser Aided Direct Metal Deposition of Inconel 625 Superalloy: Microstructural Evolution and Thermal Stability," *Materials Science and Engineering: A*, vol. 509, pp. 98-104, 2009.
- [8] Q. Jia and D. Gu, "Selective Laser Melting Additive Manufacturing of Inconel 718 Superalloy Parts: Densification, Microstructure and Properties," *Journal of Alloys and Compounds*, vol. 585, pp. 713-721, 2014.
- [9] W. C. Lin and C. Chen, "Characteristics of Thin Surface Layers of Cobalt-based Alloys Deposited by Laser Cladding," *Surface and Coatings Technology*, vol. 200, pp. 4557-4563, 2006.
- [10] M. K. Imran, S. H. Masood, M. Brandt, S. Bhattacharya, and J. Mazumder, "Direct Metal Deposition (DMD) of H13 Tool Steel on Copper Alloy Substrate: Evaluation of Mechanical Properties," *Materials Science and Engineering: A*, vol. 528, pp. 3342-3349, 2011.
- [11] S. Bhattacharya, G. P. Dinda, A. K. Dasgupta, and J. Mazumder, "Microstructural Evolution of AISI 4340 Steel During Direct Metal Deposition process," *Materials Science and Engineering: A*, vol. 528, pp. 2309-2318, 2011.
- [12] W. Li, X. Chen, L. Yan, J. Zhang, X. Zhang, and F. Liou, "Additive Manufacturing of a New Fe-Cr-Ni Alloy with Gradually Changing Compositions with Elemental Powder Mixes and Thermodynamic Calculation," *International Journal of Advanced Manufacturing Technology*, vol. 95, pp. 1013-1023, 2017.
- [13] S. Kumar, V. Sharma, A. K. S. Choudhary, S. Chattopadhyaya, and S. Hloch, "Determination of Layer Thickness in Direct Metal Deposition using Dimensional Analysis," *International Journal of Advanced Manufacturing Technology*, vol. 67, pp. 2681-2687, 2013.
- [14] N. Shamsaei, A. Yadollahi, L. Bian, and S. M. Thompson, "An Overview of Direct Laser Deposition for Additive Manufacturing; Part II: Mechanical Behavior, Process Parameter Optimization and Control," *Additive Manufacturing*, vol. 8, pp. 12-35, 2015.
- [15] Z. Wang, K. Guan, M. Gao, X. Li, X. Chen, and X. Zeng, "The Microstructure and Mechanical Properties of Deposited-IN718 by Selective Laser Melting," *Journal of Alloys and Compounds*, vol. 513, pp. 518-523, 2012.
- [16] J. Bennett, R. Dudas, J. Cao, K. Ehmann, and G. Hyatt, "Control of Heating and Cooling for Direct Laser Deposition Repair of Cast Iron Components," *International Symposium on Flexible Automation, OH, USA*, pp. 229-236, 2016.

- [17] A. J. Pinkerton, W. Wang, and L. Li, "Component Repair using Laser Direct Metal Deposition," *Proceedings of the Institution of Mechanical Engineers, Part B: Journal of Engineering Manufacture*, vol. 222, pp. 827-836, 2008.
- [18] Q. Liu, Y. Wang, H. Zheng, K. Tang, H. Li, and S. Gong, "TC17 Titanium Alloy Laser Melting Deposition Repair Process and Properties," *Optics & Laser Technology*, vol. 82, pp. 1-9, 2016.
- [19] L. Song, G. Zeng, H. Xiao, X. Xiao, and S. Li, "Repair of 304 Stainless Steel by Laser Cladding with 316L Stainless Steel Powders followed by Laser Surface Alloying with WC Powders," *Journal of Manufacturing Processes*, vol. 24, pp. 116-124, 2016.
- [20] J. Song, Q. Deng, C. Chen, D. Hu, and Y. Li, "Rebuilding of Metal Components with Laser Cladding Forming," *Applied Surface Science*, vol. 252, pp. 7934-7940, 2006.
- [21] J. Gao, X. Chen, O. Yilmaz, and N. Gindy, "An Integrated Adaptive Repair Solution for Complex Aerospace Components through Geometry Reconstruction," *International Journal of Advanced Manufacturing Technology*, vol. 36, pp. 1170-1179, 2008.
- [22] J. M. Wilson, C. Piya, Y. C. Shin, F. Zhao, and K. Ramani, "Remanufacturing of Turbine Blades by Laser Direct Deposition with its Energy and Environmental Impact Analysis," *Journal of Cleaner Production*, vol. 80, pp. 170-178, 2014.
- [23] J. Zheng, Z. Li, and X. Chen, "Worn Area Modeling for Automating the Repair of Turbine Blades," *International Journal of Advanced Manufacturing Technology*, vol. 29, pp. 1062-1067, Jul. 2006.
- [24] P. Hong-Seok and T. U. Mani, "Development of an Inspection System for Defect Detection in Pressed Parts Using Laser Scanned Data," *Procedia Engineering*, vol. 69, pp. 931-936, 2014.
- [25] J. He, L. Li, and J. Li, "Research of Key-Technique on Automatic Repair System of Plane Blade Welding," *International Conference on Control, Automation and Systems Engineering*, Singapore, pp. 1-4, 2011.
- [26] X. Zhang, W. Li, and F. Liou, "Damage Detection and Reconstruction Algorithm in Repairing Compressor Blade by Direct Metal Deposition," *International Journal of Advanced Manufacturing Technology*, vol. 95, pp. 2393-2404, 2018.
- [27] T. Van Hook, "Real-time Shaded NC Milling Display," *Proceedings of the 13th Annual Conference on Computer Graphics and Interactive Techniques*, NY, USA, pp. 15-20, 1986.

- [28] Y. Ren, S. K. Lai-Yuen, and Y.-S. Lee, "Virtual Prototyping and Manufacturing Planning by using Tri-Dexel Models and Haptic Force Feedback," *Virtual and Physical Prototyping*, vol. 1, pp. 3-18, 2006.
- [29] X. Peng and W. Zhang, "A Virtual Sculpting System Based on Triple Dexel Models with Haptics," *Computer-Aided Design and Applications*, vol. 6, pp. 645-659, 2009.
- [30] M. C. Leu, X. Peng, and W. Zhang, "Surface Reconstruction for Interactive Modeling of Freeform Solids by Virtual Sculpting," *CIRP Annals*, vol. 54, pp. 131-134, 2005.
- [31] W. Zhu and Y.-S. Lee, "Dexel-Based Force-Torque Rendering and Volume Updating for 5-DOF Haptic Product Prototyping and Virtual Sculpting," *Computers in Industry*, vol. 55, pp. 125-145, 2004.
- [32] X. Gao, S. Zhang, and Z. Hou, "Three Direction Dexel Model of Polyhedrons and Its Application," *International Conference on Natural Computation (ICNC 2007)*, Haikou, China, vol. 5, pp. 145-149, 2007.
- [33] S. He, X. Zeng, C. Yan, H. Gong, and C.-H. Lee, "Tri-Dexel Model Based Geometric Simulation of Multi-axis Additive Manufacturing," *Intelligent Robotics and Applications: 10th International Conference, ICIRA 2017*, Wuhan, China, pp. 819-830, 2017.
- [34] S. H. Choi and A. M. M. Chan, "A Virtual Prototyping System for Rapid Product Development," *Computer-Aided Design*, vol. 36, pp. 401-412, 2004.
- [35] R. Liu, Z. Wang, and F. Liou, "Multifeature-Fitting and Shape-Adaption Algorithm for Component Repair," *Journal of Manufacturing Science and Engineering*, vol. 140, pp. 21003-21019, 2017.
- [36] M. Kazhdan and H. Hoppe, "Screened Poisson Surface Reconstruction," *ACM Transactions on Graphics*, vol. 32, pp. 29:1-29:13, 2013.

V. EVALUATION OF COMPONENT REPAIR USING DIRECT METAL DEPOSITION FROM SCANNED DATA

Xinchang Zhang¹, Wei Li¹, Xueyang Chen¹, Wenyuan Cui¹, and Frank Liou¹

¹Department of Mechanical and Aerospace Engineering,

Missouri University of Science and Technology, Rolla, MO 65409, USA

ABSTRACT

In this work, the repair volume of AISI H13 tool steel samples with hemisphere-shaped defects was reconstructed through reverse engineering and the samples were repaired by laser-aided direct metal deposition (DMD) using cobalt-based alloys powder as the filler material. Microstructure characterization and elemental distribution of deposits were analyzed using an optical microscope (OM), scanning electron microscope (SEM), and energy dispersive spectrometry (EDS). Mechanical properties of repaired samples were evaluated via tensile testing and microhardness measurement. The experiment showed that a gap between deposits and substrate exists if only employing the tool path generated from the reconstructed repair volume but the gap can be removed by depositing an extra layer covering that region. Microstructure and the tensile testing confirmed a strong metallurgical bond in the interface. Defect-free columnar structure dominated the deposits near the interface while other regions of deposits consisted of a dendrite structure with interdendritic eutectics. The tensile test showed the repaired samples have a higher ultimate tensile strength (UTS) and lower ductility compared with those of base metal. Fractography from tensile test showed repaired samples fractured brittly at the deposits

section with cracking propagating along the grain boundaries. The hardness measurement showed the as-deposited layers have a much higher hardness in comparison to that of the substrate.

Keywords: Direct Metal Deposition; Repair; Reverse Engineering; Additive Manufacturing; Tool Steel

1. INTRODUCTION

Laser-aided direct metal deposition (DMD) is an additive manufacturing (AM) process that can build fully-dense complex parts according to their 3D models layer by layer following a user-defined tool path [1]. The process requires using a high-power laser to create a molten pool by melting substrate surfaces and filler metal particles that delivered into the molten zone (Figure 1). The adding material solidifies to form a layer of the part to be fabricated, forming a good bond between two materials [2, 3]. The DMD process has shown great applications in the fields of near-net-shape part fabrication [4-6] and surface coating [7-9] to enhance hardness, wear, and corrosion resistance. For H13 tool steel that broadly used to fabricate die, mold, and cutting tools, reinforcing surfaces to withstand wear and corrosion is always desired. Generally, hard surfacing alloys can be cladded on tool steel to enhance wear and corrosion resistance or tool steel matrix can be reinforced by hard phases such as WC or TiC. Huang et al. successfully clad WC/Ni layers on H13 steel substrate with fully dense and crack-free [10]. The result reveals that the wear resistance of H13 steel was greatly enhanced. Almagour et al. reinforced H13 steel by mixing H13 powder with TiC [11] and TiB₂ powder [12] fabricated by selective laser

melting. Both nanocomposites show higher hardness and much lower wear rate than pure H13 steel counterpart. An optimal concentration of TiC in TiC/H13 steel composite can also benefit its erosion resistance [13].

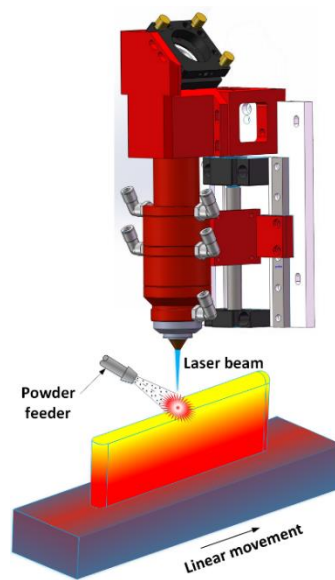


Figure 1. Schematic diagram of the laser-aided direct metal deposition process

Another application of the DMD process is in component repair [14, 15], where filler materials are conveyed into damaged region of a worn part to restore the missing geometry. DMD process for component repair has been studied in diverse aspects. In repair capability, Pinkerton et al. machined varied shapes of grooves and slots on H13 tool steel substrates and then refilled with H13 powder [16]. High-quality repaired parts were fabricated, except near boundaries where the defect's edge is too steep. Childs et al. revealed that porosities of AM-fabricated steel are strongly affected by carbon content:

high content of carbon in H13 steel contributes to the poor wettability and low density [17]. Graf et al. prepared varied groove-shaped defects on stainless steel and Ti-6Al-4V substrates and then tried to repair those missing volumes by modifying process parameters [18]. Defects on Ti-6Al-4V substrate were also created and subsequently refilled with Ti-6Al-4V powder by Paydas et al [19]. It needs to clarify that the repair volume in the aforementioned studies was very simple and thus able to be defined manually. However, damage with complex and irregular shapes is difficult to define manually. In addition, operator's experience-based damage reconstruction cannot guarantee consistent and repeatable repair quality, and thus dramatically increase the risk of failure during service.

In the aspect of repair automation, many studies were focused on the repair of aero-engine blades. An adaptive tool path generation method was proposed to repair turbine airfoils by Qi et al. [20] through varying laser beam diameter and laser power. Gao et al. provided a geometry reconstruction algorithm by comparing the 3D-scanned damaged model with the nominal model [21]. Wilson et al. utilized the fracture surface on the damaged model to cut the nominal model to restore the missing volume [22]. A stereo camera was used to detect damaged region on a Ti-6Al-4V aircraft part and then a laser displacement sensor was used to scan the damaged geometry in [23]. This process limits fast repair due to inefficient scanning numerous points on damaged surfaces. Developing a high-efficient damage reconstruction strategy by assuring sound deposits is urgently needed in modern repair workshops.

Reconstructing repair volume of worn components is the key to provide a laser scanning tool path for material deposition. In the current research, hemispherical-shaped defects were machined on H13 tool steel substrates. The repair volume on substrates was

obtained by scanning damaged substrates using a structured-light 3D scanner. Then the repair volume was sliced into several layers to generate a smooth raster deposition tool path. The algorithm for generating the raster path is detailly discussed. Excellent wear and corrosion resistant cobalt-based alloy were deposited in the damaged area as a coating to ensure that the repaired parts will have a longer service life. Analysis such as microstructure characterization, tensile behavior, hardness measurement, and EDS quantification was performed on the repair samples to assess repair quality through the proposed methodology.

2. 3D SCANNING AND TOOL PATH GENERATION

H13 tool steel was selected as substrate due to the widespread application of such material in manufacturing molds, dies, and tools. The primary microstructure of this commercial steel is α -Fe martensite phase [24]. In order to perform repair, a 15-mm diameter ball end mill generated defects were created on the top surface of the substrate to a depth of 3 mm as shown in Figure 2. Three indexing points were marked on the surface of each substrate to define the position of the substrate with tool path in repair experiment.

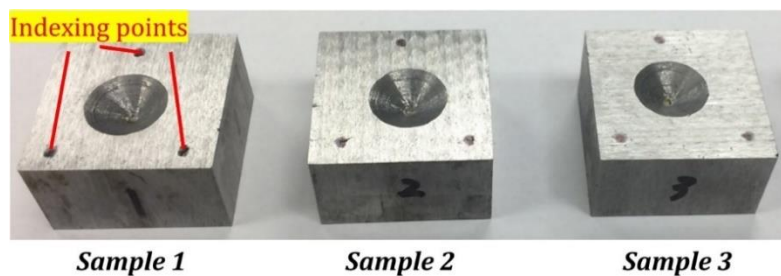


Figure 2. H13 tool steel substrates with hemispherical-shaped defects

It can be found in Figure 2 that the repair volume of the damaged substrate was enveloped by the fracture surface and a missing top surface. Therefore, the repair volume can be obtained by scanning the fracture surface and then processed to generate a tool path. The process from scanning to tool path generation is illustrated in Figure 3.

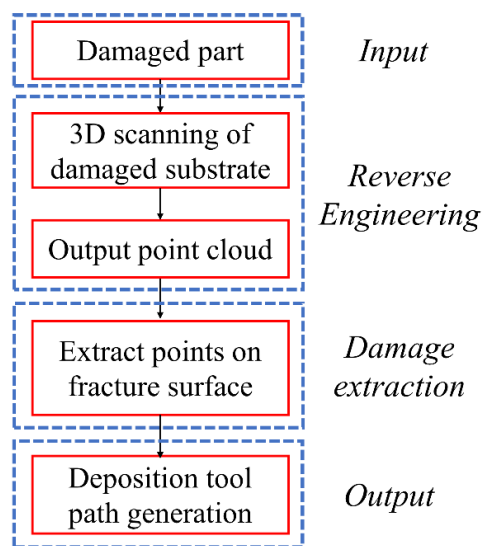
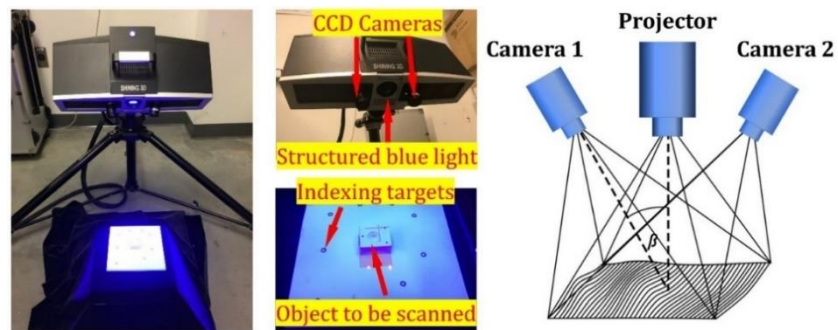


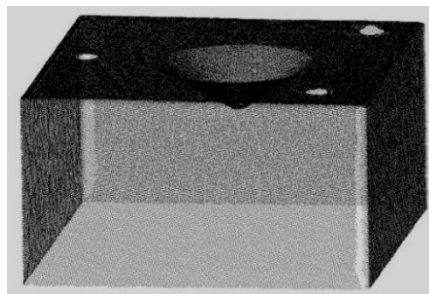
Figure 3. Flowchart of scanning to tool path generation

The scanning setup was shown in Figure 4a. The damaged substrate was scanned using a high accuracy structured light metrology 3D scanner (OptimScan 5M from Shining 3D Tech. Co. Ltd.). Structured light scanners project a narrow pattern of parallel stripes onto a three-dimensional object and convert the distortions into 3D coordinates of a point cloud. After calibration, a 6.5 mm ceramic gage block was at first scanned for six repetitions to test scanning accuracy, which was found to be 30 μm . The point cloud of the

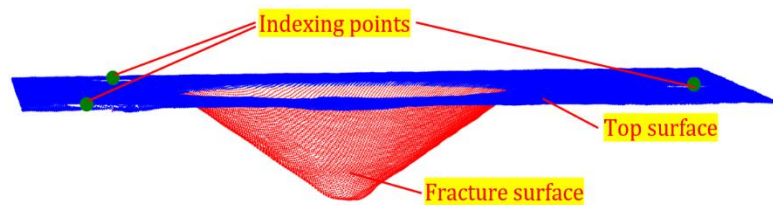
substrate was obtained as shown in Figure 4b. A Python program was developed to detect point cloud on the fracture surface and indexing dots on the upper surface based on distance to the top surface. Points on the damaged surface and indexing dots were extracted as shown in Figure 4c.



(a)



(b)



(c)

Figure 4. (a) 3D scanning setup; (b) Scanned point cloud; (c) Damage extraction

Toolpath that laser travels for material building up significantly affect the shape and mechanical properties of deposits [25]. Poor tool path planning may create gas pores, high residual stresses, and distortion on deposits. In general, outline contour with zigzag infill pattern shown in Figure 5a is widely adopted. Laser scans along the outline contour and then along a zigzag pattern to acquire fully dense deposits. Rapid interpolation was traditionally inserted between two adjacent routes such as P_j and P_{j+1} in Figure 5a. The laser will inevitably undergo acceleration and deceleration in such connections. Velocity fluctuation may result in unstable powder catch efficiency, causing distortion of deposits. To address this issue, a tool path with deposition route and continuous transitional route with laser powered-off was designed in this paper. As shown in Figure 5b, the laser moves from point P_j to P_{j+1} , where a transitional route $F(t)$ was inserted in between. The direction vectors of P_j and P_{j+1} are \vec{m} and \vec{n} , respectively. The equation of $F(t)$ can be obtained in Equation (1), where $t \in \left[0, \frac{\pi}{2}\right]$ and R is a user-defined variable to control the magnitude of the transitional route.

$$F(t) = P_j + \sin(t)R\vec{m} + [1 - \cos(t)]R\vec{n} + \frac{1 - \cos(2t)}{2}(P_{j+1} - P_j - R\vec{m} - R\vec{n}) \quad (1)$$

The extracted points on fracture surface were sliced into 6 layers with a layer thickness of 0.5 mm to generate a tool path as shown in Figure 5c. This tool path was utilized to repair substrate 1 in Figure 2. For substrate 2 and 3, besides of repair path in Figure 5c, a contour and rectangular finishing path were performed, respectively, as shown in Figure 5d and 5e. Laser travels along the boundary of damage for circular finishing path and along a bi-directional pattern for the rectangular path.

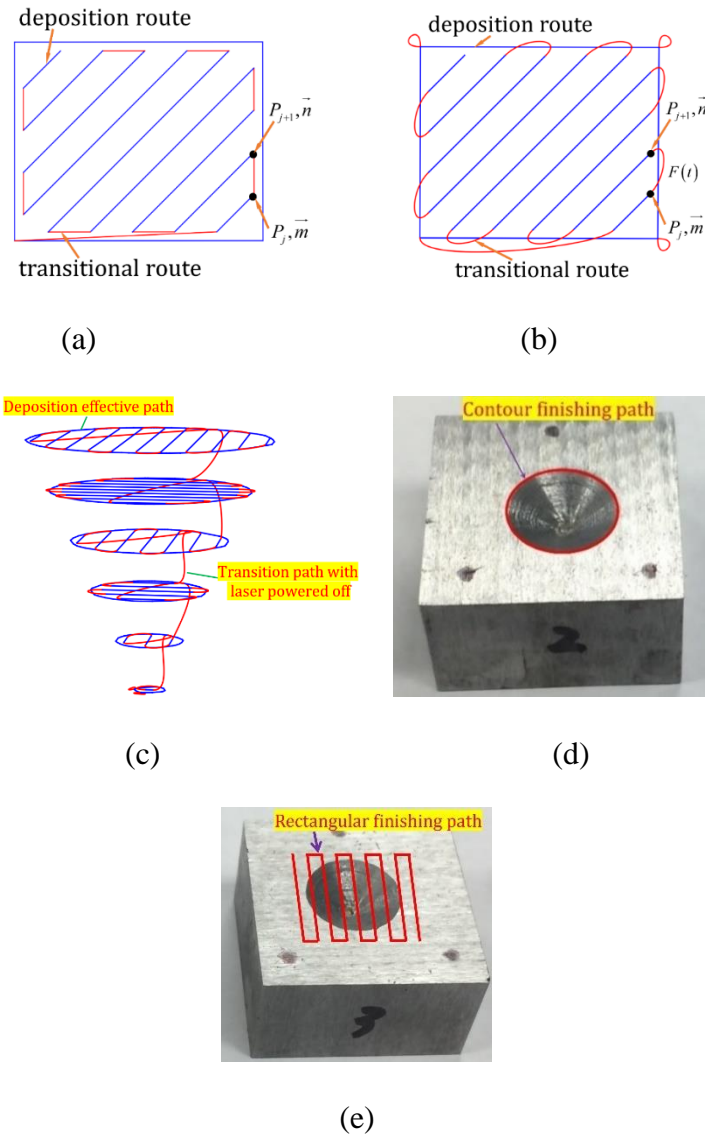


Figure 5. (a) Uncontinuous deposition pattern; (b) Continuous deposition pattern; (c) Repair tool path; Circular (d) and rectangular (e) finishing path

3. EXPERIMENT PROCEDURE

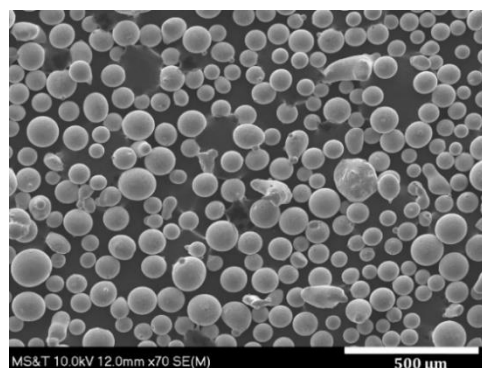
3.1. MATERIALS AND PREPARATION

The filler material was cobalt-based hard surfacing alloys Wallex 40 supplied by Wall Colmonoy Co. Since the damage is superficial, depositing Wallex 40 on tool steel act

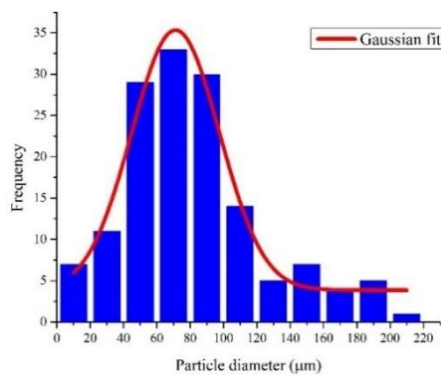
as coatings to enhance corrosive and abrasion resistance to assure longer service time. The chemical compositions of H13 tool steel and Wallex 40 are given in Table 1.

Table 1. Chemical composition of the target materials (wt.%)

Materials	C	Mn	Si	Cr	Ni	Mo	V	W	B	Fe	Co
H13 tool steel	0.4	0.4	1.0	5.25	-	1.35	1.0	-	-	Bal.	-
Wallex 40	0.6	-	1.9	16.2	23.5	-	-	7.6	2.0	1.3	Bal.



(a)



(b)

Figure 6. SEM micrograph (a) and particle size distribution (b) of Wallex 40 powder

Wallex 40 powder was characterized to analyze particle shape and size distribution. The SEM micrograph of Wallex 40 was presented in Figure 6a. One can see that most

particles exhibit spherical morphology although some irregular shaped powders were observed. Particle size distribution analyzed using ImageJ was depicted in Figure 6b and the average particle diameter was 71 μm .

3.2. EXPERIMENTAL SETUP

The DMD system (Figure 7) consists of a laser, powder feeder, 3-axis work table, and a gas feeding unit. A continuous wave (CW) fiber laser with a peak power of 1000 W from IPG Photonics Corporation was adopted as the laser generator to emit a tilted laser beam with 1.8 mm diameter. A blown powder feeder (Model 1200 from Bay State Surface Technologies, Inc.) was utilized to convey metal particles to melt pool through a vertical ceramic powder feed nozzle with the aid of Argon gas. The process was performed in the Argon gas atmosphere for preventing materials from oxidization. The damaged area was cleaned with acetone prior to repair. One complete laser preheating process with a constant power of 300 W was performed without delivering powder. This preheating process can melt a tiny thickness of material on the substrate to smooth the surface and remove surface impurities. This process also helps to prevent cracking on deposits during rapid heating and cooling cycles when depositing cobalt-based alloys as the cracking resistance of such alloys is low [26, 27].

Three repair experiments (Namely, repair 1, 2 and 3, repair 1 stands for repairing sample 1 in Figure 2) were performed. For repair 1, tool path (Figure 5c) generated directly from the repair volume was used. For repair 2, an extra layer obtained by measuring the defect's edge was performed (Figure 5d). This contour tool path overlays the defect's

boundary. For repair 3, a rectangular tool path which covers the defective region was conducted (Figure 5e). The processing parameters were listed in Table 2.

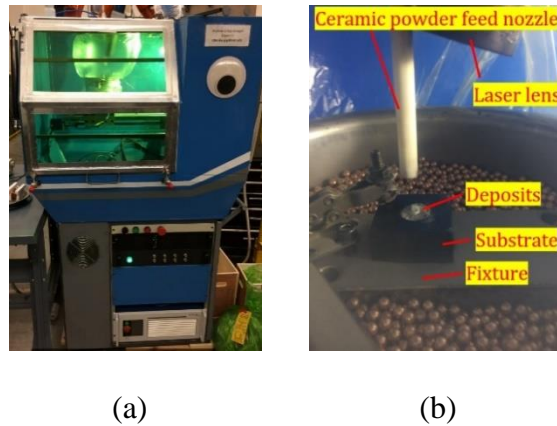


Figure 7. DMD equipment to perform repair experiment

Table 2. Processing parameters for repair experiment

Experiment	Laser power (W)	Powder flow rate (g/min)	Scan speed (mm/min)	Toolpath
Pre-heating	300	0	200	Raster (Figure 2.4c)
Repair 1	600	2.8	200	Raster (Figure 2.4c)
Repair 2	600	2.8	200	Raster (Figure 2.4c) + Circular (Figure 2.4d)
Repair 3	600	2.8	200	Raster (Figure 2.4c) + Rectangular (Figure 2.4e)

3.3. SAMPLE PREPARATION AND MATERIAL CHARACTERIZATIONS

Repaired samples were sectioned using EDM to slices with a thickness of 1.3 mm as shown in Figure 8a. Cross-sections of samples were analyzed using the HIRO KH-8700 digital optical microscope. Tensile specimens were machined from the substrate using EDM according to dimensions in Figure 8b. The position and orientation of the tensile sample over substrate were shown in Figure 8a. Tensile specimens were cut so that the interface between deposits and substrate was located approximated in the middle of the tensile sample, i.e., half of the specimen was deposits and another half was the substrate. In order to remove scratches and defects during machining using EDM, all specimens were ground using 320, 600 and 800 grid abrasive papers to a thickness of 1 mm. Tensile specimens were tested using Instron universal tester with a crosshead speed of 0.015 mm/min. Tensile stress-strain curves were obtained.

Fractured tensile specimens were mounted and the longitudinal surface was ground and finally polished using 0.05 microns silica suspension. The polished surface was etched using nitric acid and hydrochloric acid with a volume ratio of 1:1 to reveal microstructure morphology.

Tensile fracture surface in longitudinal and transverse sections was examined using FEI Helios Nanolab 600 Scanning Electron Microscope with an Oxford Energy Dispersive Spectrometer system. EDS mapping and line scan were conducted from the substrate to deposits. EDS mapping was also performed on deposits to analyze elemental distribution. Vickers hardness was measured using a Struers Duramin microhardness tester with a press load of 9.81 N and loading time of 10s. Three measurements were conducted at the same height.

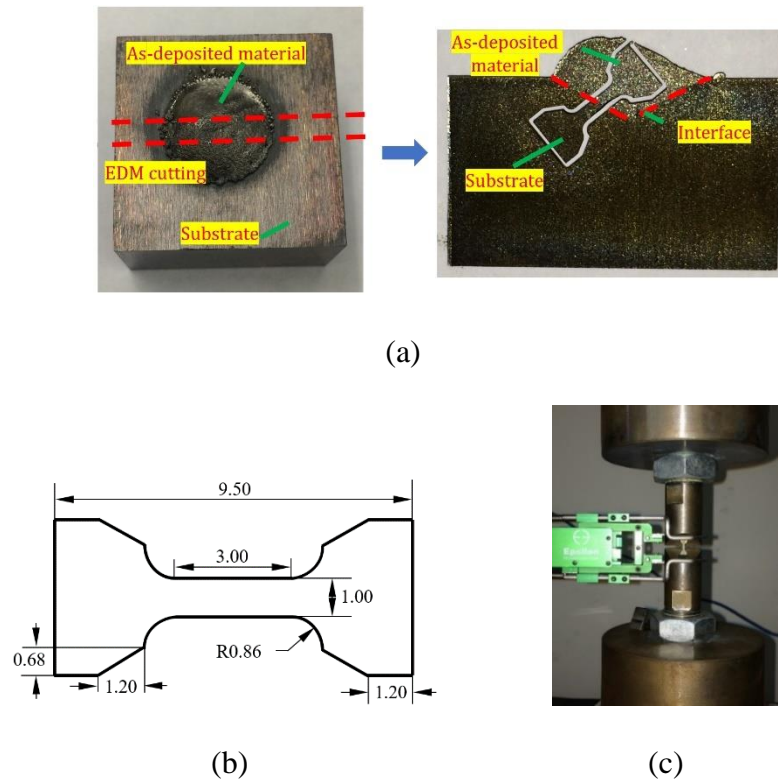


Figure 8. Tensile test specimen preparation. (a) Obtained tensile specimen over a sectioned substrate; (b) Dimensions of the mini-tensile specimen (Dimensions in mm, 1 mm in thickness); (c) Tensile test setup

4. RESULTS AND DISCUSSION

4.1. MACRO EXAMINATION OF REPAIRED SAMPLES

Overview of the repaired substrates was shown in Figure 9. The figures show mountain-shaped deposits where the center of deposits was extruded. This can be attributed to the entrapped over-delivered powder in the damaged area during deposition. Power delivered to the damaged region cannot be melted entirely. Therefore, some particles were left in the damaged area and because of the V-shape of the damage, those powders cannot

be blown away completely by Argon delivery gas. Therefore, those particles were accumulated, re-melted and solidified, resulting in the mountain-shaped deposits.

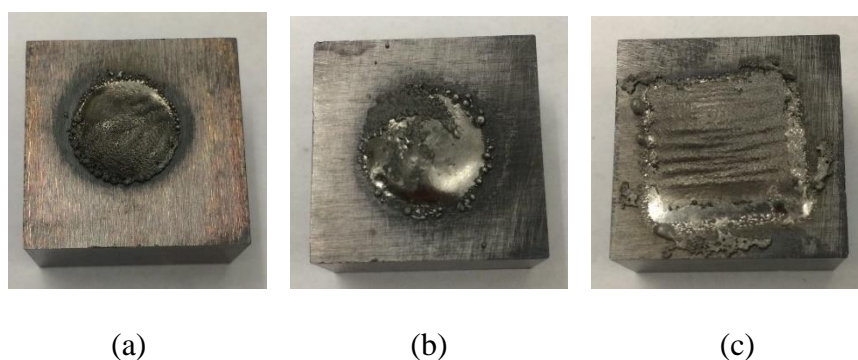


Figure 9. Repaired substrates from (a) repair 1, (b) repair 2, and (c) repair 3

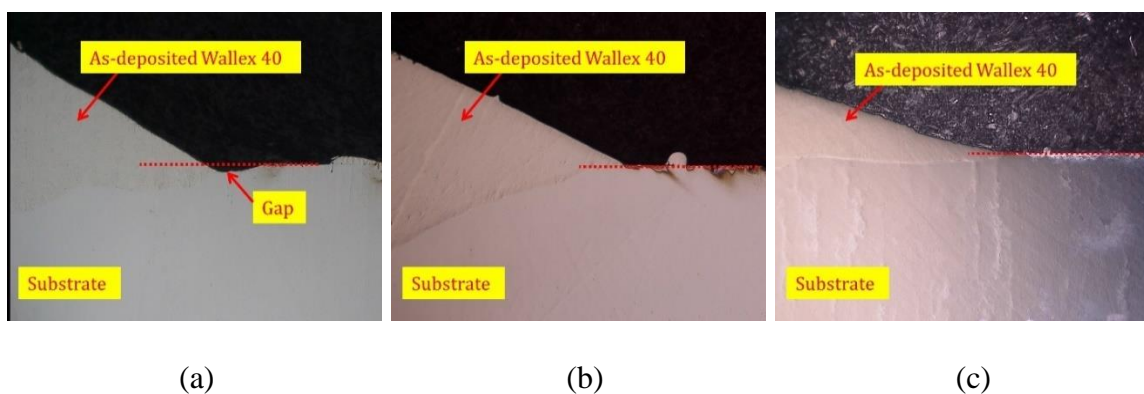


Figure 10. Optical images of cross-sections of repaired substrates from (a) repair 1, (b) repair 2, and (c) repair 3

Optical micrographs of the cross-section of samples were presented in Figure 10. One can see from Figure 10a is that, although adequate materials were deposited, a gap

between deposits and substrate along the boundary was found. The gap was produced because the laser beam cannot completely envelop the boundary, thus unable to melt material in such area. The gap can be effectively removed by depositing an extra layer along the boundary (Figure 10b) or by depositing an additional layer that completely covers the damage (Figure 10c). This overhang eliminates the gap successfully.

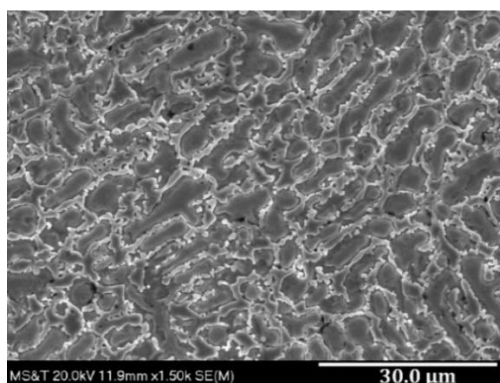
4.2. MICROSTRUCTURE CHARACTERIZATION

Micrographs were taken at three locations of the cross-section of the repaired samples: near the bonding area (Figure 11a), in the middle layers (Figure 11b) and on the top (Figure 11c). The microstructure of deposits near the interface exhibits mostly columnar structure growing parallel to the heat flow direction towards the top of deposits. Very few dendritic structures were observed in such regions. In the DMD process, the solidification rate at first few layers was very high. The substrate plays a role of the heat sink, leading to the growing direction of grains opposing the heat flux direction. The columnar grains were severely elongated due to the rapid cooling rate during the DMD process. Such high cooling rate leaves not enough time for forming secondary dendrites. As materials building up layer by layer, the cooling rate drops, and the microstructure gradually changed from columnar structure to dendrite with interdendritic eutectics as shown in Figure 11b. Most grains are fine due to rapid cooling that leaving insufficient time to grow. Some equiaxed grains were elongated against heat flux direction due to the rapid solidification during deposition. The microstructure at top regions consists of a mostly cellular structure (Figure 11c). That is because, after several layers of deposition, the cooling rate decreased and subsequently, fewer grains were elongated.

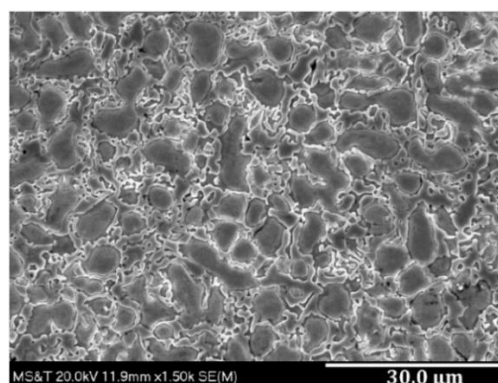
High residual tensile stress is usually associated with DMD process that may result in cracking to cobalt-based alloys coatings due to different thermal expansion coefficients between deposits and substrate [26]. Preheating substrate is usually suggested especially for coating thick layers to avoid cracking. In the current research, laser pre-scan with 300 W plays a role in preheating to reduce accumulation of tensile stress. As a result, no cracks were observed in deposited layers.



(a)



(b)



(c)

Figure 11. (a) Optical micrographs of materials on the bonding area; SEM micrograph of as-deposited Wallex 40 in the middle layers (b) and on the top (c)

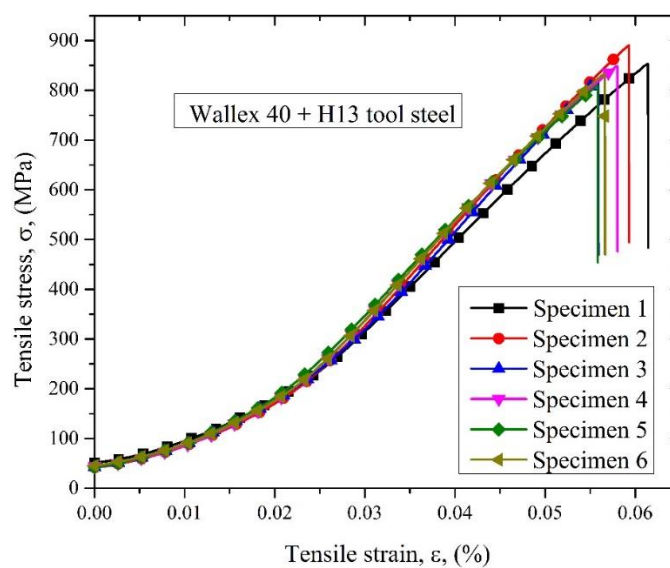
Relatively large equiaxed microstructure was discovered right below the interface and in the heat-affected zone (HAZ) (Figure 11a). This structure was fabricated because the material of the substrate near the interface was melted by the laser beam and then mixed with the delivered Wallex 40 and subsequently re-solidified. The rapid cooling rate during the process results in this coarse equiaxed-like morphology.

It is clear to notice that the bonding interface between deposits and substrate is very distinct. No defects such as cracks, pores, and delamination were detected along the interface. The microstructure along interface confirms the formation of the good metallurgical bond which is also supported by tensile testing and EDS analysis in sections 4.3 and 4.4.

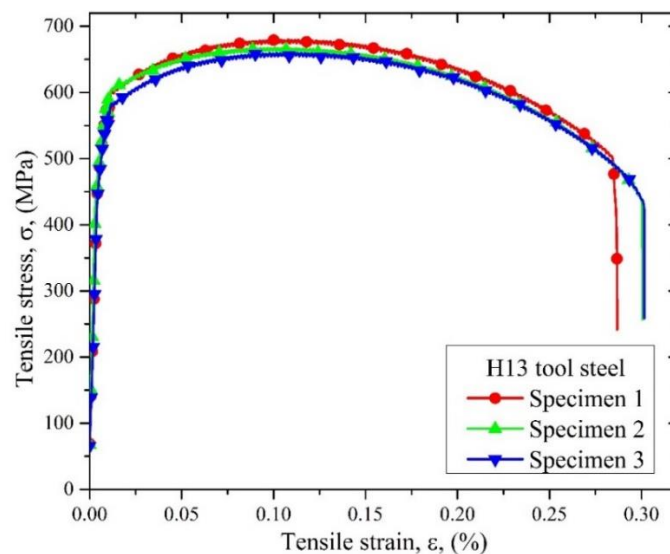
4.3. MECHANICAL PROPERTIES

4.3.1. Tensile Behavior. The stress-strain curves obtained from tensile testing were shown in Figure 12 and the results were summarized in Table 3. Two groups of samples were tested, including combined samples which is made of Wallex 40 deposits and H13 tool steel substrate, and pure H13 tool steel samples. The tensile testing of the combined samples is shown in Figure 12a and of the pure H13 tool steel samples is shown in Figure 12b. The combined samples revealed largely consistent tensile properties. The tensile stress increased with the increase of tensile strain to a peak of around 850 MPa. Then the tensile samples fractured suddenly, and the stress decreased rapidly. No yielding regions were found from the stress-strain curves, showing that the samples repaired using DMD process reveal brittle fracture failure. The ductility of the tensile samples was very low (approximately 6%). A further investigation of fractured samples reveals that the combined

samples broke at the as-deposited Wallex 40 section. Thus, the deposits show brittle failure during the tensile testing.



(a)



(b)

Figure 12. Tensile stress-strain curves obtained from the tensile test for (a) Wallex 40 + H13 tool steel samples, and (b) H13 tool steel samples

Table 3. UTS and elongation obtained from tensile testing

Material	Specimen	Specimen from	UTS (MPa)	Elongation (%)
Wallex 40 + H13 tool steel	1	Repair 1	853.3	6.14
	2	Repair 1	890.6	5.93
	3	Repair 2	822.6	5.59
	4	Repair 2	849.1	5.80
	5	Repair 3	809.8	5.59
	6	Repair 3	833.3	5.67
	Mean	-	843.1	5.78
S.D.	-	28.36	0.21	
H13 tool steel	1	H13 base metal	679.8	28.6
	2	H13 base metal	667.5	30.0
	3	H13 base metal	660.1	30.1
	Mean	-	669.1	29.57
	S.D.	-	9.95	0.84

Tensile testing of samples consisting of pure H13 tool steel shows that the tensile stress increased with the increase of strain to yield stress (YS) of approximately 600 MPa. Then an extensive plastic deformation and energy absorption were followed to reach a UTS of around 660 MPa, and the samples finally fractured. The samples were very ductile with an elongation of up to 30%.

A striking difference in the tensile test is that a long yielding region was exhibited before the final fracture for H13 tool steel samples compared with combined samples.

Another difference is that the UTS from repaired samples was found to be much higher than the H13 tool steel counterpart. The analyzed mean value of UTS for repaired samples was 843 MPa while was only 669 MPa for H13 tool steel. Since specimens fractured at deposits section for combined samples, the deposits show a higher tensile strength than H13 steel substrate. This phenomenon confirms that the repaired samples exhibited better tensile strength compared with the base metal.

The variation in UTS from combined samples was much higher than the H13 tool steel samples. This variation was attributed to the avoidable introduced defects such as micropores to the deposits during the DMD process in addition to dimensional errors in the sample measuring process for tensile testing.

4.3.2. Tensile Fracture Surface Morphology. The micrograph of the longitudinal section of the tensile fractured sample shown in Figure 13a reveals that samples broke at the as-deposited Wallex 40 section. There is barely necking region near the fracture surface, confirming the brittle fracture of deposits. The interface between deposits and substrate shown in Figure 13c was intact and defect free, which assures that good metallurgical bond was formed along the interface. Good bi-metallic bonding is essential to inhibit materials from delaminating during service. Since the interface is intact, one can conclude that the interface is stronger than the weaker material which is as-deposited Wallex 40.

The magnified view of the longitudinal fracture surface was shown in Figure 13b. One can see that the cracking during tensile testing was propagating along the grain boundaries. EDS mapping revealed that the boundary area was rich in Cr, W, Si, Mn and C. The high composition of Cr, W and Si form very hard phases, resulting in the brittle

fracture. Moreover, it has been observed that laser deposited Co-based alloys have very hard carbides and intermetallic phases including $M_{23}C_6$, Cr_7C_3 , Co_7W_6 , Co_3W and Co_2Si that contribute to the brittle failure of deposits [28, 29].

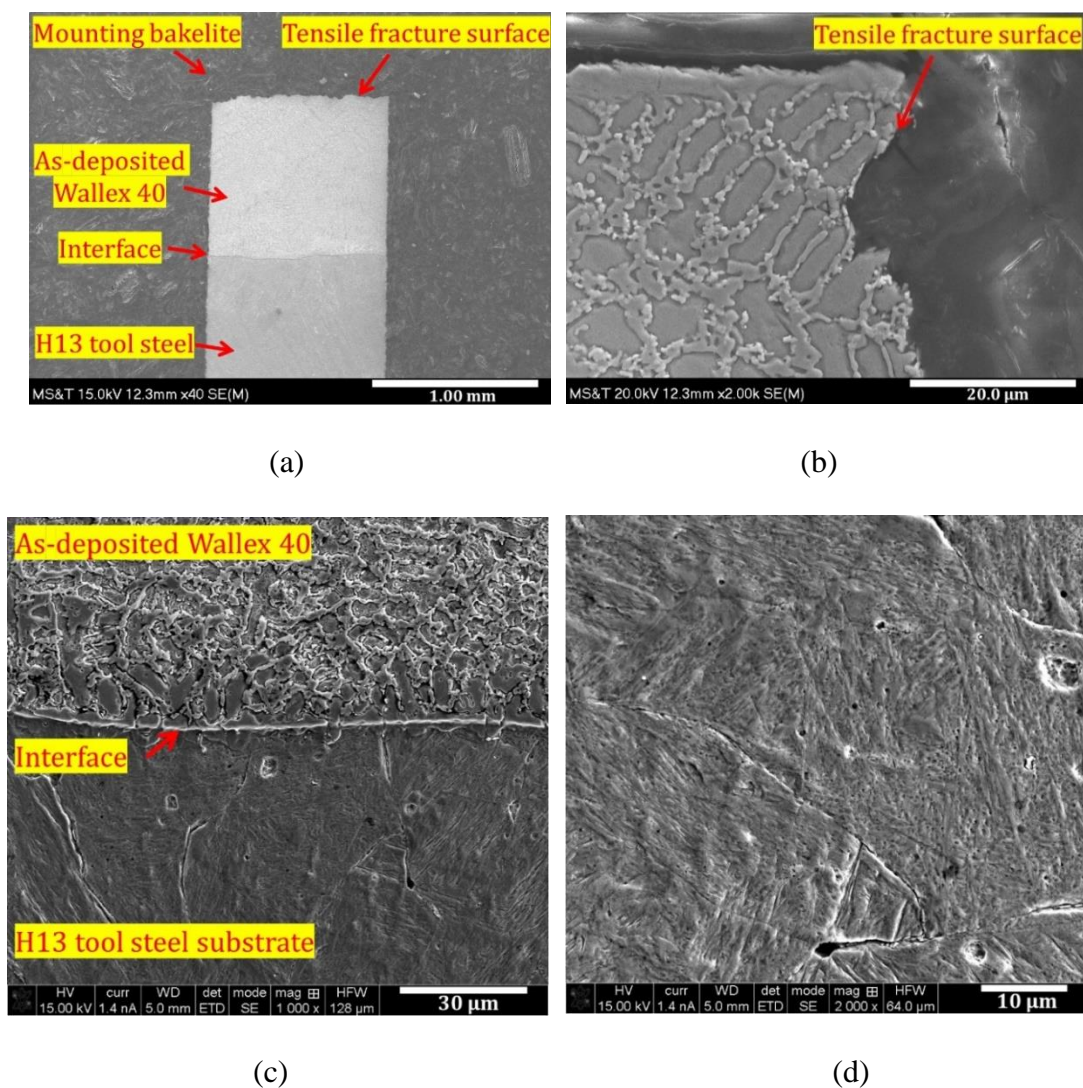


Figure 13. Fracture morphologies in longitudinal section of a Wallex 40 + H13 tool steel sample. (a) Overview of the fracture surface; (b) Magnified view of the fracture surface; (c) Magnified view of the bonding area; (d) Magnified view of the substrate near the interface

An interesting phenomenon discovered is that although the UTS of H13 steel is relatively low (around 669 MPa) compared to the UTS of Wallex 40 + H13 tool steel samples (843 MPa), all the combined samples fractured at the Wallex 40 region instead of the H13 steel zone. Although some cracks on the H13 steel region near the interface were found after the tensile test (Figure 13d), they didn't cause the final fracture. This phenomenon is probably because the laser melted some materials on the substrate and this amount of materials were combined with the filler material and then solidified. This dilution changed the microstructure and mechanical properties of the substrate material near the interface. Another reason is that the substrate material near the interface was in the heat-affected zone. The H13 tool steel used in the current study is in anneal condition. Therefore, the laser produced a function of hardening on the H13 tool steel. The heating history refined the microstructure of the substrate material, and then contributed to the improved tensile strength.

SEM micrographs of a transverse section of the tensile fracture surface were depicted in Figure 14. The overall view shown in Figure 14a reveals a relatively flat surface that is perpendicular to the tensile stress axis. There is no significant necking in the gauge length of the tensile specimens. Magnified view of morphology in various locations of fracture surface exhibits microscopically unsmooth fracture regions (Figures 14b-d). Microcracks were found on the fracture surface as shown in Figures 14c-d due to the overload during the tensile test. There is very limited population of voids and dimples observed in the fracture surface. This reveals a brittle fracture mechanism of the as-deposited Wallex 40.

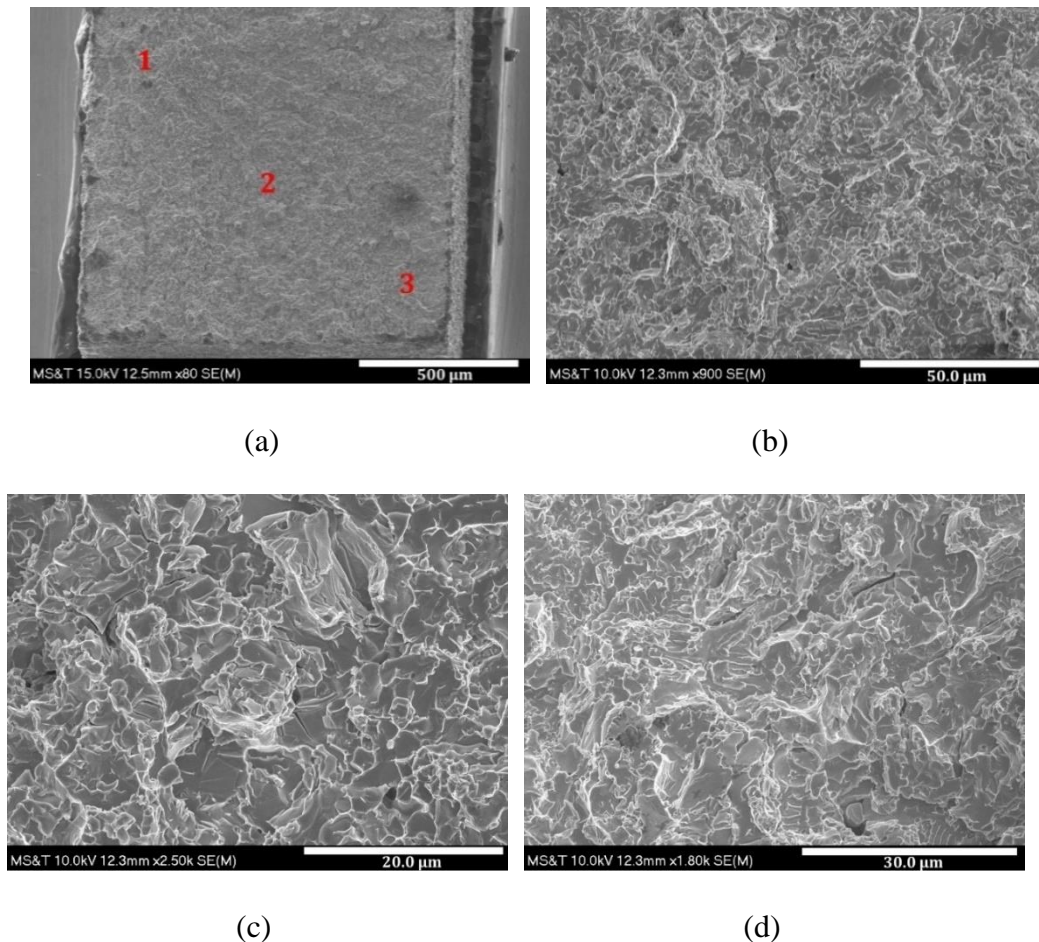


Figure 14. Fracture morphologies in cross-section of a Wallex 40 + H13 tool steel sample. (a) Overview of the fracture surface; (b) Magnified view of position 1; (c) Magnified view of position 2; (d) Magnified view of position 3

4.3.3. Vickers Hardness Analysis. Vickers hardness was measured on the cross-section of the repaired sample from deposits to substrate and the result was plotted in Figure 15. A constant distance of 0.4 mm was applied between two indentations.

It was shown that the as-deposited material has a relatively constant hardness of around 580 HV. The hardness of deposits is much higher than that of the as-received H13 tool steel substrate in annealed condition (220 HV). The hardness increased rapidly from

220 HV on the substrate to approximately 600 HV on the deposits. The sharply increased hardness on deposits is because of the rapid cooling rate and fine microstructure obtained on deposits. Cobalt-rich matrix with carbides also contributes to the elevated hardness. The hardness measured approximately near the interface reveals transitional values between 220 HV and 600 HV, indicating the existence of a narrow region of dilution in the heat-affected zone. The dilution distance between deposit and substrate from the hardness analysis was approximately 1 mm. Another feature that can be seen is that the hardness of deposits decreases slightly during multi-layer deposition. This was due to the higher cooling rate during the first layer of deposition. In a multi-layer deposition, the pre-deposited material was re-melted and heated, causing coarse microstructure and slightly drop of hardness. The hardness at the substrate near the interface is slightly higher than the area away from the interface. Heating history in HAZ acts as a normalization process that increases the hardness in such area.

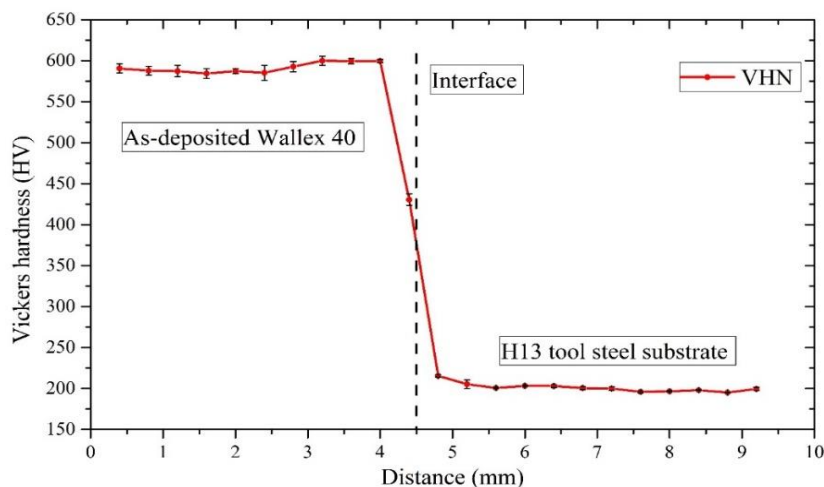


Figure 15. Vickers hardness distribution

4.4. EDS ANALYSIS

4.4.1. Interface EDS Analysis. EDS mapping and line scan analysis were performed to analyze elemental composition and distribution from the substrate to deposits passing through the interface. For the line scan analysis, major elements were quantified through the route. Totally 806 points were selected at a distance of 251 μm . Dwell time for each point was 200 ms. The EDS mapping and line scan were depicted in Figure 16 and Figure 17 respectively.

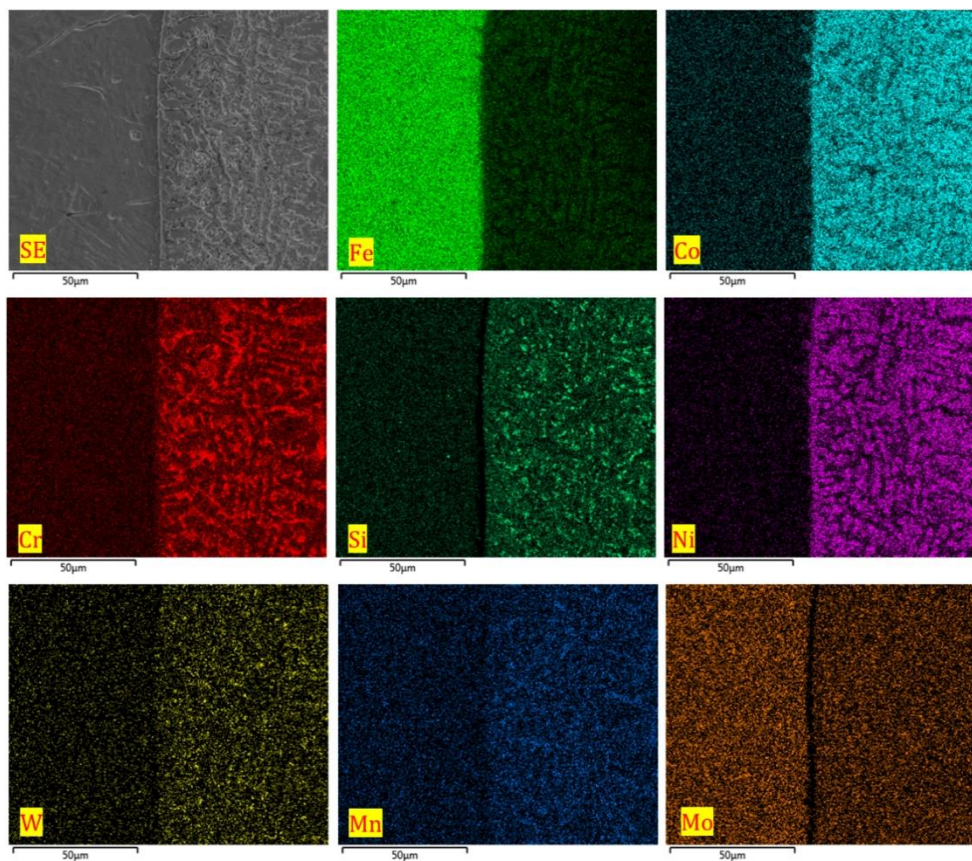


Figure 16. EDS mapping at the interface

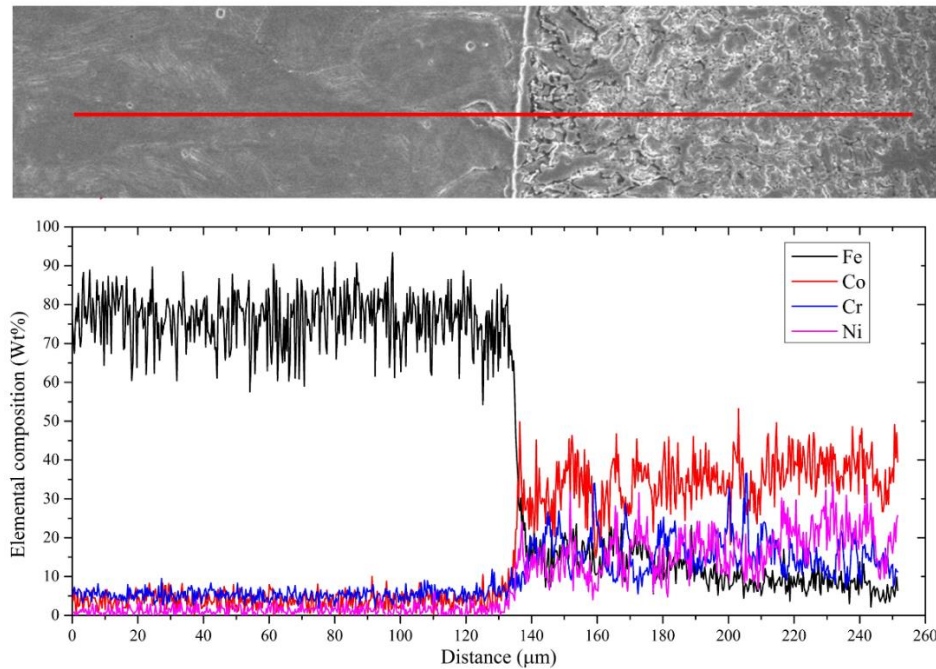


Figure 17. EDS line scan analysis from the substrate to deposits

EDS mapping reveals that some elements such as Ni and Co were diluted from the deposits into the substrate since the H13 tool steel has no composition of Ni and Co. Another point is that Si and Mo were not detected along the interface while all other elements were found in the interface region.

The EDS line scan analysis in Figure 17 exhibits that the transition of major elements from the substrate to deposits is rapid. Fe is slightly higher in the deposits near the interface compared to the area away from the interface, showing the dilution of Fe into deposits. Fe contributes a lot to phase transformation over the interface. The result confirms that excellent metallurgical bond was formed along the interface after deposition.

4.4.2. Deposits EDS Analysis. The secondary electron image of deposits was depicted in Figure 18, and EDS mapping was performed in this area to analyze the elemental distribution. Two phases were revealed by the EDS mapping, one is mostly along the grain boundary and another one is inside the boundary. The mapping shows that the grain boundaries were rich in Cr, W, Si, Mn and C while less in Co and Ni. The inner phase was dominated by Co and Ni and also has higher concentrations of Fe and Si.

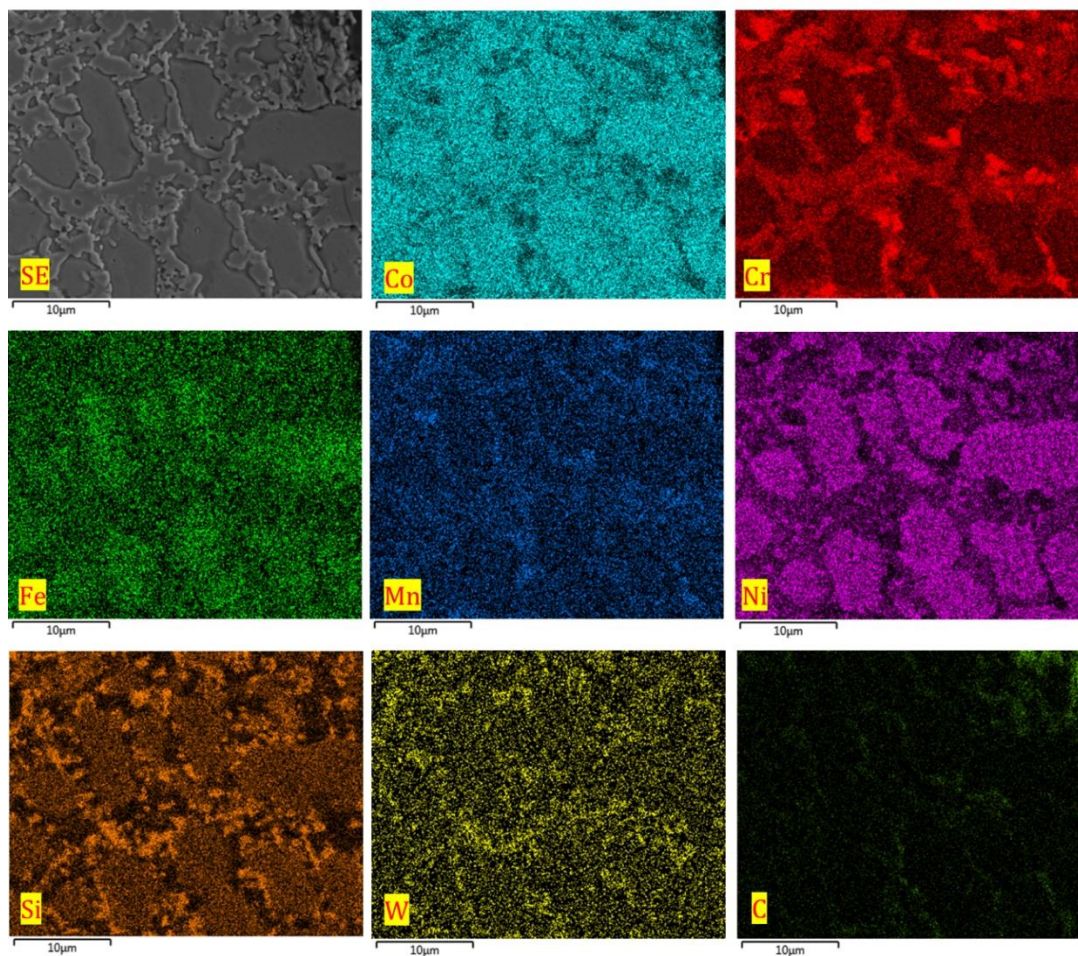


Figure 18. EDS mapping at the deposits

5. CONCLUSION

In this research, defects on H13 tool steel substrates were successfully repaired by depositing cobalt-based alloys on the damaged zone via DMD process. Through microstructure analysis and mechanical test, some conclusions were generalized.

The geometry of repair volume was obtained through 3D scanning and the repair volume was sliced into 6 layers to generate a smooth raster tool path for material deposition. Methodology for continuous tool path generation was introduced. By depositing an extra layer that along the damage boundary or completely covers the defective region, the defects can be repaired successfully with no gap along the boundary.

Microstructure and tensile test confirm the strong metallurgical bond along the interface. The microstructure of deposits near the interface exhibits mostly columnar structure due to the rapid cooling rate during the DMD process. The microstructure of deposits in middle layers show dendrite structure with interdendritic eutectics. The microstructure of deposits on top regions consists of mostly cellular structure.

The repaired samples exhibit a higher UTS (843 MPa) compared with the substrate (669 MPa). The fracture morphology shows the repaired samples fractured at deposits section with cracks propagating along grain boundaries. EDS mapping revealed that the boundary was rich in Cr, W, Si, Mn, and C while less in Co and Ni, forming hard phases that result in brittle failure during the tensile test. Fracture morphology on transverse section reveals the brittle fracture mechanism of the repaired samples.

Relative homogeneous microhardness was found in the deposits. Hardness was rapidly increased from 220 HV on the substrate to around 580 HV in deposits.

ACKNOWLEDGMENTS

This project was supported by NSF Grants CMMI-1547042 and CMMI 1625736, and the Intelligent Systems Center, Center for Aerospace Manufacturing Technologies, and Material Research Center at Missouri S&T. Their financial support is greatly appreciated.

REFERENCES

- [1] K. Zhang, W. Liu, and X. Shang, "Research on the Processing Experiments of Laser Metal Deposition Shaping," *Optics & Laser Technology*, vol. 39, pp. 549-557, 2007.
- [2] H. K. Rafi, T. L. Starr, and B. E. Stucker, "A Comparison of the Tensile , Fatigue , and Fracture Behavior of Ti - 6Al - 4V and 15-5 PH Stainless Steel Parts Made by Selective Laser Melting," *International Journal of Advanced Manufacturing Technology*, vol. 69, pp. 1299-1309, 2013.
- [3] O. M. Al-Jamal, S. Hinduja, and L. Li, "Characteristics of the Bond in Cu-H13 Tool Steel Parts Fabricated using SLM," *CIRP Annals*, vol. 57, pp. 239-242, 2008.
- [4] G. P. Dinda, L. Song, and J. Mazumder, "Fabrication of Ti-6Al-4V Scaffolds by Direct Metal Deposition," *Metallurgical and Materials Transactions A*, vol. 39, pp. 2914-2922, 2008.
- [5] E. C. Santos, M. Shiomi, K. Osakada, and T. Laoui, "Rapid Manufacturing of Metal Components by Laser Forming," *International Journal of Machine Tools and Manufacture*, vol. 46, pp. 1459-1468, 2006.
- [6] B. Baufeld, O. Van der Biest, and R. Gault, "Additive Manufacturing of Ti-6Al-4V Components by Shaped Metal Deposition: Microstructure and Mechanical Properties," *Materials & Design*, vol. 31, pp. S106-S111, 2010.
- [7] F. Weng, H. Yu, C. Chen, and J. Dai, "Microstructures and Wear Properties of Laser Cladding Co-based Composite Coatings on Ti-6Al-4V," *Materials & Design*, vol. 80, pp. 174-181, 2015.
- [8] F. Weng, C. Chen, and H. Yu, "Research Status of Laser Cladding on Titanium and its Alloys: A Review," *Materials & Design*, vol. 58, pp. 412-425, 2014.

- [9] D. Bartkowski, A. Młynarczak, A. Piasecki, B. Dudziak, M. Gościański, and A. Bartkowska, "Microstructure, Microhardness and Corrosion Resistance of Stellite-6 Coatings Reinforced with WC Particles using Laser Cladding," *Optics & Laser Technology*, vol. 68, pp. 191-201, 2015.
- [10] S. W. Huang, M. Samandi, and M. Brandt, "Abrasive Wear Performance and Microstructure of Laser Clad WC/Ni Layers," *Wear*, vol. 256, pp. 1095-1105, 2004.
- [11] B. AlMangour, D. Grzesiak, and J.-M. Yang, "Nanocrystalline TiC-Reinforced H13 Steel Matrix Nanocomposites Fabricated by Selective Laser Melting," *Materials & Design*, vol. 96, pp. 150-161, 2016.
- [12] B. AlMangour, D. Grzesiak, and J.-M. Yang, "Selective Laser Melting of TiB₂/H13 Steel Nanocomposites: Influence of Hot Isostatic Pressing Post-Treatment," *Journal of Materials Processing Technology*, vol. 244, pp. 344-353, 2017.
- [13] W. H. Jiang and R. Kovacevic, "Laser Deposited TiC/H13 Tool Steel Composite Coatings and their Erosion Resistance," *Journal of Materials Processing Technology*, vol. 186, pp. 331-338, 2007.
- [14] J. Song, Q. Deng, C. Chen, D. Hu, and Y. Li, "Rebuilding of Metal Components with Laser Cladding Forming," *Applied Surface Science*, vol. 252, pp. 7934-7940, 2006.
- [15] S. Nowotny, S. Scharek, E. Beyer, and K. H. Richter, "Laser Beam Build-Up Welding: Precision in Repair, Surface Cladding, and Direct 3D Metal Deposition," *Journal of Thermal Spray Technology*, vol. 16, pp. 344-348, 2007.
- [16] A. J. Pinkerton, W. Wang, and L. Li, "Component Repair using Laser Direct Metal Deposition," *Proceedings of the Institution of Mechanical Engineers, Part B: Journal of Engineering Manufacture*, vol. 222, pp. 827-836, 2008.
- [17] T. H. C. Childs, S. P. Akhtar, C. Hauser, M. Youseffi, P. Fox, and C. S. Wright, "Selective Laser Melting of Prealloyed High Alloy Steel Powder Beds," *Advanced Materials Forum III*, vol. 514, pp. 516-523, 2006.
- [18] B. Graf, A. Gumenyuk, and M. Rethmeier, "Laser Metal Deposition as Repair Technology for Stainless Steel and Titanium Alloys," *Physics Procedia*, vol. 39, pp. 376-381, 2012.
- [19] H. Paydas, A. Mertens, R. Carrus, J. Lecomte-beckers, and J. T. Tchuindjang, "Laser Cladding as Repair Technology for Ti-6Al-4V Alloy : Influence of Building Strategy on Microstructure and Hardness," *Materials & Design*, vol. 85, pp. 497-510, 2015.

- [20] H. Qi, M. Azer, and P. Singh, "Adaptive Toolpath Deposition Method for Laser Net Shape Manufacturing and Repair of Turbine Compressor Airfoils," *International Journal of Advanced Manufacturing Technology*, vol. 48, pp. 121-131, 2010.
- [21] J. Gao, X. Chen, O. Yilmaz, and N. Gindy, "An Integrated Adaptive Repair Solution for Complex Aerospace Components through Geometry Reconstruction," *International Journal of Advanced Manufacturing Technology*, vol. 36, pp. 1170-1179, 2008.
- [22] J. M. Wilson, C. Piya, Y. C. Shin, F. Zhao, and K. Ramani, "Remanufacturing of Turbine Blades by Laser Direct Deposition with its Energy and Environmental Impact Analysis," *Journal of Cleaner Production*, vol. 80, pp. 170-178, 2014.
- [23] R. Liu, Z. Wang, T. Sparks, F. Liou, and C. Nedic, "Stereo Vision-Based Repair of Metallic Components," *Rapid Prototyping Journal*, vol. 23, pp. 65-73, 2017.
- [24] K. Surekha and A. Els-Botes, "Effect of Cryotreatment on Tool Wear Behaviour of Bohler K390 and AISI H13 Tool Steel During Friction Stir Welding of Copper," *Transactions of the Indian Institute of Metals*, vol. 65, pp. 259-264, 2012.
- [25] N. Shamsaei, A. Yadollahi, L. Bian, and S. M. Thompson, "An Overview of Direct Laser Deposition for Additive Manufacturing; Part II: Mechanical Behavior, Process Parameter Optimization and Control," *Additive Manufacturing*, vol. 8, pp. 12-35, 2015.
- [26] W. C. Lin and C. Chen, "Characteristics of Thin Surface Layers of Cobalt-Based Alloys Deposited by Laser Cladding," *Surface and Coatings Technology*, vol. 200, pp. 4557-4563, 2006.
- [27] C. P. Paul, H. Alemohammad, E. Toyserkani, A. Khajepour, and S. Corbin, "Cladding of WC-12 Co on Low Carbon Steel using a Pulsed Nd:YAG Laser," *Materials Science and Engineering: A*, vol. 464, pp. 170-176, 2007.
- [28] C. Cui, Z. Guo, Y. Liu, Q. Xie, Z. Wang, J. Hu, and Y. Yao, "Characteristics of Cobalt-Based Alloy Coating on Tool Steel Prepared by Powder Feeding Laser Cladding," *Optics & Laser Technology*, vol. 39, pp. 1544-1550, 2007.
- [29] A. S. C. M. D'Oliveira, P. S. C. P. da Silva, and R. M. C. Vilar, "Microstructural Features of Consecutive Layers of Stellite 6 Deposited by Laser Cladding," *Surface and Coatings Technology*, vol. 153, pp. 203-209, 2002

SECTION

2. CONCLUSION

Considering a great application of additive manufacturing is for metallic component remanufacturing, this research targets at several key issues associated with part repair, including pre-repair processing strategies, damage detection and reconstruction algorithms, and evaluation of remanufactured components. Based on these research tasks, some conclusions were summarized as follows.

At first, in order to investigate the influence of sidewall inclination angle of the damage on the properties of repaired parts, V-shaped grooves with different sidewall inclination angles of 45° , 75° , and 90° were prepared on H13 tool steel blocks. The objective of this research is to define an appropriate sidewall tilt angle to support the pre-repair machining strategies. These machined blocks were scanned to acquire the 3D models. Then raster deposition tool paths were generated based on the reconstructed 3D models of the blocks. A cobalt-based alloy was filled in the damaged region to restore the missing geometry. Macrostructure examination shows that the sample with 90° sidewall damage was not repaired successfully since the laser was not able to melt materials in the vertical surface and then, the filler material cannot bond well with the substrate. Samples with 45° and 75° damage were repaired successfully, showing excellent metallurgical bonding along the interface. Microstructure characterization reveals columnar structure dominates the deposits near the interface owing to rapid cooling rate. Tensile testing

confirms the strong bonding strength between deposits and substrates, while the influence of sidewall inclination angle on the tensile strength is not observed.

To further develop pre-repair processing strategies, components with varied defects were investigated, including surface indentations, wear, corrosion, erosion, heat checks, cracking, and thermal fatigue. For surface indentations, two strategies, U-shaped strategy and convex-hull strategy were introduced to define the machining volume. The example adopted in this task shows the convex-hull strategy gives the minimal material removal and therefore, the convex-hull strategy was utilized for cut-off volume definition. Based on the target geometry, machining tool path was generated and CNC machining was performed on the damaged part. For surface wear, corrosion, erosion, and heat-checks, an approach was presented to quickly remove a thin layer of material from the damaged parts. In detail, the damaged region was scanned to obtain the 3D model. Then the model was loaded to CAM software to generate the machining tool path after considering the cut depth and machining areas. Candidate machining approaches for cracking were introduced and can be selected considering a number of factors such as the depth and length of cracks, surrounding structures, accessibility of cracks to machining tools, surface or internal cracking, etc. Pre-repair heat-treatment procedure for re-hardening H13 tool steel after a large number of thermal fatigue was introduced. Tensile testing and hardness measurements of re-hardened H13 tool steel show the nominal mechanical properties of damaged H13 tool steel material were successfully restored.

Moreover, this research proposed algorithms for reconstructing repair volume of jet engine blades. At first, models of nominal and damaged blades were obtained through reverse engineering. Then the damaged model was aligned with the nominal model by a

transformation matrix using the overlapping area comparison method. By taking the area comparison method, defective layers on the damaged models were detected. One-directional ray casting method was adopted to extract the repair volume on the defective layers. After that, repair tool path was generated based on the repair volume and repair experiment was conducted to deposit titanium powder on the defective region. Finally, microstructure examination was performed on the repaired part to test the repair quality and it shows the blade was repaired successfully. This research introduced a model alignment algorithm, damaged detection and reconstruction methodologies for efficiently obtaining repair volume on engine blades.

In order to further extend the damage detection and reconstruction methodologies to a variety of parts, tri-dexel method was utilized as damage reconstruction approach to regenerate three-dimensional repair volume. Once the damaged model was aligned with the nominal model, the damaged zone was chosen and the corresponding minimum bounding box was generated. Then a number of casting rays in three directions were generated to intersect the damaged and nominal model. By comparing intersections of casting rays with nominal and damaged models, the repair volume was reconstructed. After that, the reconstructed repair volume was sliced to generate repair tool path. The reconstructed damage using the proposed tri-dexel method was compared with the exact damage to investigate the accuracy of the process. The result shows that by reducing the grid interval to a specific level, a high accurate reconstructed damage can be obtained. A damaged turbine rotor and two damaged dies were implemented as case studies to test the feasibility of the damage detection and reconstruction processes.

The final task aims to evaluate the metallic components repaired using the additive manufacturing process. Several H13 tool steel substrates were repaired by depositing a cobalt-based alloy on the damaged zone via a direct metal deposition process. Microstructure examination and mechanical testing were conducted to evaluate the repaired parts. The microstructure characterization confirms the fully dense deposits that are free of defects. Besides, microstructure analysis and tensile testing confirm the strong metallurgical bond along the bi-material interface. The repaired samples exhibit a higher UTS compared with the substrates. Hardness measurement shows the hardness increased rapidly from the substrate to the deposits. The conducted testing confirms that the metallic parts were repaired successfully through the additive manufacturing process.

The overall outcomes of this dissertation addressed several key problems which are challenging the wide application of the additive manufacturing process for metallic component repair. The research provided pre-repair processing strategies to guarantee the damaged parts are ready for remanufacturing. Besides, it provided an efficient way for repairing complex structures by proposing damage detection and reconstruction algorithms to automatically regenerate the repair volume precisely. In addition, evaluation of repaired components revealed the damaged parts can be repaired successfully through the additive manufacturing process. The results of this dissertation provided methodologies for metallic component repair that could benefit many industries.

BIBLIOGRAPHY

- [1] E. Silveira, G. Atxaga, and A. M. Irisarri, "Failure Analysis of Two Sets of Aircraft Blades," *Engineering Failure Analysis*, vol. 17, pp. 641-647, 2010.
- [2] S. Jhavar, C. P. Paul, and N. K. Jain, "Causes of Failure and Repairing Options for Dies and Molds: A Review," *Engineering Failure Analysis*, vol. 34, pp. 519-535, 2013.
- [3] W. R. Morrow, H. Qi, I. Kim, J. Mazumder, and S. J. Skerlos, "Environmental Aspects of Laser-Based and Conventional Tool and Die Manufacturing," *Journal of Cleaner Production*, vol. 15, pp. 932-943, 2007.
- [4] C. Chen, Y. Wang, H. Ou, Y. He, and X. Tang, "A Review on Remanufacture of Dies and Moulds," *Journal of Cleaner Production*, vol. 64, pp. 13-23, 2014.
- [5] O. M. R. O. Strategies, W. W. Wits, J. R. R. García, and J. M. J. Becker, "How Additive Manufacturing Enables more Sustainable End-user Maintenance , Repair and Overhaul (MRO) strategies," *Procedia CIRP*, vol. 40, pp. 694-699, 2016.
- [6] E. Capello, D. Colombo, and B. Previtali, "Repairing of Sintered Tools using Laser Cladding by Wire," *Journal of Materials Processing Technology*, vol. 164-165, pp. 990-1000, 2005.
- [7] P. Kattire, S. Paul, R. Singh, and W. Yan, "Experimental Characterization of Laser Cladding of CPM 9V on H13 Tool Steel for Die Repair Applications," *Journal of Manufacturing Processes*, vol. 20, pp. 492-499, 2015.
- [8] B. Graf, A. Gumenyuk, and M. Rethmeier, "Laser Metal Deposition as Repair Technology for Stainless Steel and Titanium Alloys," *Physics. Procedia*, vol. 39, pp. 376-381, 2012.
- [9] X. Zhang, W. Li, K. M. Adkison, and F. Liou, "Damage Reconstruction from Tri-Dexel Data for Laser-Aided Repairing of Metallic Components," *International Journal of Advanced Manufacturing Technology*, vol. 96, pp. 3377-3390, 2018.
- [10] F. Caiazzo, "Laser-Aided Directed Metal Deposition of Ni-Based Superalloy Powder," *Optics & Laser Technology*, vol. 103, pp. 193-198, 2018.
- [11] X. Zhang, W. Li, X. Chen, W. Cui, and F. Liou, "Evaluation of Component Repair using Direct Metal Deposition from Scanned Data," *International Journal of Advanced Manufacturing Technology*, vol. 95, pp. 3335-3348, 2018

VITA

Xinchang Zhang was born in Deping, Linyi, Dezhou, Shandong, China. He received his Bachelor of Science Degree in mechanical engineering in July 2013 from Qingdao University, China. In June 2015, he received his master's degree in automotive engineering from Wuhan University of Technology, China. In July 2019, he received his Doctor of Philosophy in mechanical engineering from Missouri University of Science and Technology, Rolla, Missouri, USA. He received the Best Paper Award in the 2018 Solid Freeform Fabrication Symposium Conference and 2017 NSF Student Travel Award. He also received the Outstanding Reviewer Award from Additive Manufacturing Journal. His research interests included metal additive manufacturing, laser cladding, component repair, CAD/CAE/CAM, and fabrication of advanced materials and structures. During his Ph.D. study, he authored 12 journal papers and 5 conference proceedings.